

Scalar Polarizability of the Indium $6P_{1/2}$ State:
Atomic Beam Stark Shift Measurements
Using Two-Step Laser Spectroscopy

by
Benjamin L. Augenbraun

Professor Protik K. Majumder, Advisor

A thesis submitted in partial fulfillment
of the requirements for the
Degree of Bachelor of Arts with Honors
in Physics

WILLIAMS COLLEGE
Williamstown, Massachusetts
May 13, 2015

For Mr. Durkee and Mr. Delzell, who set me on the path of physics,
And for my parents, who encouraged me to follow it.

Abstract

We have nearly completed a high-precision measurement of the scalar polarizability of the indium $6P_{1/2}$ state using two-step laser spectroscopy in an atomic beam. Preliminary data reveals $\alpha_0(6P_{1/2}) = 7938 \pm 60(\text{stat}) \pm 200(\text{sys})a_0^3$. This is in excellent agreement with recent theoretical calculations. We make use of a newly implemented two-tone FM spectroscopy scheme to observe the two-step transition in an atomic beam. The methods outlined in this thesis represent the first time our group has observed a multi-step transition in an atomic beam. We lock one laser, at 410 nm, to the lower transition in an atomic vapor cell while simultaneously scanning a second laser, at 1343 nm, across the upper transition. Furthermore, we have introduced a new, robust method of laser stabilization, making use of an EOM and frequency modulation to routinely lock to several hundred kHz noise. As part of this polarizability measurement, we have also obtained a measurement of the hyperfine structure in the $6P_{1/2}$ state. This result is in rough agreement with existing measurements, but an order of magnitude more precise. Determination of systematic errors remains to be done, requiring more data collection. In parallel to experimental advances that led to this preliminary measurement, we have undertaken a theoretical study of three-level systems to understand how the observed Stark shift arises in these simultaneously coupled states. With more data collection, we aim to measure the polarizability to $<1\%$ precision, providing a stringent test of *ab initio* atomic theory calculation methods.

Acknowledgments

First and foremost, I thank my advisor, Professor Tiku Majumder. His kindness, enthusiasm, and deep knowledge of physics have been an inspiration to me throughout my time at Williams College. He is the sort of physicist and teacher I aspire to be someday. I would also like to thank Professor Charlie Doret for his tremendously useful feedback on this thesis and the many conversations we had over the past year about experimental physics. How nice it is to have such a successful example of a former Majumder lab member right upstairs!

I also wish to thank Dr. Milinda Rupasinghe, who joined our group in January, for his good humor and general helpfulness in lab. I owe a debt of gratitude to Michael Taylor, who helped with all things machine shop, and Jason Mativi, who helped bring circuits to life and revived an ailing vacuum pump. I am also indebted to Professor Fred Strauch, who demonstrated his characteristic kindness in helping with the theoretical treatment of three-level systems. Nathan Bricault '14 deserves my appreciation for introducing me to the Majumder lab last year, and for leaving me in a prime position to continue this Stark shift measurement.

I thank my friends, for listening whenever I wanted to talk about my thesis— and for taking my mind off of it when that was what I needed more. To the “five o’clock dinner crew,” thank you for making this year so much fun and so full of laughs. Here’s one last toast, from me to each of you.

Most of all, I thank my family for their love and support. They taught me to ask questions about the world around me, and gave me the confidence to seek the answers. For that, I am eternally grateful.

Executive Summary

This thesis outlines the near completion of the first ever high-precision measurement of the DC Stark shift in the two-step $5P_{1/2} \rightarrow 6S_{1/2} \rightarrow 6P_{1/2}$ transition in indium. We use the Stark shift in this transition to determine the static polarizability of the $6P_{1/2}$ state. We have nearly completed the measurement, and a recently completed *ab initio* atomic theory calculation of this quantity is in excellent agreement with our preliminary results. Our data analysis also makes it possible to obtain a new, precise measurement of the hyperfine structure within the $6P_{1/2}$ state in indium. Preliminary analysis indicates that our measurement of this quantity will also agree well with theory and previous measurements, while being at least an order of magnitude more precise. See Figure 1 for preliminary analyses of both quantities. In Figure 1a, we have conservatively estimated systematic uncertainties from preliminary data; the shaded region represents the statistical uncertainty in the preliminary analysis.

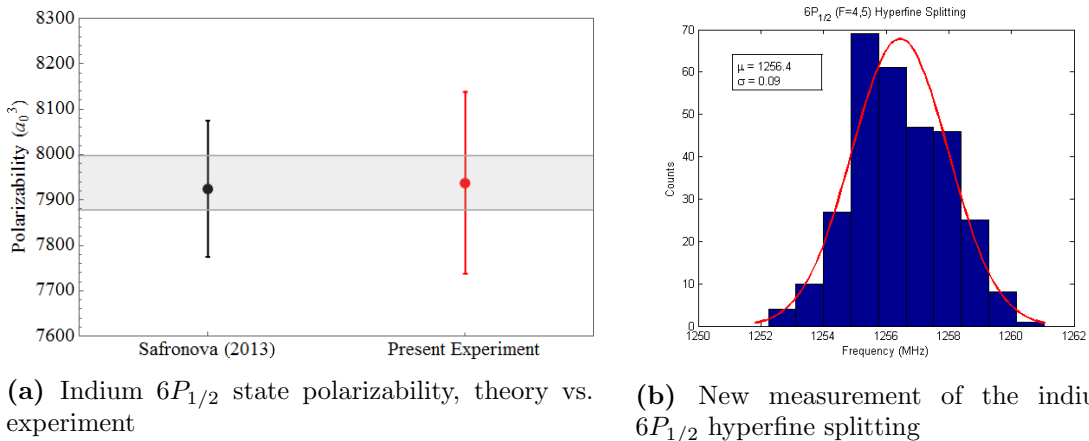


Figure 1: Preliminary data. (a) Stark shift measurement, to be improved with a new optical setup being implemented now. The shaded region represents the statistical error in our measurement, whereas the error bar contains both systematic and statistical uncertainties. (b) Hyperfine splitting measurement, which we get “for free” from our frequency calibration method.

The Stark shift and the hyperfine structure are but two of the atomic structure observables of interest to the Majumder lab. Our goal is to perform high-precision tests of atomic theory in Group IIIA atomic systems, like indium and thallium. We do so to provide stringent tests of atomic theory calculations produced by theorists.

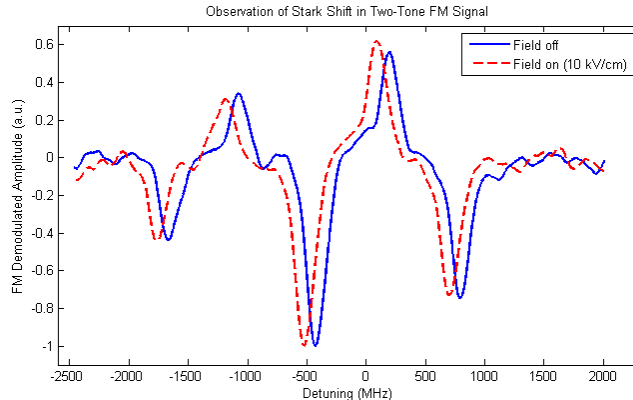


Figure 2: Observation of a two-step transition in the atomic beam, using two-tone FM spectroscopy. Shown are two copies of the absorption pattern, one with HV-on (solid/ blue) and another with HV-off (dashed/ red). For this example, the HV was set to 10 kV, and we observe a shift of roughly 100 MHz.

The scalar polarizability of the $6P_{1/2}$ state is an especially useful test of atomic theory: predicting it requires good calculations of a nearby D -state, which is notoriously difficult to model. Over the years, we have developed an extremely productive collaboration with Mariana Safronova at the University of Delaware, whose group produces many relevant theoretical predictions based on *ab initio* quantum mechanical calculations. Ultimately, high quality tests of atomic theory like these may have relevance to searches for physics beyond the Standard Model— finding fundamentally new physics requires that we understand the “ordinary” quantum mechanics well enough first.

We observe the Stark shift as the change in frequency of atomic transitions caused by a static electric field (see Figure 2). To perform this two-step Stark shift measurement, we make use of an atomic beam apparatus. The beam is produced by an indium sample heated to 1100°C in a home-built molybdenum crucible, and then shaped into a thin beam by collimating elements. This atomic beam is housed within a vacuum chamber which we regularly maintain at pressures below 10^{-6} Torr. The beam passes through a pair of high voltage plates, separated by 1 cm, which we use to apply electric fields of up to 20 kV/cm across the atoms. Perpendicular to both the applied electric field and the atomic beam, a pair of laser beams— one tuned to the $5P_{1/2} \rightarrow 6S_{1/2}$ 410 nm transition and the other tuned to the $6S_{1/2} \rightarrow 6P_{1/2}$ 1343 nm transition— interacts with the atomic beam. We stabilize the blue laser using a method developed over the course of this thesis: an EOM is used to generate a dispersion-like frequency modulation (FM) signal in a table-top vapor cell, and this error signal provides electronic feedback to the laser. This allows us to lock the laser to an atomic resonance with residual RMS noise of less than 1 MHz. We measure the transmitted intensity of the IR laser through the atomic beam, and compare the location of the resonance when the applied electric field is on to when it is off to determine the Stark shift. Due to the very low optical depth (of order 10^{-3}) in the atomic beam, we make use of two-tone FM spectroscopy to observe the absorption.

This represents the first time our group has ever observed a multi-level transition in the atomic beam. It makes possible not only the present experiment, but many interesting and important extensions in the near future.

In order to understand how to convert the raw, observed frequency shift to a value for the actual Stark shift, we studied the quantum mechanics of a three-level system coupled by two laser fields. We developed numerical and analytic¹ treatments of the behavior of the Stark shift in three-level systems. This thesis explores some of that theory and demonstrates that depending on how the experiment is conducted, one can expect to measure either the difference in Stark shifts between the first and third state *or* between the second and third state. As is typical of Stark shift measurements, we can only measure the difference in shifts between two states. We are able to turn this number into a value for the polarizability of just the uppermost state using existing measurements of the lower states' polarizabilities.

We have assembled the necessary data acquisition and analysis software. A Lab-View program is used to control the experimental apparatus and acquire data. A suite of MATLAB code has been developed to turn raw data into measurements of both the Stark shift and the hyperfine splitting. After a few modifications to the experimental apparatus, already underway, all that remains is the collection of additional data sets to analyze and use in systematic error searches. The preliminary measurements contained within this thesis demonstrate that our statistical power will be sufficient, and we will be limited only by systematic uncertainties in the final measurement (see Figure 3). We aim to complete this measurement with a 1% uncertainty, a level of precision exceeding that of the theoretical calculation we wish to test. Immediate extensions of this work to higher excited states in indium present exciting potential tests of atomic theory while requiring minimal changes to the experimental apparatus constructed for the present experiment.

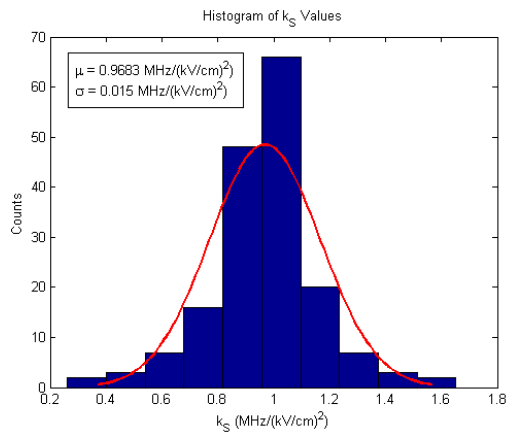


Figure 3: Preliminary measurement of k_S . This corresponds to the difference in Stark shifts between the $6P_{1/2}$ and $5P_{1/2}$ states, as discussed in the body of this thesis.

¹with the help of Professor Fred Strauch

Contents

| | |
|---|-----------|
| Abstract | ii |
| Acknowledgments | iii |
| Executive Summary | iv |
| 1 Introduction | 1 |
| 1.1 Motivation | 2 |
| 1.2 Indium and Thallium | 3 |
| 1.3 Previous Work | 4 |
| 1.4 Present Work | 5 |
| 1.5 Outline of This Thesis | 6 |
| 2 Atomic Spectroscopy and Theory | 7 |
| 2.1 Absorption Spectroscopy | 7 |
| 2.2 Frequency Modulation | 9 |
| 2.2.1 Single-Tone FM Spectroscopy | 10 |
| 2.2.2 Two-Tone FM Spectroscopy | 12 |
| 2.3 The Stark Shift | 12 |
| 2.4 The Stark Shift in a Two-Step Transition | 15 |
| 2.4.1 Three-Level Resonance | 16 |
| 2.4.2 Blue Laser Always Resonant with Field-Free Sample | 18 |
| 2.4.3 Blue Laser Always Resonant with Atomic Beam | 20 |
| 3 Experimental Setup | 23 |
| 3.1 Sources of Atoms | 23 |
| 3.1.1 Table-Top Vapor Cell | 23 |
| 3.1.2 Atomic Beam Unit | 25 |
| 3.2 Optical System | 28 |
| 3.2.1 External Cavity Diode Lasers | 28 |
| 3.2.2 Frequency Stabilization of the 410 nm Laser | 29 |
| 3.2.3 IR Laser Preparation and Modulation | 33 |
| 3.3 Data Acquisition | 34 |
| 4 Data Collection and Analysis | 36 |
| 4.1 Observation of $6S_{1/2} \rightarrow 6P_{1/2}$ Transition | 36 |
| 4.1.1 Vapor Cell Work | 36 |

| | | |
|----------|--|-----------|
| 4.1.2 | Atomic Beam Work | 38 |
| 4.2 | Data Analysis | 40 |
| 4.2.1 | Collected Signals | 41 |
| 4.2.2 | Data Import | 42 |
| 4.2.3 | Frequency Linearization | 43 |
| 4.2.4 | Frequency Calibration | 45 |
| 4.2.5 | Stark Shift Determination | 47 |
| 4.3 | Preliminary Results | 50 |
| 5 | Ongoing and Future Work | 53 |
| 5.1 | Controllable Frequency Detuning in the 410 nm Transition | 53 |
| 5.2 | Systematic Error Searches | 55 |
| 5.2.1 | Continuous Variables | 56 |
| 5.2.2 | Binary Variables | 58 |
| 5.3 | Future Work | 59 |
| 5.3.1 | Inferred $5D_{3/2}$ State Mixing | 59 |
| 5.3.2 | Polarizability in the $6P_{3/2}$ State | 60 |
| 5.3.3 | Analogous Measurements in Thallium | 60 |
| A | Spectroscopy Derivations | 62 |
| A.1 | Lifetime Broadening | 62 |
| A.2 | Doppler Broadening | 63 |
| A.3 | Single-Tone FM Lineshape Derivation | 64 |
| A.3.1 | Alternative Single-Tone Lineshape Derivation | 67 |
| A.4 | Two-Tone FM Lineshape Derivation | 68 |
| B | Three-Level System Derivations | 71 |
| B.1 | Derivation of the Three-Level Hamiltonian | 71 |
| B.2 | Stark Shift Correction Due to Doppler Shift | 74 |
| C | Mathematica Simulations | 75 |
| D | Data Analysis MATLAB Code | 81 |
| E | Measuring the Stark Effect in a $j = 3/2$ State | 87 |
| E.1 | Measuring the Indium $6P_{3/2}$ Tensor Polarizability | 87 |
| E.2 | Measuring the Thallium $7P_{3/2}$ Tensor Polarizability | 88 |

List of Figures

| | | |
|------|--|----|
| 1 | Summary of Preliminary Data | iv |
| 2 | Observation of Two-Step Excitation | v |
| 3 | Preliminary Measurement of k_S | vi |
| 1.1 | Low-lying Energy Levels of In and Tl | 4 |
| 2.1 | Comparison of Absorption Lineshapes | 10 |
| 2.2 | Single-Tone FM Demodulated Lineshape | 11 |
| 2.3 | Two-Tone FM Demodulated Lineshape | 13 |
| 2.4 | Stark Shifted Levels | 14 |
| 2.5 | Three-Level System | 16 |
| 2.6 | $\langle P_3 \rangle$ vs. Δ | 17 |
| 2.7 | Stark Shift as $\delta_3 - \delta_1$ | 19 |
| 2.8 | Deviation from $\delta_3 - \delta_1$ if Blue Frequency Fixed | 20 |
| 2.9 | Stark Shift as $\delta_3 - \delta_2$ | 21 |
| 2.10 | Lineshape for Three-Level System Transition | 22 |
| 3.1 | Full Experimental Apparatus | 24 |
| 3.2 | Diagram of Atomic Beam Unit | 26 |
| 3.3 | Geometry of Interaction Region | 27 |
| 3.4 | New Locking Scheme | 30 |
| 3.5 | Locking Signal Calibration | 32 |
| 3.6 | Unlocked vs. Locked Laser Operation | 33 |
| 3.7 | Data Acquisition Procedure | 35 |
| 4.1 | Setup for HFS Observation in Vapor Cell | 37 |
| 4.2 | Vapor Cell Observation of the $6P_{1/2}$ Spectrum | 38 |
| 4.3 | Optical Setup for Atomic Beam Unit | 39 |
| 4.4 | Atomic Beam Two-Tone Demodulated Signal | 41 |
| 4.5 | Observation of Stark Shift in ABU | 42 |
| 4.6 | Example of Collected Signals | 43 |
| 4.7 | Fit to Raw Fabry-Perot Data | 45 |
| 4.8 | Nonlinearity in PZT Scan | 46 |
| 4.9 | Frequency Calibration by EOM Sidebands | 47 |
| 4.10 | Measurement of the $6P_{1/2}$ HFS | 48 |

| | | |
|------|--|----|
| 4.11 | Overlap Method to Find Stark Shift | 49 |
| 4.12 | Shift vs. \mathcal{E}^2 | 51 |
| 4.13 | Histogram of k_S Values | 52 |
| 4.14 | Comparison of Uncertainties in Calculation and Measurement of $\alpha_0(6P_{1/2})$ | 52 |
| 5.1 | Optical Setup to Shift Blue Frequency | 54 |
| A.1 | Single-Tone Modulated Spectrum | 66 |
| A.2 | Two-Tone Modulated Spectrum | 69 |
| C.1 | Code to Simulate Laser's Electric Field | 76 |
| C.2 | Code to Simulate Laser's Spectrum | 77 |
| C.3 | Example Plot of Simulated Two-Tone Spectrum | 77 |
| C.4 | Code to Simulate the Transmitted E-Field and Intensity | 78 |
| C.5 | Code to Simulate Demodulation | 78 |
| C.6 | Code to Simulate Three-Level Hamiltonian | 79 |
| C.7 | Code to Calculate Analytic Lineshape $\langle P_3 \rangle$ | 80 |

List of Tables

2.1 Sources of Broadening 9

Chapter 1

Introduction

A physicist is just an atom's way of looking at itself.

Niels Bohr

A physicist might just be a way for atoms to look at the world they comprise, but atoms are a proven way for physicists to study the world they inhabit. Indeed, atomic systems have been some of the most fertile testing grounds for modern physical theory. Even now, a century after quantum theory began to emerge, atomic physics comprises a diverse and exciting field. From demonstrations of quantum control to the ability to test the most fundamental symmetries of nature, atoms allow us to learn a great deal about the universe. But none of these experimental feats would be possible without accurate and precise atomic theory, and no such theory could be improved without increasingly precise measurements of atomic structure. In the Majumder lab, we aim to provide high-precision measurements of atomic structure (e.g., polarizabilities, hyperfine splittings, and isotope shifts) in order to test state-of-the-art theoretical and calculation techniques.

We focus our efforts on indium and thallium— heavy atoms with three valence electrons (so-called Group IIIA atoms) where complicated, many-body physical interactions among electrons makes calculations challenging. These atoms are simple enough to allow for tractable theoretical treatments, but complicated enough to provide interesting tests of theory. Additionally, thallium has a long history of being used in important tests of fundamental symmetries of nature, especially measurements related to parity violation effects. Accurate theory is thus necessary for thallium, and because indium resides in the same group of the periodic table, both elements can be used to refine the relevant theory.

1.1 Motivation

Precision Measurements to Probe Fundamental Physics

In many cases of interest, we wish to perform measurements within an atomic sample as a means of extracting an observable produced by some fundamental physical interaction. For instance, the observable may be an optical rotation, ϵ_w , induced by the parity-nonconserving weak interaction [1]. We can separate the fundamental phenomenon from the less interesting details of the particular system being used to study it by writing

$$\epsilon_w = Q_w C(Z) \tag{1.1}$$

Here, Q_w quantifies the fundamental physics being studied, while $C(Z)$ contains the relationship between the fundamental physics and the atom used to study it. Clearly, the determined value of Q_w will depend on the uncertainties contained in *both* the experimental measurement of the observable and the theoretical calculation leading to $C(Z)$. In the case of the weak interaction, for instance, $C(Z)$ scales like Z^3 , so it is desirable to use heavy atoms—precisely those atoms for which good theory is difficult to achieve. However, only with high-precision experimental measurements *and* very accurate theory can we extract a meaningful measurement of Q_w . In the present example, stringent tests of atomic theory help push theorists to better calculations of $C(Z)$. These calculations, in turn, will reduce the overall error bar in a measurement of Q_w , the quantity of interest.

In this thesis, we are not testing fundamental symmetries of nature like in a parity nonconservation measurement. Rather, we are measuring an atomic polarizability. First and foremost, our polarizability measurements represent a stringent test of state-of-the-art atomic theory, as will be discussed below. These polarizability measurements are also, in a more indirect way, relevant to other cutting edge experimental atomic physics research. For instance, it turns out that one of the leading uncertainties for modern atomic clocks can be traced to a poor understanding of atomic polarizabilities [2]. Currently, blackbody radiation (BBR) shifts constitute the largest uncertainty in the development of new optical frequency standards. By measuring polarizabilities very precisely, and thereby pointing theorists toward the best calculation methods by which to predict these quantities, we can hope to improve the accuracy of BBR calculations. We are addressing a well-known gap in the literature: even for simple alkali atoms, polarizabilities—especially excited-state polarizabilities—have not been adequately studied [3]. Our work specifically addresses this concern.

To mention some other specific applications of research in Group IIIA atoms, we briefly note that thallium has long been a popular atomic test-bed for studying the weak interaction and parity nonconservation [4]. Indium, for its part, has been proposed as a system with which to search for a permanent electron electric dipole moment (eEDM), because it has an unusually large and precisely calculable enhancement factor [5]. In this thesis, our immediate goals are centered on atomic structure

measurements. Our aim is not to search for new physics directly, but simply to understand indium better by performing a high-precision test of its polarizability. In the long run, though, such tests are necessary to complement exciting new searches for fundamental physics.

Precision Measurements as Stringent Tests of Atomic Theory

It is an unfortunate fact that modeling heavy atoms presents many challenges to theorists. Only the lightest atom—hydrogen—has analytically solvable wavefunctions. This makes hydrogen a great testing ground for quantum theory, but a boring system when it comes to searching for new physics. In the Majumder lab, we wish to study atoms that present more of a theoretical challenge. At the same time, many theorists have undertaken the task of formulating calculation techniques to numerically solve the Schrodinger equation in heavy atomic systems. For instance, our primary collaborator over the past many years has been the group of Mariana Safronova at the University of Delaware, whose stated goal is to develop precise wavefunction calculations in atomic systems like thallium and indium. In their calculations of these wavefunctions, various computational methods can be employed, so experimental tests that can distinguish between these methods are of particular importance [6, 7].

Armed with wavefunctions from *ab initio* calculations, theorists can then predict many physically measurable quantities, including hyperfine intervals, isotope shifts, and polarizabilities. It is interesting to note that, whereas the hyperfine structure arises from electron-nucleus interactions (and is therefore relevant to short-range wavefunction behavior), polarizabilities arise from perturbation of the electronic wavefunction far from the nucleus (and therefore test long-range wavefunction behavior). Hence, tests of different theoretical predictions provide complementary information. If there is to be any hope of using heavy atoms to test fundamental physics, we must understand the “ordinary” physics well enough first. This leads to the desire to perform precise tests of these wavefunction and matrix element calculations.

1.2 Indium and Thallium

As stated above, both indium and thallium are Group IIIA elements. First, let us review their basic structure, which is already well-understood. See Figure 1.1 for a schematic energy level diagram showing several low-lying atomic states of each element. They both have three electrons in their outer shells: two paired s electrons and one unpaired p electron. This gives them their ns^2np^1 structure. Because of the similar structure, high-precision studies of indium are relevant to *both* indium and thallium. Furthermore, similar wavelengths of light can be used to excite analogous transitions in both atoms. This is of great importance to our lab, as it makes conducting many experiments with the same equipment possible.

Also shown in the energy level diagrams are the fine and hyperfine structures. For indium, the states we consider in the present experiment have total orbital angular

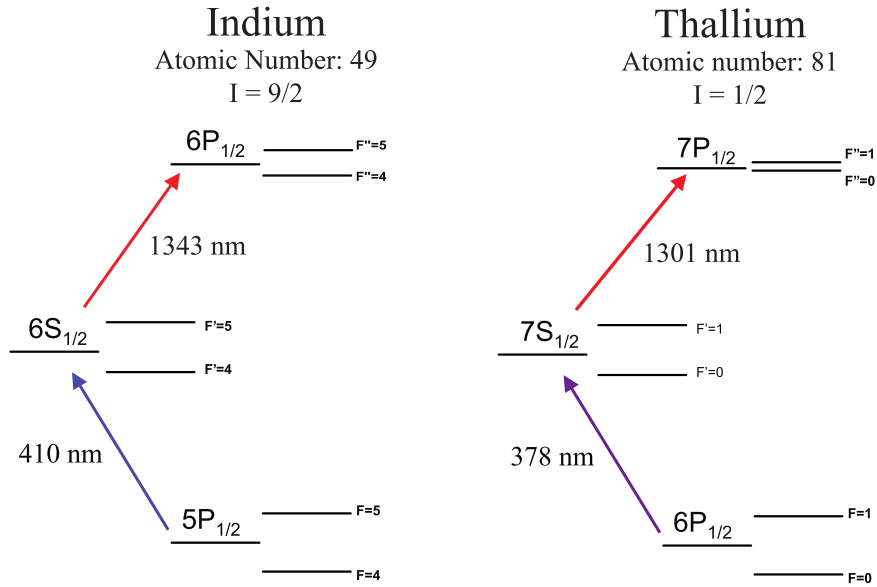


Figure 1.1: Some low-lying energy levels of both In and Tl. Both atoms have a lone p-electron which we excite using various combinations of blue, UV, and IR light. The structure of these two elements is very similar.

momentum $L = 0$ or 1 , and total spin $S = 1/2$. Therefore, the total electronic angular momentum can be either $J = 1/2$ or $3/2$. We choose to focus on the $J = 1/2$ states, as shown in the diagram. In future experiments, we will consider a $J = 3/2$ state, but that is a complication to be added later.

The nuclear spin of indium is $I = 9/2$, so when this couples to the electronic angular momentum (assumed to be $J = 1/2$ for now), we end up with $F = 4$ and $F = 5$ states in each level. The hyperfine splittings of the $5P$ and $6S$ states are both relatively large—about 11 GHz and 8 GHz, respectively. We choose to drive the first transition between the $5P_{1/2}(F = 5)$ and $6S_{1/2}(F' = 4)$ states. The hyperfine structure in the $6P_{1/2}$ state is relatively small, only about 1 GHz, so we drive transitions to both hyperfine states.

1.3 Previous Work

Over the past two decades, the Majumder lab at Williams College has undertaken a series of these high-precision measurements in atomic indium and thallium. These experiments began in thallium, with precise measurements of the electric quadrupole amplitude in the thallium $6P_{1/2} \rightarrow 6P_{3/2}$ transition, and the hyperfine structure, isotope shift, and Stark shift in the thallium $6P_{1/2} \rightarrow 7S_{1/2}$ transition [8–10]. The group then introduced indium into the lab, which among other things has the appeal of *not* being highly toxic. Analogous measurements to those completed in thallium have been undertaken in indium, culminating most recently in measurements of the

hyperfine structure within the indium $6P_{3/2}$ state and the Stark shift in the $5P_{1/2} \rightarrow 6S_{1/2}$ transition [11, 12].

In general, hyperfine and isotope shift measurements have been performed in a vapor cell environment, while Stark shift measurements have been performed in an evacuated atomic beam unit. There are advantages and disadvantages of each environment: the vapor cell provides large, broad signals; the atomic beam produces narrow, tiny signals. The atomic beam also has the advantage that we can easily apply a known, uniform electric field to induce the Stark shift in the first place. We discuss these ideas in more detail later. Several experiments in the Majumder lab, for instance [11, 13], have utilized two-step excitation schemes which have direct relevance to the present work. However, no two-step Stark shift experiment has been conducted previously by our group, so we do face some novel theoretical challenges—see Chapter 2.

1.4 Present Work

This thesis reports on the measurement of the scalar polarizability of the indium $6P_{1/2}$ state. This is the first experimental measurement of this quantity. We make the measurement by determining the Stark shift within the $5P_{1/2} \rightarrow 6S_{1/2} \rightarrow 6P_{1/2}$ two-step transition. Especially in a $J = 1/2 \rightarrow 1/2$ transition, it is possible to speak somewhat interchangeably of a Stark shift or a polarizability—one can easily convert from one to the other. However, because what we actually measure in the lab is the shift in energy levels, most of the discussions in this thesis will be in terms of Stark shifts. As will be developed in Section 2.3, this is the shift in atomic energy levels induced by an applied electric field. In many ways, the experiment can be seen as a natural combination of the two major measurement methods used by the Majumder lab in recent years: a two-step excitation scheme, but now in the atomic beam unit. Significantly, this represents the *first* time the Majumder lab has observed a multi-step transition in an atomic beam.

In truth, we can only ever measure a *difference* of Stark shifts, since each and every energy level is perturbed when an electric field is applied to the atomic sample. Therefore, the measurement we perform is of the difference of Stark shifts within the indium $6S_{1/2} \rightarrow 6P_{1/2}$ 1343 nm transition. However, the Stark shift within the $5P_{1/2} \rightarrow 6S_{1/2}$ has already been measured very accurately in [12], and the uncertainty in the calculation of the $5P_{1/2}$ polarizability is so small that we can take the theoretical value to be essentially exact. Hence, a precise measurement of the Stark shift within the transition being studied will unambiguously determine the value of the polarizability of the $6P_{1/2}$ excited state. Due to the nearby $5D_{3/2}$ state, this is a very good test of atomic theory (see Section 2.3).

Throughout this thesis, we will use the following notation: the Stark shift within an *individual* level will be referred to as δ_i , where i is some representation of the state. When using this notation, we will refer to the $5P_{1/2}$ state as $i = 1$, the $6S_{1/2}$ state as $i = 2$, and the $6P_{1/2}$ state as $i = 3$. To denote the *difference* between

Stark shifts in any two levels, we will use Δ_{ij} where i and j each represent a single state. For example, the difference between the third and first states would be written $\Delta_{31} \equiv \delta_3 - \delta_1$. Though not necessarily standard, this notation is very useful for our purposes.

Over the course of this thesis, we realized that it is also possible to obtain a precise measurement of the hyperfine structure within the indium $6P_{1/2}$ state “for free” based on the scheme we use to calibrate the frequency axis during data analysis. For this reason, we undertake this hyperfine splitting measurement concurrently. See Section 4.2.4 for details. As was described above, it is nice to note how the hyperfine and Stark shift measurements complement one another, with the former testing short-range wavefunction calculations and the latter testing long-range wavefunction calculations.

1.5 Outline of This Thesis

This thesis describes the first measurements of the Stark shift within the two-step $5P_{1/2} \rightarrow 6S_{1/2} \rightarrow 6P_{1/2}$ transition in indium. Chapter 2 introduces the basic concepts of absorption spectroscopy, describes the frequency modulation (FM) spectroscopy used throughout this experiment, and derives the Stark shift from second-order perturbation theory. It then moves on to describe the quantum theory of three-level systems relevant to our experiment. This theoretical project was a major step necessary to interpret the results obtained during the past year. Chapter 3 describes the experimental apparatus used to conduct this experiment. It also introduces a new method of laser stabilization developed over the course of this thesis. An overview of the newly observed two-step transition and the data analysis procedure is given in Chapter 4. Next, Chapter 5 describes the preliminary results we have obtained, and the work that remains to complete this Stark shift measurement. Appendix A contains derivations relevant to the discussions of laser and FM spectroscopy. Appendix B contains derivations related to the three-level system dynamics. Appendices C and D contain details about numerical simulations of the FM and atomic theory, and MATLAB code used for data analysis, respectively. Finally, Appendix E works out the theory of potential future measurements of tensor polarizabilities in the indium $6P_{3/2}$ and thallium $7P_{3/2}$ states.

Chapter 2

Atomic Spectroscopy and Theory

We turn now to the theoretical underpinnings of this experiment. We first review the basics of absorption spectroscopy and quote the lineshapes we expect to observe when we use lasers to probe atomic samples. Next, we present the basic lineshapes of frequency modulation (FM) spectroscopy, which is used extensively throughout this experiment. We then describe the Stark shift as it arises from second-order perturbation theory. Because the basic ideas of these topics are relatively standard, we present only the essential results here. Relevant derivations can all be found in Appendices A and B. Finally, we consider complications due to the three-level nature of the transition being studied. This is a fundamentally new theoretical project for the Majumder lab, so we discuss the three-level results in some detail.

2.1 Absorption Spectroscopy

We probe our atoms by shining lasers through an atomic vapor and measuring the amount of light transmitted. When the laser outputs photons of energy very near the energy splitting between two atomic energy levels, these photons are likely to be absorbed by an intervening atom and re-radiated isotropically. The transmitted intensity will thus be lower than when the laser is tuned far from an atomic resonance. By locating the center of these absorption features, we can locate individual energy levels. Of particular interest to this thesis is not merely locating the position of a resonance, but also measuring how it *changes* when an external electric field is applied. The more precisely we can locate a transition, the more precisely we can measure this shift.

Mathematically, the fundamental idea of absorption spectroscopy is that if we interact a laser beam of intensity I and frequency ω with a sample of atoms of thickness dz , the intensity of the light will decrease by the amount $dI = -A(\omega)Idz$. Here, $A(\omega)$ represents the probability that the atoms will absorb light of frequency ω . It is conventional to write $A(\omega) = \alpha P(\omega)$, where α is the atomic sample's *optical depth* (characterizing how strongly the light is absorbed) and $P(\omega)$ is a normalized

probability of absorption (= 1 on resonance). This is easily integrated to reveal the transmitted intensity, $I(\omega, z)$:

$$I(\omega, z) = I_0 e^{-\alpha P(\omega)} \quad (2.1)$$

In a very general sense, measuring this $I(\omega, z)$ is how we obtain any and all data about the atoms studied in this thesis. As will be discussed in Chapter 3, we typically observe values of α in the 10^{-3} range or lower, leading to the necessity of sophisticated detection techniques like FM spectroscopy. As for $P(\omega)$, we typically observe significant levels of absorption spread over many MHz, or even many GHz, about the actual atomic resonance. Such *lineshape broadening* can be caused by many factors, but two are of particular importance to the present experiment: the finite lifetime of any atomic state, and the motion of atoms along the laser beam.

Lifetime Broadening

All excited atomic states eventually decay into a state of lower energy. Whether this decay happens over relatively short or long times varies from species to species, but no excited state is infinitely long-lived. Through the Heisenberg Uncertainty Principle, this finite lifetime gives rise to a *Lorentzian* lineshape of full-width-at-half-maximum (FWHM) Γ , which is a measure of how “narrow” the state is and is inversely proportional to the state’s lifetime (see Section A.1). In the case of the indium, these lifetimes include $\tau_{6S_{1/2}} \approx 7$ ns and $\tau_{6P_{1/2}} \approx 55$ ns (where it is assumed that the decays are $6S_{1/2} \rightarrow 5P_{1/2}$ and $6P_{1/2} \rightarrow 6S_{1/2}$, respectively) [14]. Based on Equation A.1, these correspond to $\Gamma_{6S_{1/2}} \approx 22$ MHz and $\Gamma_{6P_{1/2}} \approx 3$ MHz. It should be noted that this is an example of *homogeneous broadening*, so these widths are characteristic of *any* indium atom, regardless of how it is behaving.

Doppler Broadening

In addition to the natural lifetime detailed above, there is also a broadening due to the motion of atoms relative to the laser beam probing them. As discussed in Section A.2, when the atomic sample obeys a Maxwell-Boltzmann distribution, this sort of broadening gives rise to a *Gaussian* lineshape of width Δ . This width is proportional to the transition frequency and the square root of the sample’s temperature, but inversely proportional to the square root of the atomic mass. To put in numbers representative of the indium $5P_{1/2} \rightarrow 6S_{1/2}$ transition we study in the vapor cell, assume $T = 730^\circ\text{C}$, $\omega_0/2\pi = 730673$ GHz, and $m = 115$ amu, yielding $\Delta \approx 1.6$ GHz. As will be seen, in the vapor cell, this is nearly two orders of magnitude larger than any other source of broadening. One of the advantages of performing our experiment in an atomic beam, then, is a drastic reduction of this width by several orders of magnitude (see Chapter 3). Doppler broadening is a sort of *inhomogeneous broadening* in that it partitions atoms into different “velocity classes” depending on their individual motions.

Lineshapes Relevant to this Thesis

Lifetime and Doppler broadening are not the only sources of broadening, but they are the predominant ones in the regime in which the present experiment is conducted. Table 2.1 outlines the approximate sizes of many sources of broadening within the indium $5P_{1/2} \rightarrow 6S_{1/2}$ transition [15]. One major difference is that we have increased the contribution from power broadening to be about 20 MHz, in both vapor cell and atomic beam environments.¹ This is based on the known matrix element connecting the $5P_{1/2}$ and $6S_{1/2}$ states, as well as the approximate blue laser power. Issues concerning Rabi frequencies will be explored more below, and can introduce both broadening and, in extreme cases, splitting of lines in a two-step transition. In order to ensure these effects do not lead to systematic uncertainties, we check our results at various blue and IR powers.

Finally, we should note that the proper way to model the absorption signal of an atomic sample broadened by both Gaussian and Lorentzian profiles is to consider the convolution of these two functions, the so-called Voigt profile. However, computing the Voigt profile is a computationally intensive process. In the past, it has not had a significant effect on the precision or accuracy of measured values [15], so we often simply model our signals as Gaussians (Lorentzians) in the vapor cell (atomic beam). For completeness, we show a comparison of Gaussian, Lorentzian, and Voigt profiles in Figure 2.1.

| Broadening Mechanism | FWHM | |
|--------------------------------|------------|-------------|
| | Vapor Cell | Atomic Beam |
| Natural Width | 21 MHz | 21 MHz |
| Doppler Broadening | 1.4 GHz | 70 MHz |
| Laser Line-width | 2 MHz | 2 MHz |
| Pressure Broadening | 10 kHz | 0 kHz |
| Power Broadening | 20 MHz | 20 MHz |
| Transit-Time Broadening | 480 kHz | 550 kHz |
| <i>Voigt Convolution Total</i> | 1.4 GHz | 103 MHz |

Table 2.1: A comparison of potential sources of broadening for the $5P_{1/2} \rightarrow 6S_{1/2}$ transition in indium at representative experimental conditions. This table is reproduced from [15].

2.2 Frequency Modulation

Having discussed the basics of atomic absorption above, we still face an experimental challenge: it is prohibitively difficult to induce detectable amounts of absorption in our

¹Power broadening, of course, depends on the operating conditions of the laser; for this calculation, we assumed representative parameters of a 5 mm beam waist and power of about 1 mW for the 410 nm laser.

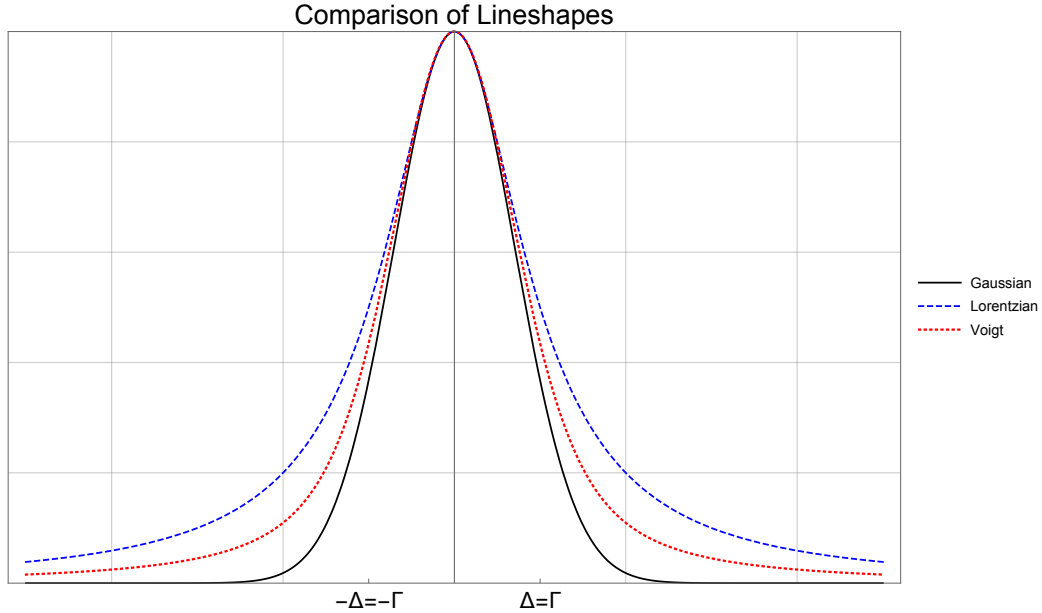


Figure 2.1: Examples of Gaussian, Lorentzian, and Voigt absorption profiles. For this example, it was assumed that the Gaussian and Lorentzian lineshapes both have equal widths. Notice that the main difference between the lineshapes comes in the tails.

atomic beam of indium. Luckily, the Majumder lab has extensive experience with an alternative detection method known as frequency modulation (FM) spectroscopy. FM spectroscopy involves modulating the laser frequency at some well-known frequency and using that modulation as a marker so that the detection electronics (a lock-in amplifier) know “where” in frequency space to look for a useful signal. Any signal not oscillating at the modulation frequency is ignored— ideally, there is no (or at least very little) background. Hence, our experimental task changes from detecting a small signal on top of a large background to detecting a signal on top of zero background. This is a much more manageable task. The demodulated lineshape that comes from this process is the signal that is actually studied in an FM experiment.

For our purposes, FM spectroscopy comes in two forms: (1) single-tone FM spectroscopy and (2) two-tone FM spectroscopy. Each of these has been used in previous experiments in the Majumder lab (see [15, 16] for single-tone and [17, 18] for two-tone experiments). However, in the present experiment we make use of *both* varieties, albeit for vastly different purposes: single-tone FM as a method of laser stabilization and two-tone FM as a way to detect the Stark shift. We discuss the lineshapes arising in each form of FM spectroscopy here, leaving their derivations to Appendix A.

2.2.1 Single-Tone FM Spectroscopy

Single-tone FM spectroscopy involves modulating the laser field at a chosen frequency, ω_m , allowing the beam to interact with an atomic sample, and then demodulating the transmitted light so as to consider only that portion of the light which is oscillating

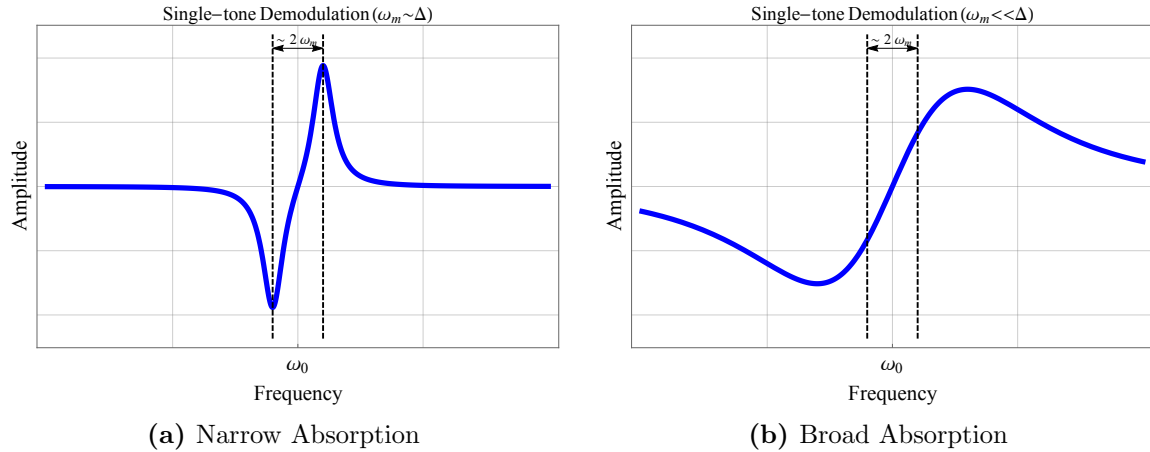


Figure 2.2: Example single-tone FM demodulations (a) when the atomic width is of the same order as ω_m , and (b) when the atomic width is much larger than ω_m . The former is roughly what we observe in the atomic beam, and the latter is roughly what we observe in the vapor cell. See Chapter 3 for details.

at ω_m . Typically, by choosing ω_m to be very high (in the kHz or MHz range), many ordinary sources of noise can be reduced due to their relatively low frequencies—demodulation will reject all low-frequency contributions. The experimental realization of this is described in Sections 3.2.2 and 3.2.3.²

Suppose we send a single-mode laser beam through an EOM, pass it through some atomic sample, and then detect it by using a lock-in amplifier referenced to ω_m . Then the demodulated intensity will be

$$I_{\text{demod}}^{\text{single-tone}} \propto T^2(\omega_c + \omega_m) - T^2(\omega_c - \omega_m) \quad (2.2)$$

where T is the frequency-dependent transmission factor and the modulation depth is assumed to be small. This is the fundamental results of single-tone FM spectroscopy and is derived in Section A.3. It says that the detected signal will be proportional to the differential absorption of the two sidebands in the laser spectrum.

In Figure 2.2, we plot simulated single-tone demodulated spectra for two specific cases of atomic absorption. In the Figure 2.2a, we plot the case when $\omega_m \sim \Delta$. The two peaks are separated by close to, but not exactly, $2\omega_m$. In Chapter 3 it will be seen that this case corresponds closely to the atomic beam signal. In Figure 2.2b, we plot the case where $\omega_m \ll \Delta$. Then the two peaks are largely overlapping and the peaks are separated by much more than $2\omega_m$. We will see later that this models the sort of signal seen in the vapor cell. It also represents a useful locking signal, as will be discussed in Section 3.2.2.

²Briefly, we use an electro-optic modulator, or EOM, to modulate the laser beam and a lock-in amplifier to demodulate the transmitted intensity signal.

2.2.2 Two-Tone FM Spectroscopy

In this experiment, a second type of FM spectroscopy is used to extract the experimental signal by which the Stark shift is measured. This technique involves modulating the laser at *two* frequencies, and is fittingly known as two-tone FM spectroscopy. First introduced in [19], it has been used in various experiments within the Majumder lab (see, for instance, [18]).³ Its great value is that we may modulate a laser beam at a very high frequency to decrease potential sources of noise, but demodulate the signal at a relatively low frequency where IR detection electronics and lock-in amplifiers are cheaper and readily available. In addition to these technological appeals, two-tone FM methods offer some advantages in terms of reducing spurious signals or small offsets in the single-tone demodulated signal [15].

In a two-tone FM spectroscopy scheme we modulate the laser frequency at the two nearby frequencies $\omega_m + \Omega/2$ and $\omega_m - \Omega/2$. It is assumed that ω_m is very large (600 MHz for us) compared to Ω (100 kHz), and that Ω is very narrow compared to the width of the transition being probed. After the laser interacts with an atomic sample, we demodulate at Ω via a lock-in amplifier. The fundamental lineshape of two-tone FM spectroscopy is

$$I_{\text{demod}}^{\text{two-tone}} \propto 2T^2(\omega_c) - T^2(\omega_c - \omega_m) - T^2(\omega_c + \omega_m) \quad (2.3)$$

Whereas the demodulated lineshape of single-tone FM spectroscopy shows a characteristic double-peaked function, the two-tone FM spectroscopic lineshape shows *three* peaks. There is one upward-going peak at the actual resonance, with two downward-going sidebands spaced by exactly ω_m on either side of it. The derivation of this lineshape is left to Section A.4. In Figure 2.3a, a sample two-tone FM spectrum is shown. This is not actually what we observe when we run the experiment. Due to the small hyperfine splitting within the indium $6P_{1/2}$ state, we observe two copies of the two-tone FM lineshape spaced by roughly 1 GHz. Figure 2.3b simulates the signal we expect to observe. It contains six peaks (three per hyperfine transition), even though only five are clearly resolved. As will be explained in Chapter 3, the choice of experimental parameters is what causes these two signals to have overlapping sidebands.

2.3 The Stark Shift

At a fundamental level, this thesis asks the question: how do indium atoms respond to an externally applied electric field? We will find that, upon applying electric fields of order 10 kV/cm to the atoms, the atomic energy levels decrease in energy by an amount proportional to the *square* of the applied field (see Figure 2.4). This is called the (quadratic) Stark shift. In indium, with its atomic radius of about 167 pm, the outermost electron experiences an electric field of roughly 5×10^7 kV/cm. The fields we apply in the lab are clearly orders of magnitude smaller than this intrinsic electric

³I would be remiss if I did not point out the Eph who co-authored the original two-tone FM paper: Professor Tom Gallagher graduated from Williams College in 1966.

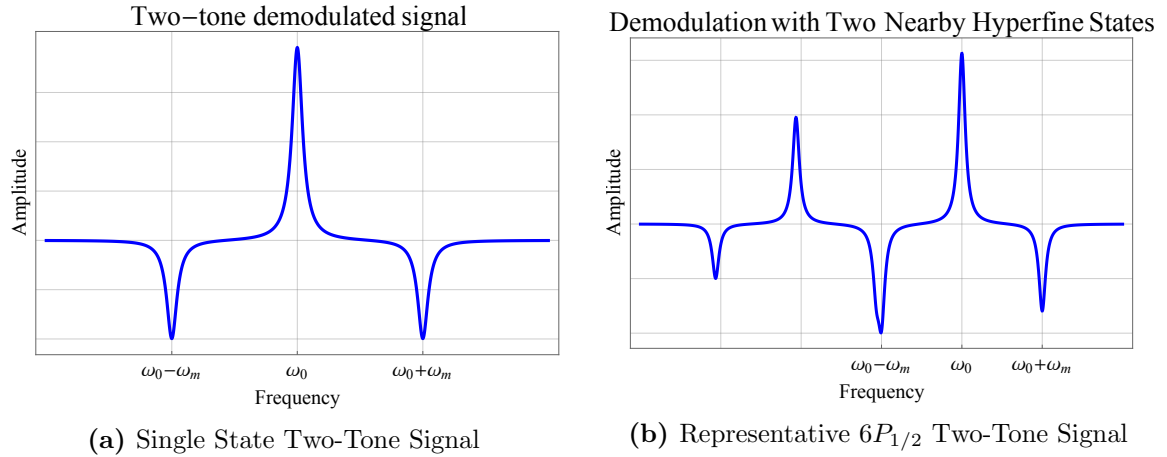


Figure 2.3: (a) A typical two-tone FM demodulated signal. It consists of two downward-going sidebands spaced precisely ω_m on either side of a central upward going peak. (b) A more representative plot of what we observe in the atomic beam shows two copies of this lineshape, overlapping slightly. The two copies differ in size due to the relative strengths of the two transitions being driven.

field, and we are justified in applying perturbation theory to derive the effect these applied fields will have on the atomic energy levels. The perturbation due to the electric field is

$$\hat{H}' = q\vec{\mathcal{E}} \cdot \vec{r} = q\mathcal{E}z \quad (2.4)$$

where q is the electron charge and we have chosen the electric field to lie entirely along the z -axis. Turning to first-order perturbation theory, we see that due to parity there is *no* linear shift in the applied electric field:

$$\Delta E_\eta^{(1)} = q\mathcal{E} \langle \psi_\eta^{(0)} | z | \psi_\eta^{(0)} \rangle \quad (2.5)$$

$$\propto \int_{-\infty}^{\infty} |\psi_\eta^{(0)}|^2 z dz \quad (2.6)$$

$$= 0 \quad (2.7)$$

Here, and in what follows, we denote energy by E , so as not to confuse it with electric field, \mathcal{E} . We index states by the subscript η , and we denote the order of perturbation by a superscript. With no linear Stark shift, we move on to second-order perturbation theory⁴ and look for a quadratic effect. In general, we have

⁴It is completely justified to apply *non-degenerate* perturbation theory: hyperfine splittings in indium are typically of order GHz and the atoms are distributed thermally among the $2F + 1$ degenerate magnetic sublevels; for instance, we make no effort to optically pump the atoms. Thus, the excitations can be treated like a statistical average over the various m_F states, which shift by the same amount for the case of scalar polarizability anyway.

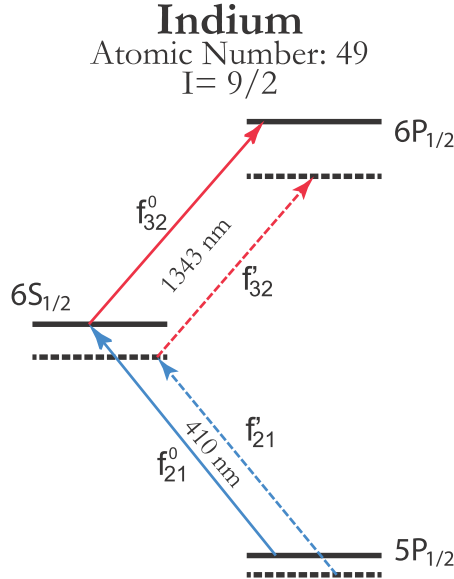


Figure 2.4: Schematic diagram of the energy levels of interest to this thesis, in both field-off (solid) and field-on (dashed) configurations. As expected, higher energy levels shift by larger amounts for any given electric field, and all states shift to lower energies. Frequencies f^0 correspond to field-off transition frequencies, while f' corresponds to field-on transition frequencies.

$$\Delta E_{\eta}^{(2)} = \sum_{\nu \neq \eta} \frac{|\langle \psi_{\nu}^{(0)} | q\mathcal{E}z | \psi_{\eta}^{(0)} \rangle|^2}{E_{\nu}^{(0)} - E_{\eta}^{(0)}} \quad (2.8)$$

$$\equiv -\frac{1}{2}\alpha_0(\eta)\mathcal{E}^2 \quad (2.9)$$

The first equality shows that higher energy levels will shift by larger amounts due to the more densely packed states at higher energies. In the second equality, we have pulled out the electric field dependence, and introduced the polarizability, α_0 (the factor of $\frac{1}{2}$ is conventional). This factor of α_0 characterizes how the state responds to an applied electric field. The polarizability is in general a tensor, depending on the relative polarization between the static electric field and the resonant laser field exciting a transition. For the $j = \frac{1}{2}$ states considered in this thesis, there is only a scalar polarizability. Note that α_0 is state-dependent. Luckily, then, each level shifts by a different amount: if two levels shifted by the same amount, it would be impossible to detect the electric field's effect, as the same laser light would excite transitions regardless of whether the field were on or off.

When we probe a particular transition in our experiment, we measure the *difference* in polarizability between the two states in that transition. For instance, in the 410 nm $5P_{1/2} \rightarrow 6S_{1/2}$ transition, we would find:

$$\Delta f_S = -\frac{1}{2h} \{ \alpha_0(6S_{1/2}) - \alpha_0(5P_{1/2}) \} \mathcal{E}^2 \quad (2.10)$$

$$= k_S \mathcal{E}^2 \quad (2.11)$$

In our experiment, we can easily measure how the line center of this IR transition changes as a function of applied electric field. Plotting the measured shift versus \mathcal{E}^2 and determining the slope of the resulting line immediately reveals k_S .⁵ Most importantly, this is a good test of atomic theory because accurate atomic wavefunction calculations are necessary to predict α_0 for each state—recall that the polarizability is defined in terms of the matrix elements in Equation 2.8. Furthermore, for the case of the $6P_{1/2}$ state, the largest term in the sum is the nearby $5D_{3/2}$ state. D -states are notoriously difficult to model, so our precision measurement of the polarizability is of great value to theorists trying to do so.

2.4 The Stark Shift in a Two-Step Transition

We undertook this experiment imagining that one laser (at 410 nm) simply pumps atoms into an intermediate state, populating it with atoms available for excitation by a second laser (at 1343 nm). Therefore, when an electric field is applied we believed that the detected shift in resonance frequency of the IR laser would correspond to the difference in Stark shifts between the second and third states. In some sense, the end result is true—but we must understand the process quantum mechanically. We need to think more carefully about how we measure the Stark shift in a two-step transition.⁶

Because we overlap two lasers such that atoms interact with *both* laser fields simultaneously, we are effectively coupling three atomic energy levels by two near-resonant fields. This means the naive picture of two independent transitions is simply wrong. We will see that, so long as we require the blue laser *always* be on resonance with the first transition when an electric field is applied (i.e., as long as we tune it to the location of the Stark-shifted transition), then the resonance in the IR laser will occur at a frequency corresponding to the difference between the second and third energy levels. Hence, we measure the difference in Stark shifts between these two upper levels (see Section 2.4.3). But, we can also perform the measurement in such a way as to measure the difference in shifts between the *first* and third states (see Section 2.4.2). Because the Stark shift within the lower level was measured to very high precision in [12], we will unambiguously determine the Stark shift in the third state with the present measurement.

⁵To convert a given k_S in $\frac{\text{kHz}}{(\text{kV}/\text{cm})^2}$ into a difference of polarizabilities in a_0^3 , simply multiply the numerical value of k_S by 8.136. This conversion takes us from SI units to atomic units, where $h = 1$ so that Δf and ΔE are equivalent.

⁶Professor Fred Strauch [20] was particularly helpful in working through the three-level quantum mechanics with us, most especially in understanding the lineshapes to be discussed below.

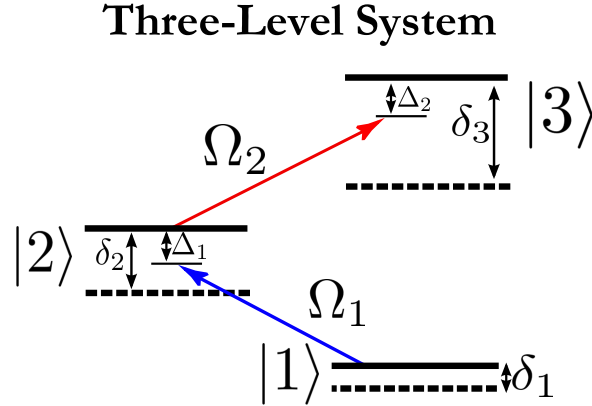


Figure 2.5: Schematic energy level drawing of a three-level system in the “cascade” configuration. We assume that the states $|i\rangle$ and $|j\rangle$ are coupled by light with frequency near $(E_j - E_i)/\hbar$ and Rabi frequency Ω_k . We also show (dashed lines) the possibility that each level is shifted from its unperturbed location (solid lines) by δ_i ($i = 1, 2, 3$), representing a Stark shift. We allow some overall detuning Δ_j ($j = 1, 2$) from the location of that level, which we control by tuning each laser.

Luckily, three-level systems constitute a classic problem in quantum optics (see, for instance, [21–23]). Unluckily, this problem is vastly more difficult than solving the dynamics of a two-level system, which can be easily handled analytically. Here, we use a “quantum optics” style argument to derive the resonance condition when a three-level system is simultaneously irradiated by two laser fields.

2.4.1 Three-Level Resonance

The three-level system we wish to study is shown schematically in Figure 2.5. There are three states, $|1\rangle$, $|2\rangle$, and $|3\rangle$ with energies E_1 , E_2 , and E_3 , respectively. The lower two (upper two) states are coupled by a laser field of Rabi frequency Ω_1 (Ω_2). When an electric field is applied, the i^{th} state shifts down by some Stark shift δ_i . Finally, each laser may be tuned from the j^{th} transition by Δ_j . Given these stipulations, the Hamiltonian representing the dynamics of this system is:

$$H_{\text{RWA}} = \begin{pmatrix} 0 & \Omega_1 & 0 \\ \Omega_1 & \Delta_1 - (\delta_2 - \delta_1) & \Omega_2 \\ 0 & \Omega_2 & \Delta_2 + \Delta_1 - (\delta_3 - \delta_1) \end{pmatrix} \quad (2.12)$$

This is the general form of the Hamiltonian we must study. It is derived in Section B.1 via a rotating wave approximation. We move on now to determine the relevant resonance conditions.

Assuming all atoms start in the ground state, the probability of excitation to the third state, P_3 , can be expressed as $P_3 = |\langle 3| e^{-iH_{\text{RWA}}t/\hbar} |1\rangle|^2$. Given eigenstates and eigenenergies of H_{RWA} , $|v_j\rangle$ and E_j ($j = 1$ through 3), we can invoke the decomposition

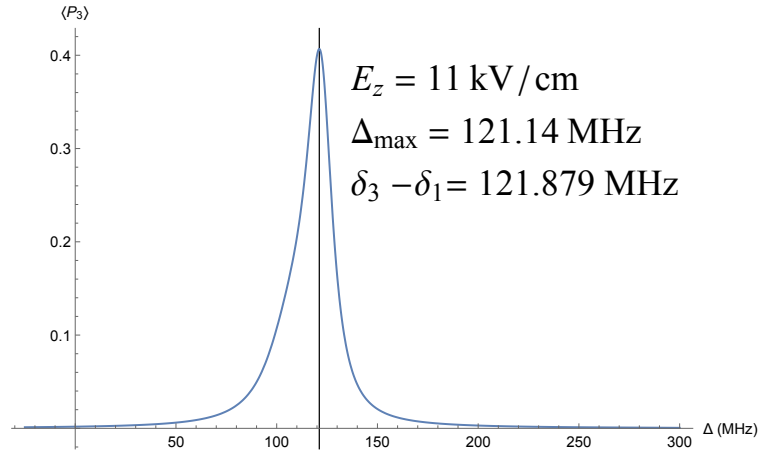


Figure 2.6: Probability of exciting the atom to state $|3\rangle$ as a function of the IR laser detuning, Δ . The peak corresponds to the location of the resonance in the presence of an applied electric field— i.e., it *is* the Stark shift for that field value.

$$\langle 3| e^{-iH_{\text{RWAt}}/\hbar} |1\rangle = \sum_{j=1}^3 \langle 3|v_j\rangle \langle v_j|1\rangle e^{-iE_j t/\hbar} \quad (2.13)$$

$$\Rightarrow P_3 = \sum_{j=1}^3 \sum_{j'=1}^3 \langle 3|v_j\rangle \langle v_j|1\rangle e^{-iE_j t/\hbar} e^{iE_{j'} t/\hbar} \langle 1|v_{j'}\rangle \langle v_{j'}|3\rangle \quad (2.14)$$

However, since we measure the absorption continuously, we essentially want to take a time-average of this probability. Doing so amounts to integrating P_3 over a long time period (and dividing by that length of time), which is mathematically equivalent to setting the product of the time-dependent complex exponentials equal to the Kronecker delta $\delta_{j,j'}$.⁷ Hence, the double sum collapses into a single sum which expresses the probability of excitation to the upper state:

$$\langle P_3 \rangle = \sum_{j=1}^3 |\langle 3|v_j\rangle \langle v_j|1\rangle|^2 \quad (2.15)$$

We want to model this probability as a function of Δ_2 . We wish to find how the peak of $\langle P_3 \rangle$ shifts when the electric field is on and turn that information into a quoted Stark shift. As an example, see Figure 2.6. Technically, one can do this by diagonalizing the Hamiltonian analytically, but working numerically is also possible and often more enlightening. Appendix C contains Mathematica code which allows for such numerical simulations; the results are summarized here.

There are essentially two experimental regimes in which we can work: (1) locking the blue laser to a field-free resonance and doing nothing else, or (2) locking the blue

⁷Put another way, the sum's cross-terms, which were the things causing any time-dependence in the first place, are all set to zero.

laser to a field-free resonance and then shifting it in frequency by $\delta_2 - \delta_1$ so that it always remains resonant with the atomic beam when an electric field is applied. These two conditions give rise to different spectra and observed Stark shifts, which we describe here.

2.4.2 Blue Laser Always Resonant with Field-Free Sample

Suppose we stabilize the blue laser driving the $5P_{1/2} \rightarrow 6S_{1/2}$ transition to a sample of atoms in a field-free region and send this stabilized frequency into the atomic beam sample. That is, $\Delta_1 \equiv 0$, and Equation 2.12 yields the Hamiltonian

$$H_{\text{RWA}} = \begin{pmatrix} 0 & \Omega_1 & 0 \\ \Omega_1 & -(\delta_2 - \delta_1) & \Omega_2 \\ 0 & \Omega_2 & \Delta_2 - (\delta_3 - \delta_1) \end{pmatrix} \quad (2.16)$$

When we apply the electric field to the atomic beam, the first-step transition is slightly off resonance (because in the atomic beam, *all* energy levels shift). In the atomic beam, we thus excite atoms whose motion along the laser beam causes a Doppler shift bringing them *back* into resonance with the blue beam. Because only these atoms are available for excitation to the $6P_{1/2}$ state, that transition will again take place at a Doppler-shifted frequency. The necessary correction is derived in Section B.2 as:

$$|\Delta_{32}| = (f_{32}^0 - f'_{32}) + |\Delta_{21}| \frac{f_{32}^0}{f_{21}^0} \quad (2.17)$$

The peak of $\langle P_3 \rangle$, given the RWA Hamiltonian in Equation 2.16, occurs at $f_{32}^0 - f'_{32}$, so we simply add on the small correction term to determine Δ_{32} . Because of the high-precision measurement of Δ_{21} in [15], we can do so with no overall loss of overall precision.

It is interesting to note that, as the applied electric field becomes larger, the first-step transition becomes more and more “virtual,” due to the fact that the detuning (relative to the Rabi frequency of that transition) increases. At large enough fields, we can drive a two-photon transition in which the intermediate state effectively drops out of the physical picture. Hence, we would expect to observe a Stark shift that is very much like $\delta_3 - \delta_1$ in this regime. Numerical results show that this is true. In Figure 2.7, we show the fractional difference between the numerically computed peak of $\langle P_3 \rangle$ and the exact value of $\delta_3 - \delta_1$ as a function of applied electric field for several potential Rabi frequencies. As can be seen, the agreement is good but never perfect.

Unfortunately, how quickly the fractional difference drops off is dependent on the Rabi frequencies of both transitions; since we cannot measure these, we can never be sure exactly how to simulate the resonance numerically. However, based on the computed E1 matrix elements in [6] and the measured laser powers, we can estimate that the Rabi frequencies for both transitions will be somewhere between 20 and 50 MHz. As shown in Figure 2.7, in this range of parameters we expect to observe a

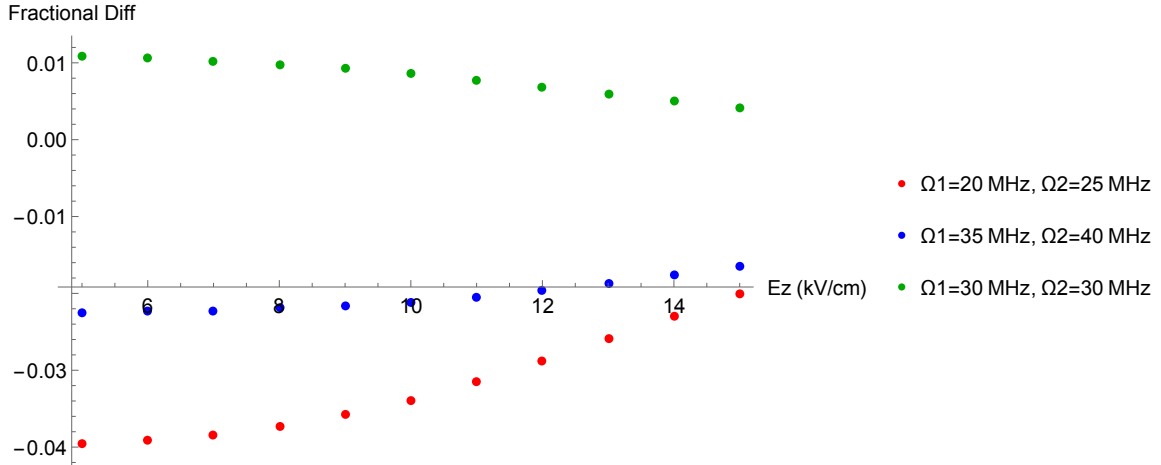


Figure 2.7: Case of *fixed* blue laser frequency: Fractional difference between a numerically calculated Stark shift and the exact difference in shifts between the third and first states, i.e. $\delta_3 - \delta_1$. Shown are three representative examples near the range of laser powers and applied HV we realize experimentally. In all cases, the disagreement from $\delta_3 - \delta_1$ is less than 4%.

shift close to the difference in Stark shifts between the third and first levels, although we cannot claim to measure *exactly* that difference. In that particular figure we chose representative Rabi frequencies and plotted the deviation versus electric field.

We can also choose a particular electric field value and plot the deviation versus the two Rabi frequencies; we do so as a surface plot in Figure 2.8. In that curve, there is a clear trough for which the shift we observe would be very nearly equal to $\delta_3 - \delta_1$, just as demonstrated above. This trough occurs in the regime where $\Omega_1 = \Omega_2$, i.e. where the Rabi frequencies of the two transitions are equal. This can be understood intuitively as due to two AC Stark shifts of opposite direction being induced by both the blue and IR lasers being slightly off-resonant with the ABU atoms; the AC shifts happen to cancel for equal Rabi frequencies. Note that, going along with our idea that the lower transition becomes more “virtual” as electric field increases, surfaces for higher fields lie below surfaces for lower fields. Given our experimental parameters, the preliminary data was collected near the trough of these surfaces.

When we collect data in this configuration, we have to claim a roughly 4-5% systematic uncertainty because of our inability to model this situation exactly. This is not the ideal way to conduct a final measurement. However, as will be noted in Chapter 5, when we actually perform the measurement in this way, we do not observe a 4% variation in the value of k_S as a function of \mathcal{E} . This gives us confidence that we are not dealing with the worst case scenario— but that discussion will be deferred for now. We will instead discuss the second, alternative measurement scheme.

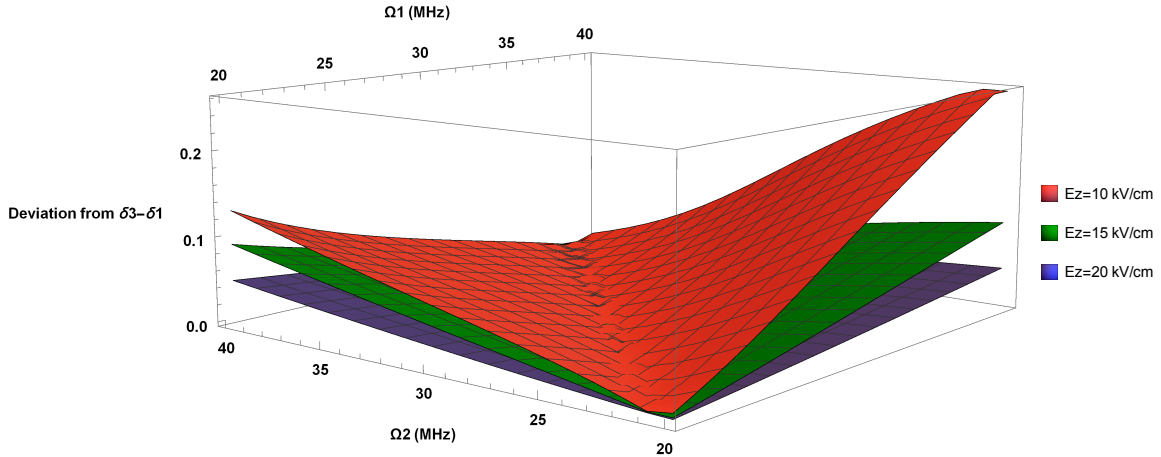


Figure 2.8: Case of *fixed* blue laser frequency: Fractional difference between a numerically calculated Stark shift and the exact difference in shifts between the third and first states, as a function of Rabi frequencies of both lasers. We plot the case of $\mathcal{E} = 10, 15,$ and 20 kV/cm. For larger fields, the maximum deviation decreases, as expected. The actual experimental regime places us near the trough of the curves.

2.4.3 Blue Laser Always Resonant with Atomic Beam

Suppose, instead, that we require that the frequency of the laser driving the $|1\rangle \rightarrow |2\rangle$ transition is always on resonance with atoms in the electric field region. That is, we track the Stark-shifted resonance frequency so that the laser always excites the zero-velocity class of atoms in the electric field. Mathematically, then, $\Delta_1 \equiv (\delta_2 - \delta_1)$ is always satisfied. With this condition, Equation 2.12 gives the Hamiltonian

$$H_{\text{RWA}} = \hbar \begin{pmatrix} 0 & \Omega_1 & 0 \\ \Omega_1 & 0 & \Omega_2 \\ 0 & \Omega_2 & \Delta_2 - (\delta_3 - \delta_2) \end{pmatrix} \quad (2.18)$$

By staying resonant with the Stark-shifted levels, the first transition never becomes “virtual,” so we expect the measured shift to be $\Delta_{32} = \delta_3 - \delta_2$. This can also be seen by equating the first and last diagonal elements of the Hamiltonian to determine the resonance condition. Furthermore, we do not need to worry about a Doppler shift correction as we did in Section 2.4.2, since we always excite the zero velocity class of atoms in the atomic beam.

It is possible to show numerically that, if we remain resonant with the atomic beam sample, then the Stark shift we measure will be the difference in Stark shifts between the third and second states. To do so, we simulate Equation 2.18 in Mathematica and compute the fractional difference between the calculated peak of $\langle P_3 \rangle$ and the exact value of $\delta_3 - \delta_2$. A plot of the result versus electric field value is shown in Figure 2.9 for the same three example Rabi frequencies used in Figure 2.7. Given our experimental precision, the observed shift is essentially exactly equal to $\Delta_{32} = \delta_3 - \delta_2$. Furthermore, there is no clear systematic dependence on the Rabi frequency of either laser, which

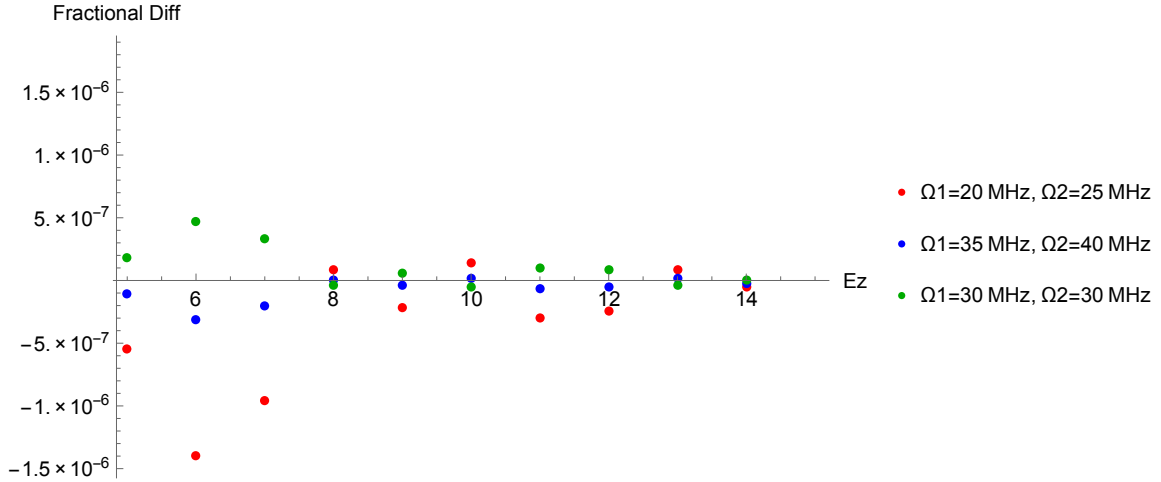


Figure 2.9: Case of tuning blue laser to stay resonant with atomic beam: Fractional difference between a numerically calculated Stark shift and the exact difference in shifts between the third and second states, i.e. $\delta_3 - \delta_2$, for Rabi frequencies near our experimental regime. The agreement is essentially exact, given our experimental precision.

is extremely useful given our inability to measure them. Therefore, carrying out our experiment while requiring $\Delta_1 = \delta_2 - \delta_1$, we can expect to measure exactly the Stark shift difference $\Delta_{32} = \delta_3 - \delta_2$.

Analytic Lineshape

We can also derive the analytic lineshape for the probability of excitation to the third state, $\langle P_3 \rangle$, in the case where the first transition is always resonant. The details of the analytic calculation are shown in the relevant Mathematica code in Appendix C. The relevant result is that the lineshape is:

$$\langle P_3 \rangle(x) = \frac{2\Omega_1^2\Omega_2^2(x^2 + 3(\Omega_1^2 + \Omega_2^2))}{4x^4\Omega_1^2 + x^2(-8\Omega_1^4 + 20\Omega_1^2\Omega_2^2 + \Omega_2^4) + 4(\Omega_1^2 + \Omega_2^2)^3} \quad (2.19)$$

where $x = \Delta_2 - (\delta_3 - \delta_2)$ is the detuning from the resonance in the atomic beam. (Note that resonance is at $\Delta_2 = 0$ if no field is applied, and only $\Delta_2 = \delta_3 - \delta_2$ if there is a field applied— since $\delta_j \propto \mathcal{E}^2$.)

Plots of this lineshape are shown in Figure 2.10 for various choices of the Rabi frequencies. As can be seen, the well-known Autler-Townes splitting can be seen in the regime $\Omega_1 \gtrsim 0.7\Omega_2$. While Ω_1 sets the overall scale at which a splitting might begin to be observed, and Ω_2 sets the overall width of the entire pattern, the ratio of Ω_1/Ω_2 determines whether any Autler-Townes splitting occurs. In other cases, especially when both Rabi frequencies are small, the lineshape is sharply peaked. In the experimental case explored in this thesis, the upper transition's electric dipole matrix element is intrinsically larger than the lower transition by about a factor of 3,

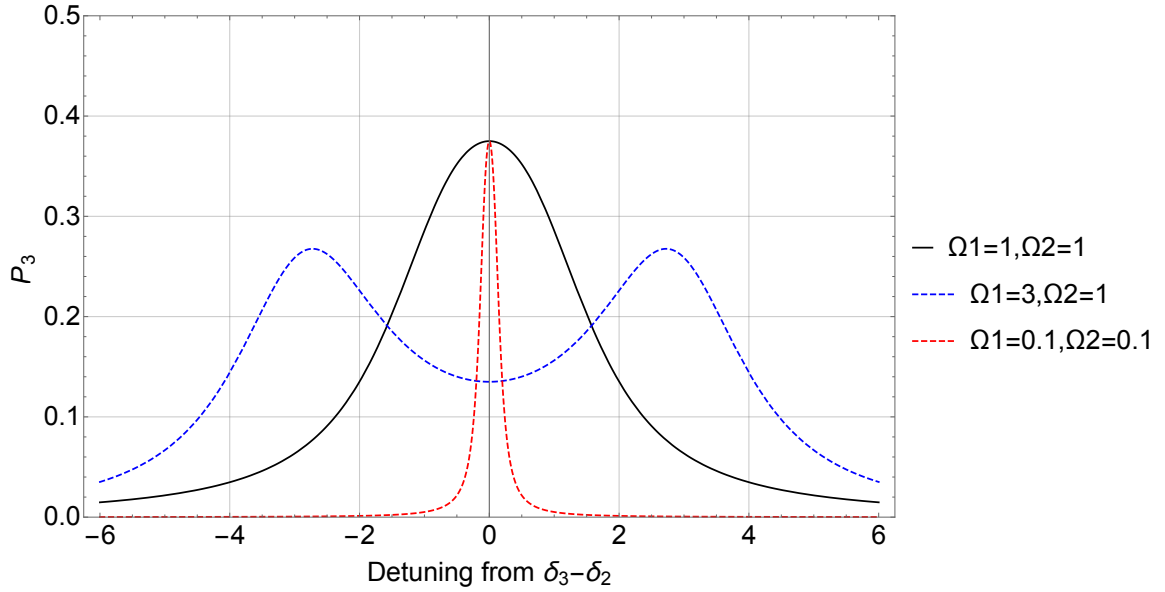


Figure 2.10: Plot of the analytic lineshape for a transition from $|1\rangle$ to $|3\rangle$ for various choices of Rabi frequencies. In our experiment, we are in the regime $\Omega_1 < \Omega_2$ due to the intrinsic coupling between the lower two states.

so given roughly equal laser powers in the atomic beam, we only ever expect to see a single peak.

Furthermore, in the case of a blue laser which remains always resonant with the atomic beam transition, the lineshape is always symmetric about the expected position of the Stark shift in the IR transition alone. That is, even in the presence of broadening, the shift we observe experimentally in this case always corresponds to the difference in Stark shifts between the third and second states. Performing our experiment this way, we therefore expect to measure $\alpha_0(6P_{1/2}) - \alpha_0(6S_{1/2})$.

Chapter 3

Experimental Setup

The apparatus used in this experiment draws on experience the Majumder lab has gained conducting experiments in both vapor cell and atomic beam environments. Detailed discussions of specific elements can therefore be found in [15–17]. Nonetheless, because each piece of the setup is crucial to our ability to measure the Stark shift (and diagnose systematic errors), it is worthwhile to describe them all briefly. In this chapter, we take an operational approach to the purpose of each element, leaving details about construction to the references provided. Special attention is paid to significant additions and changes to the existing apparatus: mainly laser stabilization, electric-field plate separation measurement, and the two-tone FM spectroscopy scheme. A schematic of the system is shown in Figure 3.1. As can be seen, the experiment consists of two (interdependent) regions: one used for laser preparation and diagnostics, the other used to conduct the actual experiment and process the relevant signals.

3.1 Sources of Atoms

In order to conduct an atomic spectroscopy experiment, we first need a source of atoms to probe. Furthermore, to study indium using laser spectroscopy, we must deal with the fact that indium is a solid metal at room temperature. Even at temperatures approaching 1100°C , indium has very small vapor pressure, so high temperatures are necessary to induce measurable absorption. We rely on two separate methods to produce these atomic vapors.

3.1.1 Table-Top Vapor Cell

First, we use a table-top oven to heat a sealed, quartz cell of indium to $\sim 730^{\circ}\text{C}$. This produces an indium atomic vapor of optical depth $\alpha \sim 1$ in our 10 cm long vapor cell, i.e. about 60% of light is absorbed directly on resonance. This is ideal for the purposes of frequency stabilization, as discussed in Section 3.2.2. Along with the relatively large absorption comes a large amount of Doppler broadening, at least

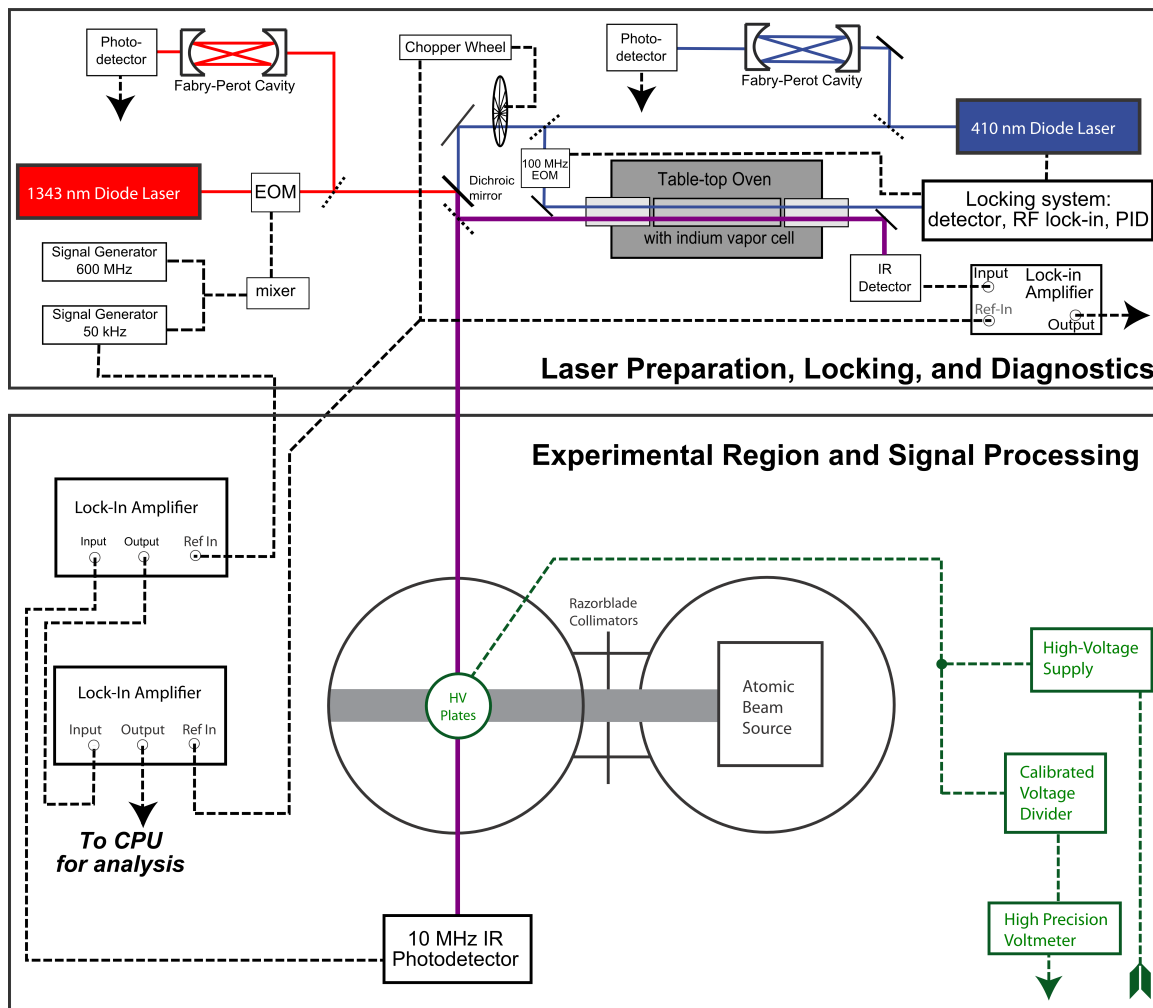


Figure 3.1: A diagram of the full experimental apparatus. For clarity, boundaries have been drawn around the parts of the setup that focus on preparation and calibration, and those that allow for the actual experimental manipulation and data collection.

in the $5P_{1/2} \rightarrow 6S_{1/2}$ transition. Doppler broadening is by far the largest broadening mechanism in the vapor cell, leading to widths of ~ 1.6 GHz in this first-step transition. Furthermore, because the table-top oven sits in air (rather than vacuum), it would be very difficult to measure the Stark shift in this environment. Applying large electric fields across the vapor cell could lead to catastrophic breakdown. Even if we resigned ourselves to applying smaller fields, it would be difficult to calculate the electric fields experienced by the atoms since we would need to take the effect of the dielectric glass cell into account. The atomic beam removes these concerns by allowing us to apply large, easily calculable electric fields *directly* to the atoms. Even so, the vapor cell is an ideal tool for locking the 410 nm laser (see Section 3.2.2) and monitoring the 1343 nm transition as a stable frequency reference (see Section 4.1.1).

3.1.2 Atomic Beam Unit

In order to apply such large electric fields, our group has traditionally conducted Stark shift measurements using an atomic beam unit (ABU). The ABU is housed within a vacuum chamber, allowing for safe application of large electric fields. A diagram of the system is shown in Figure 3.2. Both the ABU and vacuum chamber are described in great detail in [15, 16], so we will present only a brief overview here.

Vacuum System

The vacuum chamber, designed and adapted by many previous thesis students, is necessary due to our desire both to apply a well-calibrated electric field while also heating a sample of indium to over 1100°C . Operationally, a “roughing” vacuum pump is used to achieve pressures $\sim 10^{-3}$ torr. Once we have achieved this level of vacuum, a pair of diffusion pumps (complete with liquid nitrogen traps) further reduce the pressure to between 10^{-6} and 10^{-7} torr, even when the sample of indium is heated to 1100°C . The chamber is equipped with both Pirani and ionization gauges to measure the pressure at various levels of evacuation. While these pressures are nowhere near the state of the art in vacuum technology, the mean free path of an indium atom in our atomic beam is many times larger than the atomic beam’s path. The pressures we achieve are low enough that we may ignore the presence of any other gas in the ABU. More details about the vacuum system may be found in [15].

Atomic Beam Production

The source of indium atoms, also described in detail in [15, 16], consists of a molybdenum crucible heated by a custom-built oven. By heating a sample of roughly 100 grams of indium to 1100°C , we produce an atomic beam with low, but sufficient, optical depth ($\alpha \sim 10^{-3}$). Special care was taken to shield the rest of the ABU from the radiation put out by the oven [16]. As described in [15], the construction of the crucible is such that the emerging atomic beam is initially collimated by 20 small slits at the crucible’s opening. Various other elements collimate the atomic beam

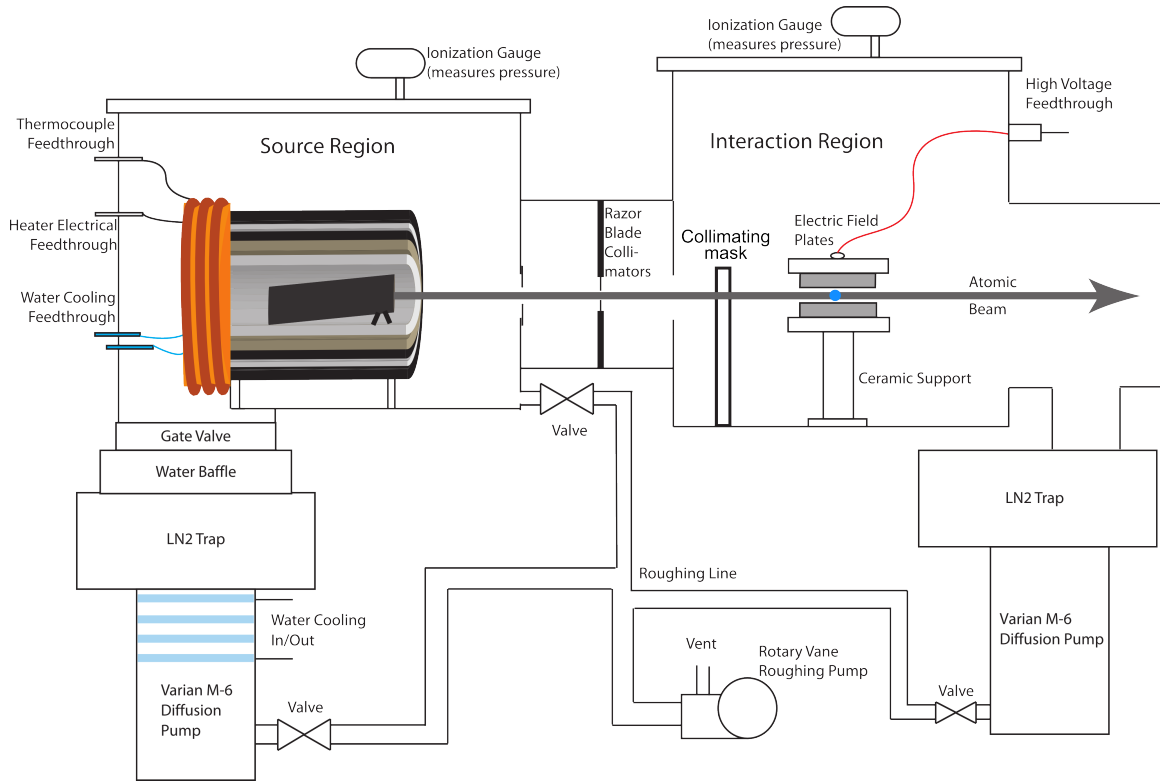


Figure 3.2: A diagram of the atomic beam unit, housed inside our home-built vacuum chamber. The atoms travel from left to right, being collimated into a ribbon-shaped beam before reaching the interaction region.

along its path. A set of four, adjustable razor blades define the atomic beam into a “ribbon” shape about 20 cm before the lasers interact with the atoms. Then, about 5 cm before the interaction region, a rectangular shield is placed in the atomic beam’s path to further collimate the beam, and to reduce the amount of indium that may coat the electric field plates. With all of these efforts, the beam is collimated to such a degree that the residual Doppler broadening in our atomic beam is drastically reduced: we observe $5P_{1/2} \rightarrow 6S_{1/2}$ transition widths of only 100 MHz in the ABU, whereas the same transition is broadened to nearly 2 GHz in a table-top vapor cell at 730°C (see Section 4.1.1). The 100 MHz width, still a factor of 4-5 larger than the natural linewidth of the transition, is primarily due to power broadening (we purposely saturate transitions) and some residual Doppler broadening. This is of significant advantage for single-step excitations, like in [15], as the narrowed signal is essential for observation of the small perturbation observed when the electric field is applied. Collimation is also useful in the present two-step experiment, because in a well-collimated beam interacting with two laser fields, a significant proportion of the atoms will be resonant with the second-step laser, in contrast with the situation in the vapor cell (see Section 4.1.1).

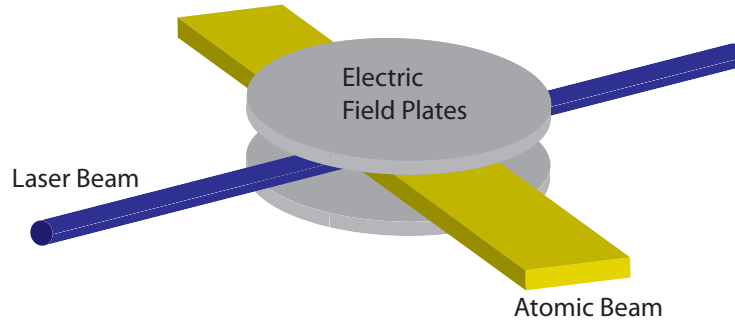


Figure 3.3: Reproduced from [15], this image shows the interaction region’s geometry. The atomic beam, applied electric field, and laser beams are all mutually orthogonal.

Interaction Region

The Stark shift is evident as a shift in atomic absorption lines due to the application of an electric field; in the interaction region, we induce this shift. The collimated atomic beam finally passes through the interaction region, where overlapped 410 nm and 1343 nm laser beams intersect it at normal incidence. A pair of high-voltage (HV) capacitor plates is capable of applying electric fields up to ~ 20 kV/cm to this interaction region. See Figure 3.3 for an image of the interaction geometry.

Previous theses describe the precision with which we can measure the applied electric field [15], which is done using a specially calibrated voltage divider to monitor the voltage applied across the roughly 1 cm-separated plates. These HV plates lead to an approximately constant electric field sufficiently near their center: computer simulations of the field between finite, circular HV plates confirm that the field is essentially uniform (to the level of precision we require in our electric field value) across the width of the atomic beam. Hence, edge effects due to finite HV plate size can be neglected. Defining the direction of the field to be the z -axis, we obtain

$$\vec{E} = \frac{V}{d} \hat{z} \quad (3.1)$$

Our HV plates are separated by $d = 1.0005(5)$ cm, and we can apply voltages up to 20 kV, allowing us to achieve fields of up to 20 kV/cm. A significant change in how we measure the plate separation has allowed us to achieve higher precision in the value of our plate separation, d , than possible in previous experiments. A new CNC machine in the Williams College machine shop allows for precise determination of position differences, to better than 1 part in 10^3 .¹ While previous theses measured the plate

¹As a test of this value, we measured the width of a precisely ground gauge block to within 4 microns of its quoted 2 cm width.

separation with a fractional uncertainty of 10^{-3} [15], using the new measurement method we have achieved an uncertainty of roughly 5×10^{-4} .

Of course, the uncertainty in the *electric field* comes from a combination of voltage uncertainty and plate separation uncertainty. If we let δ represent fractional uncertainty, propagation of errors yields:

$$\delta\mathcal{E} = \sqrt{\delta V^2 + \delta d^2} \quad (3.2)$$

In Equation 3.2, we have $\delta d = 5 \times 10^{-4}$. We know the voltage reading (and the field uniformity) to about an order of magnitude greater precision than this. To be sure that we know V to this precision, we follow [24] to numerically solve Laplace's equation assuming cylindrical symmetry (given our round capacitor plates) and ensure that the field is predicted to be uniform across the width of the atomic beam to at least 1 part in 10^4 . Thus, the fractional uncertainty in the electric field comes almost exclusively from the separation measurement. We include *twice* this value in our systematic error budget, because the Stark shift we observe is proportional to \mathcal{E}^2 . We measure the field plate separation both before and after collecting experimental data to make sure the value has not changed.

3.2 Optical System

To excite transitions in either of these atomic sources, we must also produce laser radiation at the proper frequencies. First, we discuss the lasers used in this experiment, and then discuss the problem of stabilizing the frequency of the blue laser.

3.2.1 External Cavity Diode Lasers

The two lasers necessary for this experiment have been described in other theses [15, 17]. Briefly, they are two external cavity diode lasers (ECDLs): a blue laser tuned to the $5P_{1/2} \rightarrow 6S_{1/2}$ transition near 410 nm (Toptica DL 100), and an IR laser tuned to the $6S_{1/2} \rightarrow 6P_{1/2}$ transition near 1343 nm (Sacher Lynx series). Both are arranged in the so-called Littrow configuration. In this configuration, the diode puts out light over a relatively broad frequency range. The light is collimated by a lens and directed onto a diffraction grating; by directing the first-order diffracted light back into the diode, an external cavity is formed allowing for lasing operation to occur. Importantly, because the grating diffracts light at specific angles dependent upon the light's frequency, this adds a tunable frequency-selective element. Only a precise frequency of light will be amplified and lase. Using the zeroth order diffracted beam as the actual laser output, we obtain up to ~ 8 mW of light from the blue laser and ~ 20 mW of light from the IR laser, each with sub-MHz linewidth over short (< 1 sec) time scales when operating in single-mode (i.e., only one lasing frequency) operation. Over longer time scales (several minutes), a free-running ECDL tends to drift ~ 100 MHz. We address this in Section 3.2.2.

Careful adjustment of the exact grating position, the current run through the laser diode, and the temperature of the diode can be used to adjust the lasing frequency and single-mode reliability. Even a small misalignment results in multi-mode operation, in which many longitudinal modes of the external cavity are simultaneously excited. We can slowly scan the exact wavelength selected in this process by applying a small voltage ramp to a piezoelectric transducer (PZT) attached to the diffraction grating. Typically, the lasers will scan smoothly over ~ 5 GHz while maintaining single-mode operation. A 500 MHz free spectral range (FSR) Fabry Perot cavity is used to monitor single-mode operation of the IR laser, while a 1 GHz FSR cavity is used similarly for the blue laser. We also make use of a commercial wavemeter (Burleigh WA-1500) to measure each laser's frequency to 0.1-ppm accuracy (see [17] for more details on its operation).

3.2.2 Frequency Stabilization of the 410 nm Laser

In order to observe the Stark shift in a two-step transition, it is necessary to stabilize the frequency of the blue laser driving the lower transition. We choose to lock the blue laser to the $5P_{1/2}(F = 5) \rightarrow 6S_{1/2}(F' = 4)$ transition. Locking to this resonance is important to protect against systematic errors. In observing a two-step transition, we must keep in mind that the sum of both laser frequencies contributes to the overall observed shift. Any frequency drifts of the blue laser of the same order as the Stark shifts we expect to observe would propagate into an uncertainty in the measured shift. Because free-running ECDLs typically drift by tens to hundreds of MHz over many minutes, roughly the size of a Stark shift we expect to induce, this sort of drift is not tolerable. Furthermore, by locking the blue laser we are then able to adjust the precise frequency that is sent to interact with the atoms in the ABU (see Section 5.1). To deal with these concerns, significant time and effort was spent achieving a method of laser locking that would stabilize the blue laser to eliminate frequency drifts.

First, a brief explanation of the theory underlying our locking scheme. One can achieve a laser lock by choosing a suitable error signal to pass into a proportional-integral-derivative (PID) controller, a device which outputs a voltage correction proportional to that error signal back to the laser in order to correct for drifts away from the lock point. Since we would like to lock the laser to the center of a particular transition, it is only natural to use the atoms themselves as the source of this error signal. We thus pass a portion of the blue laser through the table-top vapor cell and use the absorption of light to produce our locking signal. One might be tempted to use a direct absorption signal as the error signal by telling the PID controller to maintain the laser frequency at the point of maximum absorption. However, this naive method quickly runs into a problem: it is impossible to distinguish between a drift from ω to $\omega + \epsilon$ and one to $\omega - \epsilon$ using only the absorption signal, since the Doppler-broadened line is symmetric about its center. Hence, we desire a signal that looks like the *derivative* of an absorption curve in order to lock our laser. In such a case, the signal's linear portion gives useful feedback to the PID controller. For

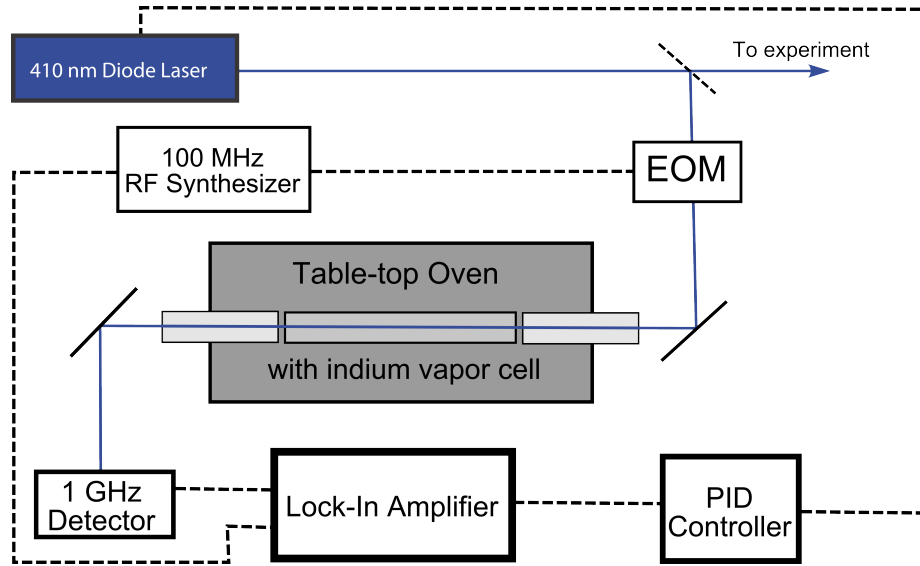


Figure 3.4: The new locking scheme developed for this experiment. The blue laser is directed through a 100 MHz EOM, passed through the table-top vapor cell, and the transmitted light is demodulated at the EOM’s drive frequency using an RF lock-in. The resulting dispersion lineshape is used as the error signal for PID feedback.

instance, if the laser’s frequency drifts high, the voltage will go negative and if the frequency drifts too low, the voltage will go positive. Now the two potential drift directions can be distinguished, and feedback to the laser can be set always to return the laser to the line center.

In fact, the Majumder lab has developed its own locking method that has been used effectively in many past experiments. This method is detailed in [25]. It relies on the differential absorption of laser beams that have been shifted in frequency relative to one another. Unfortunately, the reliance on *two* laser beams leads to concerns about whether each beam carries equal power. Variations as small as a few percent between the two beams (typical, based on our observations) would cause unwanted locking offsets of tens of MHz. This is dangerous to our measurement, as a drift of the blue laser’s frequency of this size would lead to exactly the sorts of issues we proposed to eliminate by locking the laser in the first place. Hence, we abandoned this locking method and searched for a scheme that relied on a single laser beam. Such a method would, presumably, be free from the potential problems caused by power variations in a differential absorption measurement.

New Locking Scheme

Our new method is outlined schematically in Figure 3.4. At its core it is a single-tone FM spectroscopy experiment conducted in the table-top vapor cell, like that performed in [16]. From an experimental perspective, the lock works as follows: A small portion of the blue laser (< 1 mW) is picked off near the laser. While we

scan the laser frequency, ω_c , across about 2 GHz centered on the 410 nm transition, the beam is directed through the table-top vapor cell and transmitted with some frequency-dependent transmission factor, $T(\omega_c)$. As discussed above, this is not a useful locking signal, but its derivative *would* be an ideal locking feedback signal. To obtain the derivative signal, we direct the picked-off portion of the blue laser beam through an electro-optic modulator (EOM; New Focus model 4005) *before* it enters the vapor cell. The EOM consists of a crystal inside a resonant cavity which modifies the phase of a laser beam passing through it, essentially dithering the laser's frequency by a small amount about the unmodulated frequency (see Section A.3.1). The beam then interacts with an atomic sample in the vapor cell, is detected using a high-speed photodetector capable of resolving oscillations at 100 MHz (New Focus model 1601; 1 GHz bandwidth), and is finally demodulated using an RF lock-in amplifier (Stanford Research Systems SR844).

Two important factors in determining the quality of a locking signal are its steepness and its signal-to-noise ratio. Since the locking signal obtained from the above method is relatively broad, it is a robust but not particularly tight lock.² Nonetheless, it has extremely high signal-to-noise. Its several-GHz-wide linear portion gives a suitable locking signal for PID feedback. In typical use, the slope of the locking signal's linear portion is approximately 100 MHz/V, giving us good tunability over a broad range of frequencies centered on the 410 nm transition.

Figure 3.5 shows a typical locking signal along with a simultaneously recorded Fabry-Perot transmission signal. We know the Fabry-Perot cavity has a FSR of 1 GHz. Hence, we can calibrate the slope of the locking signal as follows: measure the slope of the linear portion of the error signal (in units of V/msec) as well as the separation between consecutive Fabry-Perot peaks (which gives a measure of msec/GHz). Taking the ratio of these two numbers immediately allows us to determine the slope of the locking signal, in units of MHz/V. In the example shown here, that slope is about 150 MHz/V. After locking the laser by sending feedback to the PZT voltage by means of the PID controller, we stabilize the laser around the center of the error signal's linear portion.

In actuality, the PID controller's output is more sophisticated than simply a voltage proportional to the error signal. There are three separate terms in its output: a proportional gain, an integral gain, and a derivative gain. By adjusting the P, I, and D terms separately, we can optimize the locking feedback to give a robust, tight lock. With proper tuning, we can stabilize the blue laser to completely eliminate long-term drifts. Furthermore, the stabilized frequency exhibits noise of RMS fluctuations < 1 MHz. The lock is robust enough that it eliminates long-term drifts without any trouble for up to many hours, much longer than the typical data collection routine lasts. Any residual noise (as opposed to drift) is rapidly averaged away in the data collection process. Over long time scales, we are primarily limited by thermal drifts

²In fact, despite the scheme being quite different than those used in previous experiments in the Majumder lab, the residual noise is quite comparable to past locking schemes.

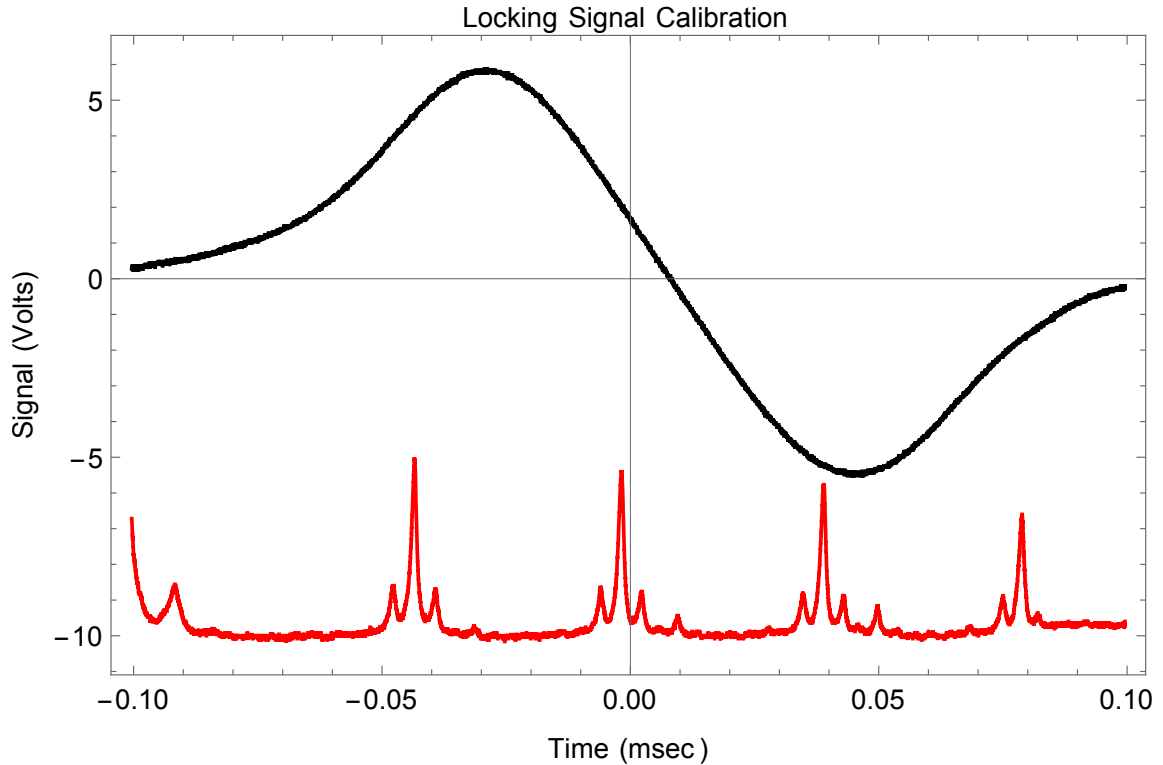


Figure 3.5: Error signal used for locking above a Fabry-Perot transmission signal, recorded simultaneously. The error signal is obtained by demodulating a single-tone FM signal (hence the sidebands on the Fabry-Perot). Given the Fabry-Perot trace’s known FSR, we can determine the slope of the locking signal and calibrate the residual noise.

which tend to change the laser frequency. Placing the laser within an insulated box eliminates some of of this drift.

Any laser drifts are seen as motion along the locking signal. Hence, the locking signal’s slope gives the conversion between observed voltage drift along the locking signal and the frequency drift that led to such a change in voltage. The locked and unlocked behaviors are dramatically different, as can be seen in Figure 3.6. Once locked, the long-term drift is completely eliminated and all that remains are small fluctuations in the laser frequency of RMS size ~ 1 MHz.

Detuning from Lock-Point

As was discussed in Section 2.4.3, if we wish to measure $\Delta_{32} = \delta_3 - \delta_2$, then we must keep the blue laser on resonance with the atomic beam transition at all times, including when the HV is on and induces a Stark shift. One way to achieve this would be to use the known slope of the locking signal to adjust the blue laser’s lockpoint so as to compensate for whatever Stark shift is induced when the HV is on. This is not ideal for a few reasons. First, the slope is not known precisely enough for us to trust the adjusted lockpoint to compensate exactly for the Stark shift in the

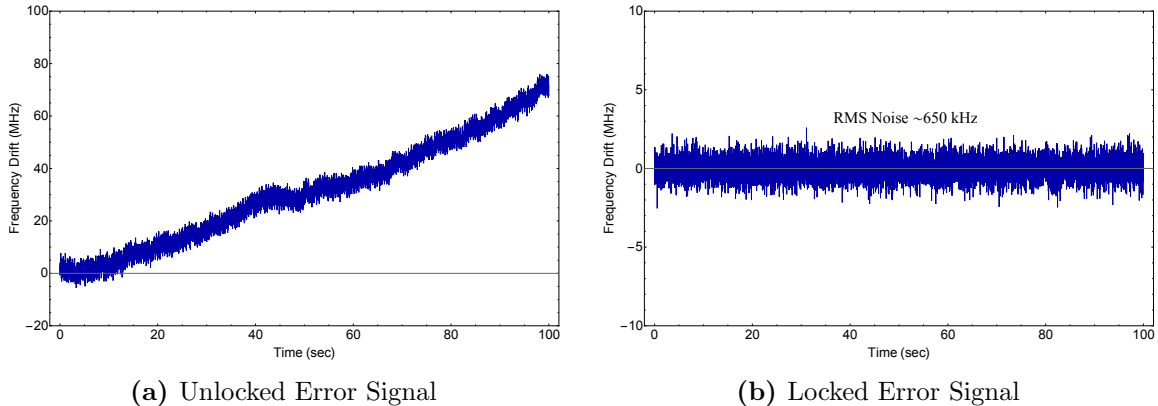


Figure 3.6: Frequency drift of the laser (a) when it is unlocked and (b) when it is locked. Note the order of magnitude difference between the two vertical axes. Our locking scheme completely eliminates background drifts, leaving only small fluctuations of RMS value < 1 MHz.

lower transition. Furthermore, we wish to use the vapor cell as a frequency reference by measuring all frequencies relative to the hyperfine structure observed in the IR laser transition (see Section 4.1.1). Adjusting the lockpoint to stay resonant with the atomic beam would force us to be *off* resonance with the vapor cell, and therefore cause a Doppler shift in our frequency reference—making it a poor reference indeed.

We have therefore begun work on a frequency adjustment method which shifts *only* the portion of the blue laser beam that enters the atomic beam. This is described in more detail in Section 5.1.

3.2.3 IR Laser Preparation and Modulation

With the blue laser’s frequency stabilized, we continue working within the table-top vapor cell in order to observe the second-step (IR) transition. We first use the wavemeter to ensure the IR laser is operating near the desired frequency, and then check that it is lasing single-mode by means of a Fabry-Perot cavity. Applying a linear voltage ramp to the laser’s PZT allows for smooth (though not-quite-linear) frequency scanning. As is developed in Section 3.3, this Fabry-Perot signal (FSR = 500 MHz) is crucial to our frequency linearization scheme. We routinely achieve smooth, single-mode scanning over ~ 4 -5 GHz.

Only about 4% of the light is sent through the Fabry-Perot cavity. The remainder is directed through an EOM (New Focus model 4423) of resonant frequency 600 MHz. It is useful to think of the EOM’s operation as manipulating the laser’s output in the frequency domain: the EOM adds frequency sidebands to a laser spectrum, separated from the carrier frequency at precisely the frequencies by which it is driven (and perhaps out of phase with the carrier by 180 degrees). In analogy with the operation of the 100 MHz EOM used in the frequency stabilization scheme, one might expect that we modulate the IR beam at 600 MHz, allow it to interact with atoms, and

then demodulate it at 600 MHz. But, due to lack of detectors and lock-in amplifiers at this high frequency, we do not do so. Rather, we drive this EOM at *two* nearby frequencies, both close enough to the nominal resonance frequency of the EOM to obtain reasonable modulation depths. The details of the frequency mixing process we use are outlined in [17]. After mixing the low and high frequencies, we drive the EOM at $\omega_m \pm \frac{\Omega}{2}$, where we choose $\omega_m = 600$ MHz and $\Omega = 100$ kHz. This allows us two different methods for observing the light transmitted through an atomic sample:

1. Measure the light transmitted through an atomic sample *without* demodulating according to an FM spectroscopy scheme. The EOM adds frequency sidebands to the laser spectrum, so around every “real” absorption peak we expect to see small sidebands offset by $\pm\omega_m$.³ Each sideband is separated by precisely ω_m from its carrier peak, so we can use this signal for frequency calibration purposes (the signal is “self-calibrating”).
2. Measure the light transmitted through an atomic sample by demodulating the transmission signal at Ω , the difference between the two frequencies driving the EOM. *This is two-tone FM spectroscopy.* We expect to see the usual two-tone FM demodulated lineshape, like in Figure 2.3. Once again, the signal is “self-calibrating,” even though the sidebands are inverted relative to the main peak. All the advantages of FM spectroscopy are realized, although this mode of detection is more sensitive to perfect beam overlap.

After the EOM, the IR beam is split once again. About 10% of it is directed into the table-top vapor cell, where it is overlapped with the blue beam in order to observe the IR transition as a reference signal. The remaining beam is also overlapped with a portion of the blue laser, but this pair is sent through the ABU to interact with the atomic beam between the electric field plates. At the output of each atomic sample, the IR beam is detected using a New Focus model 2053-FS, 10 MHz photodetector. The detector’s response to the 410 nm wavelength essentially zero, so only the IR beam is detected.

3.3 Data Acquisition

To obtain sufficiently small statistical uncertainty, we must collect many spectra. It is therefore necessary to automate the data collection process. Data is read into the computer using a National Instruments USB-6221 BNC analog DAQ input board. We record the necessary spectra, as well as information about the HV setting, atomic beam temperature, and laser powers. The same board can also be used to the HV settings, and automatically program synthesizers as necessary.

Each full data set is collected as outlined schematically in Figure 3.7. A LabView program, similar to that used in previous Stark shift measurements, is used to control

³Technically, there are peaks at $\pm\omega_m \pm \frac{\Omega}{2}$, but the 100 kHz splitting is so much smaller than the natural linewidth of any transition that we cannot resolve the constituents of each sideband.

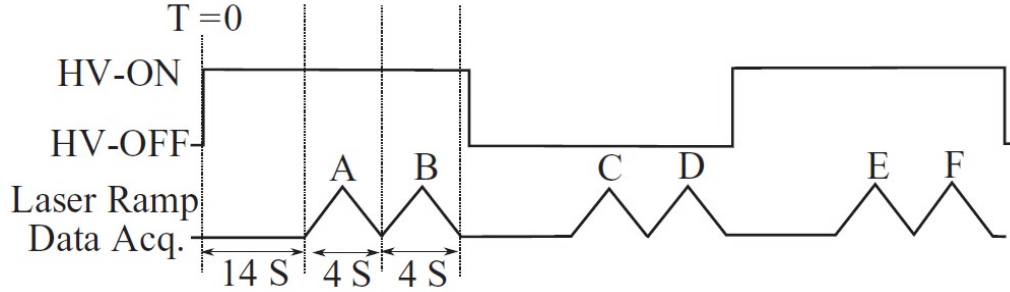


Figure 3.7: Outline of the data acquisition procedure. Figure reproduced from [15].

the full apparatus during data collection. Suppose we have just begun an experimental run, which typically consists of ~ 10 HV values. For the first HV value, the LabView program will switch the HV on; wait ~ 10 -14 seconds for transients to die down; record both an upscan and a downscan; turn the HV off, waiting for transients to settle down; record both an upscan and a downscan; immediately record another upscan and downscan; turn the HV on, wait for transients to die down, and so on. The HV on-off-off-on pattern has two distinct advantages: first, it allows us to switch the HV value half as often, and second, it allows us to search for possible systematic errors by binning all measured Stark shift values according to HV on-HV off and HV off-HV on configurations. The two directions should give rise to the same measurable effect, and any discrepancy warrants further investigation into the systematic error giving rise to it. The data collection procedure is largely unchanged since the last Stark shift measurement performed in the Majumder lab; see [15] for more details.

After recording a predetermined number of HV on-off pairs, the LabView program will repeat the entire process for another HV value. We randomize the order at which HV values are applied, in order to avoid systematic effects that might arise from monotonically increasing or decreasing the voltage. We save all data sets corresponding to a given HV-on value in their own folder, separating upscans and downscans into separate subfolders. Within these separated subfolders, each data set is labeled according to whether it was the HV-on or the HV-off scan for that particular run. More details on this scheme can be found in Appendix D.

Chapter 4

Data Collection and Analysis

In this chapter, we describe the data collection and analysis process by which Stark shift information is obtained from the raw spectra. First, we discuss the important process of actually observing a two-step transition in the atomic beam. This is a fundamentally new result in the Majumder lab. After that discussion, we discuss how data was collected and analyzed. This will be presented in the same logical order followed by the analysis software, which consists mainly of MATLAB code adapted from previous experiments in the Majumder lab. In broad terms, the analysis procedure requires three main steps: (1) linearization of each spectrum's frequency axis, (2) calibration of the frequency scale and selection of a stable frequency reference, and (3) determination of the Stark shift. However, we defer discussion of the inner workings of this code to Appendix D. Here, we present the spirit of the code.

4.1 Observation of $6S_{1/2} \rightarrow 6P_{1/2}$ Transition

Careful overlap of the blue and IR lasers through an atomic sample effectively couples the three states of interest in this thesis, allowing us to excite atoms to the two hyperfine levels contained within the $6P_{1/2}$ state. We observe the transition to this state in both the vapor cell and atomic beam environments. There are essentially two ways for us to detect this transition, and we use both of them.

4.1.1 Vapor Cell Work

Within the vapor cell, this process parallels works reported in [17], so we will present here only a short collection of the relevant results. See Figure 4.1 for a schematic showing the setup used here. With the (locked) blue and (scanning) IR beams overlapped in the vapor cell, we excite atoms into the $6P_{1/2}$ state. Unfortunately, even in the vapor cell the IR absorption is quite low, and we can not resolve the expected dip in transmission as we scan the laser over this resonance. While it is true that the optical depth of the blue transition in the vapor cell is not small ($\alpha \approx 1$), the optical depth for the IR transition in the vapor cell *is* small. Once we lock the blue

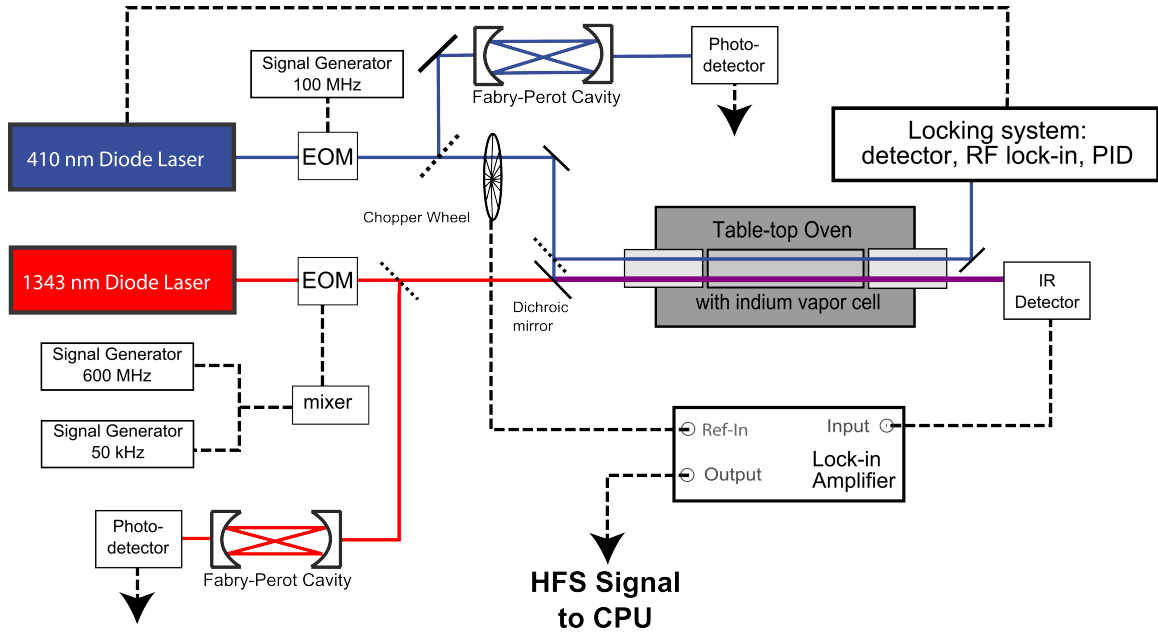


Figure 4.1: Setup used to observe the hyperfine structure within the table-top vapor cell. Both blue and IR lasers are sent into the vapor cell. The blue laser is locked, and then the IR beam (overlapped with blue in the cell) is detected. By modulating the blue laser beam using a chopping wheel, a lock-in amplifier allows easy observation of absorption of the IR laser. Sidebands are evident in the absorption pattern due to the EOM placed after the IR laser’s output.

laser, only those atoms within a homogeneous linewidth of the laser frequency will be excited to the intermediate state, where they are available for interaction with the IR laser. In our case, this natural linewidth corresponds to about 20 MHz. On the other hand, the full Doppler-broadened spectrum spans almost 2 GHz, meaning about 1% of the atoms will be so excited. We compensate for this by placing a chopping wheel in the blue beam’s path and periodically blocking this beam. Removing the blue beam prevents atoms from populating the $6S_{1/2}$ state, and therefore removes the possibility of IR absorption. Qualitatively, the absorption dips “turn on and off” as the blue beam is unblocked and blocked. By using a lock-in amplifier (Stanford Research Systems SR810) to detect only the portion of the signal that oscillates at this chopping frequency, we pick out absorption lines as the IR laser scans over the resonances. Aside from the lock-in detection, this is the experimental realization of “measurement method 1” from Section 3.2.3.

The output of this lock-in amplifier is shown in Figure 4.2. Each transition looks like three absorption peaks because of the sidebands we have added to our laser via the EOM. Because there are two hyperfine states ($F'' = 4$ and 5) to which we can drive transitions, we see *two* sets of three peaks. The central peaks overlap because of an unfortunate coincidence. The hyperfine splitting is nearly 1256 MHz (see Section 4.2.4), whereas we modulate our EOM at near 600 MHz. This leaves

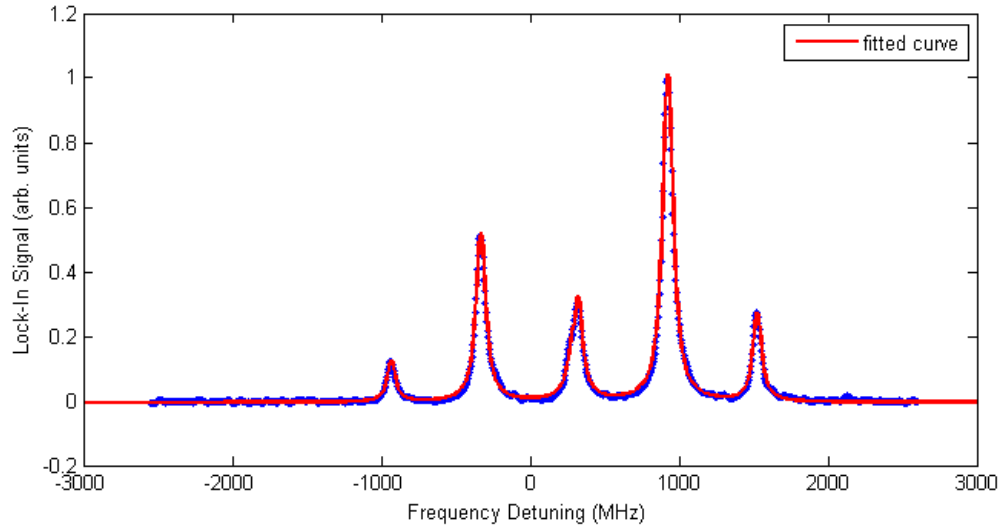


Figure 4.2: Observation of the $6S_{1/2} \rightarrow 6P_{1/2}$ transition within the vapor cell, measured using lock-in detection, with the blue beam chopper wheel as the reference frequency. The fitted curve represents a fit to a sum of six Lorentzians (two hyperfine states + 4 EOM-added sidebands), with frequency calibration based on the sideband splittings. Amplitudes, locations, and widths of all six peaks are left as fit parameters.

only about 50 MHz of space between these two central features.¹ Another important and useful feature can be seen in this vapor cell signal: that we can resolve all six peaks implies we have nearly eliminated Doppler broadening. This is due to an effect known as “hole burning:” with the blue laser locked to the first-step transition, it will excite only a single velocity class of atoms. Therefore, when the IR laser interacts with these atoms, they are already velocity selected therefore suffer little Doppler broadening.

We can reliably observe the IR transition in our vapor cell with high signal-to-noise ratio. Because the sidebands are separated from their corresponding central peaks by precisely 600 MHz, this signal represents an ideal source of frequency calibration (see Section 4.2.4). Furthermore, because there is no better source of frequency reference than the atoms themselves, we can also use the hyperfine signal as a stable frequency reference to define the “zero” of frequency with respect to which we measure a Stark shift.

4.1.2 Atomic Beam Work

The remaining portions of each laser beam (each containing several mW of power) are carefully overlapped through a dichroic mirror and sent through the ABU. See

¹Perhaps 600 MHz is a poor choice of modulation frequency. But because that is the resonant frequency of the EOM we already own, we choose to use it. Our fitting procedure can still resolve all six peaks, making this a nonissue.

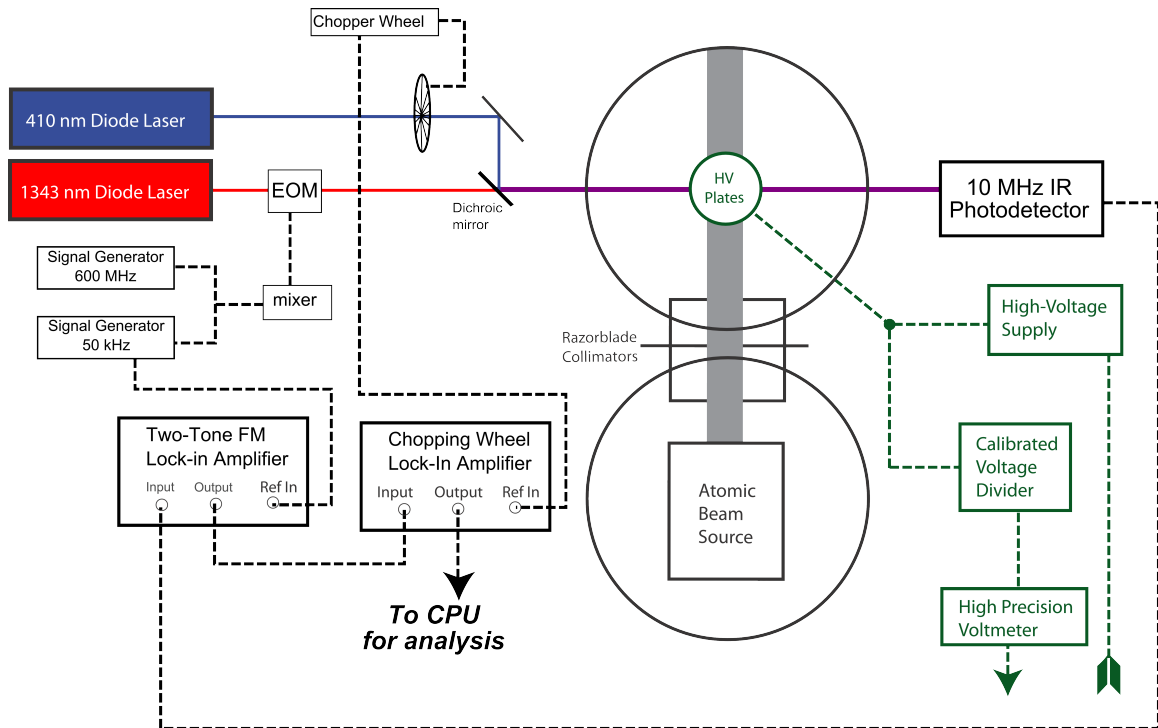


Figure 4.3: A diagram of the optical setup for the atomic beam portion of the experiment only (locking, etc. not shown). The blue and IR laser beams are overlapped, the IR is detected, demodulated using a two-tone FM scheme, and then passed into another lock-in amplifier to demodulate at the optical chopping wheel frequency. Also shown is the HV circuit to provide the electric field.

Figure 4.3 for a schematic diagram showing this portion of the experimental setup. The laser beams intersect the atomic beam transversely, minimizing the effects of Doppler broadening. Much attention must be paid to the beam overlap at this stage. Just as we reasoned about the proportion of atoms that will be excited in the vapor cell, we expect only those atoms that are within the homogeneous linewidth of the atomic beam's inhomogeneous width to be excited. While the atomic lifetime is unchanged in the atomic beam, the Doppler broadening is reduced to about 100 MHz. Hence, between 20% and 30% of atoms will be available for interaction with the IR laser beam, as compared to only 2% in the vapor cell. This somewhat compensates for the drastically reduced atomic vapor density.

With special care, and extreme patience, this alignment procedure allows us to observe an easily identifiable two-tone FM signal. It is useful to place irises near the input and output of the ABU once a signal is detected in order to aid future alignment procedures. Marking the beam path in this way helps achieve overlap and reduce aggravation. Once any semblance of a two-tone FM signal is observed on an oscilloscope, minute adjustments to the 410 nm laser's path have dramatic effects on signal size and symmetry. We believe this is because changing the overlap of the blue and IR beams changes the effective coupling of the three levels seen in the atomic

beam. Hence, making the lineshape look symmetric is the best way to ensure that we achieve the overlap assumed in the theoretical treatment of this problem. It is much better to adjust the blue beam while leaving the IR path fixed, as the actual detected signal comes from the IR light.

The overlapped IR and blue laser beams are transmitted through the atomic beam, and after exiting the vacuum chamber the IR laser is detected using the 10 MHz New Focus photodetector. The detected signal is passed immediately into a lock-in amplifier referenced to twice the low-frequency of the mixed signal driving the IR EOM ($\Omega = 100$ kHz). In principle, the output of the lock-in would give the two-tone FM demodulated signal, however the output is typically dominated by a noisy background (perhaps due to etaloning between the surfaces of the EOM). To compensate, we pass the first lock-in's output into a second lock-in, referenced to the same chopper wheel which intersects the blue beam's path in the vapor cell monitoring.² Because periodically blocking and unblocking the blue beam modulates whether the IR absorption is seen at all, *this* lock-in's output is truly background-free, and allows us to see a clean two-tone demodulated lineshape. A representative demodulated signal is shown in Figure 4.4. While the noise is clearly larger than the noise in vapor cell signals like Figure 4.2, the signal-to-noise is sufficient to allow a precise Stark shift measurement with modest integration time. This signal is particularly exciting because it represents the first time the Majumder lab has observed a two-step excitation in the ABU, in any atomic species. The ability to do so opens the door not just to completion of the present experiment, but to many future studies of excited state polarizabilities.

Observation of the Stark Shift

The most important experimental advance realized in this thesis was observing the Stark shift. After inserting the electric field plates, we hooked up the same high-voltage circuit that was used in [15]. We can safely apply voltages of up to ~ 15 kV, generating fields of ~ 15 kV/cm. When we do so, the large $6P_{1/2}$ polarizability means we observe noticeable Stark shifts of order 100 MHz. See, for instance, Figure 4.5, which shows the HV-off and HV-on two-tone FM signals when the high voltage is tuned to 10 kV. There is a clear shift between the two signals, of the expected size (as will be quantified in Section 4.2.5).

4.2 Data Analysis

After observing the two-step FM spectrum in the ABU, we move on to automate data collection and analysis. As mentioned above, the gory details of this process are reserved for Appendix D, but it is necessary to give an overview of what is achieved in this process. Two steps are required for every data set: linearizing the frequency axis

²The careful reader will notice that this brings the total number of lock-in amplifiers used in this experiment to four. We believe this sets a record for the number of lock-in amplifiers used by the Majumder lab in any single experiment (an obscure, though humbling, honor).

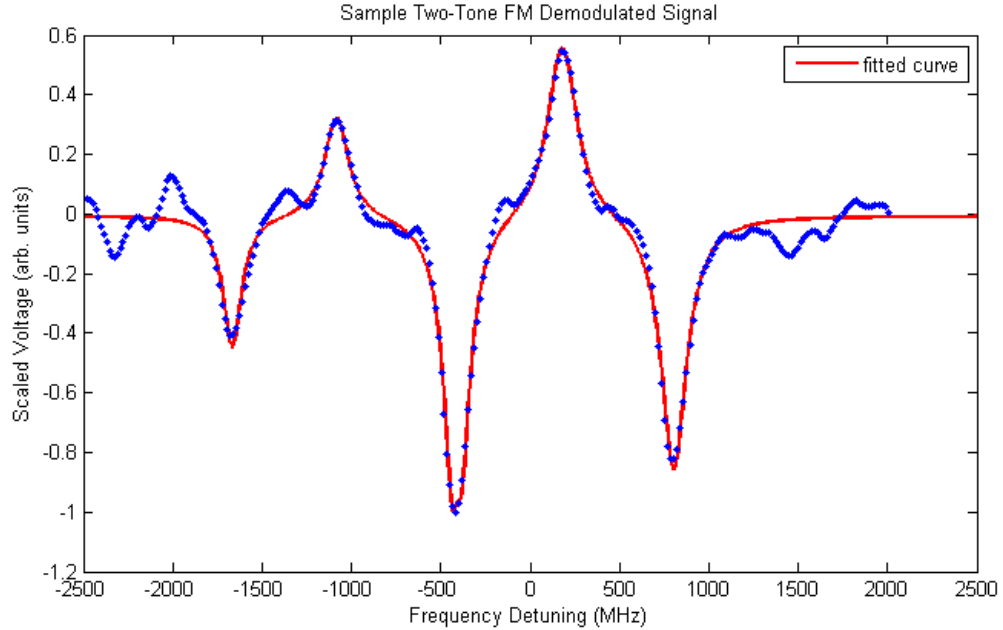


Figure 4.4: An example of the two-tone FM demodulated lineshape observed in the atomic beam. This represents the first time the Majumder lab has realized an observation of a two-step excitation in the atomic beam apparatus. Experimental data (blue dots) is shown along with a fit to the expected lineshape (i.e., a sum of six Lorentzians; red line).

and calibrating that axis. The final step, extraction of a Stark shift, can only be done by comparing data sets as HV-on and HV-off pairs. This analysis is representative of the sort conducted in most Majumder lab experiments, so the interested reader will find more details in [13, 15].

4.2.1 Collected Signals

Each time we collect a single two-tone FM spectrum (i.e., each individual trial), we simultaneously sample four signals. Aside from the voltage ramp, these signals are the ones shown in Figure 4.6. They are:

1. *The voltage input to the IR laser PZT*, which allows us to sort data sets into “upscans” and “downscans” according to the direction the laser frequency is swept across the $6S_{1/2} \rightarrow 6P_{1/2}$ transition.
2. *The IR Fabry-Perot transmission signal*, which provides a frequency linearization for the horizontal axis of all our collected data.
3. *The IR absorption pattern in the $6P_{1/2}$ state, observed in the table-top vapor cell*. This allows us to redefine the “zero frequency” to a specific peak in the absorption pattern for *every* trial. Since we are measuring a *shift*, it is important to have a drift-free reference frequency.

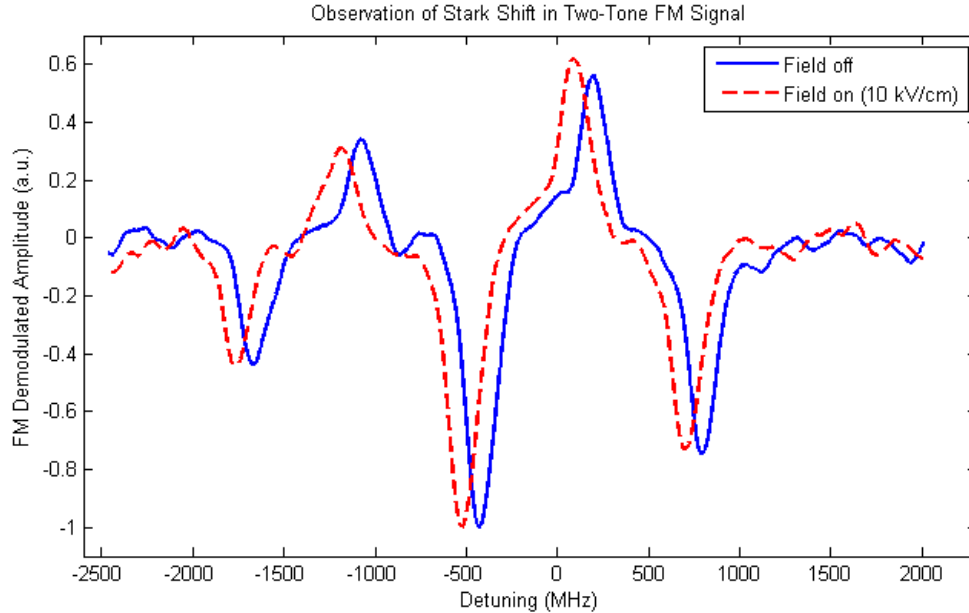


Figure 4.5: HV-on (solid/ blue) and HV-off (dashed/ red) two-tone FM signals for a field value of 10 kV. The shift is clearly noticeable, and ends up being about 100 MHz for this particular measurement.

4. *The atomic beam two-tone FM demodulated signal*, as described in Section 4.1.2. This is the signal used to measure the Stark shift.

4.2.2 Data Import

When each data set is imported into the analysis program, each signal consists of some horizontal axis given by the raw point number ranging from 1 to N . We first construct a normalized horizontal axis for each signal. We define a “normalized point number” over which to plot the raw signals. The j^{th} point defined by the relation

$$x_j = \frac{j - N/2}{N/2} \quad (4.1)$$

where N is the total number of points. Clearly, x_j ranges from -1 to 1 . This is important because later we will fit the frequency axis to various polynomials, and limiting the unscaled axis to $|x| < 1$ means that we can meaningfully compare the coefficients of each order of that polynomial.

The other important pre-processing step taken is to import downscans in order of *decreasing* point number. This ensures that, when plotted versus a frequency axis, all data sets increase in frequency in the same direction (i.e., from left to right). For instance, this will always place the $F = 4$ hyperfine peak in the $6P_{1/2}$ state to the left of the $F = 5$ peak. We can then analyze the data uniformly without

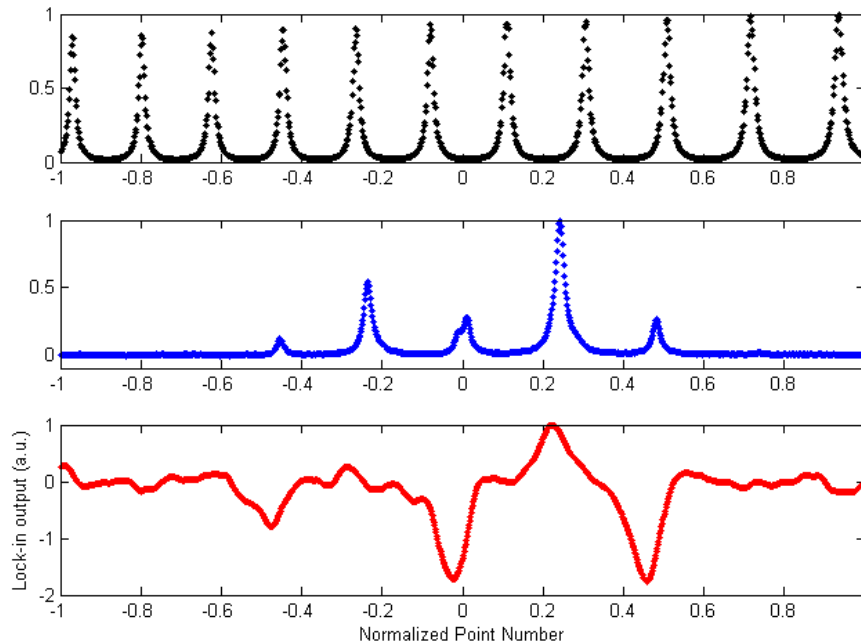


Figure 4.6: One example of the three signals collected on every experimental run. From top to bottom they are: a Fabry-Perot trace over the IR laser’s frequency scan, the table-top vapor cell IR transition (with EOM-induced sidebands), the atomic beam two-tone FM demodulated signal. Note that the horizontal axis for each scan is “normalized point number,” defined in Chapter 4, and the vertical axis is an arbitrary voltage scale (with a convenient normalization chosen).

having separate code for upscans and downscans. Nonetheless, we keep upscans and downscans separated from one another in order to search for systematic errors later.

4.2.3 Frequency Linearization

It is well known that the PZTs which we use to scan the IR laser frequency have a nonlinear response to an applied voltage ramp. Even with a perfectly linear driving voltage, the laser frequency is characteristically hysteretic. This is most easily seen by observing a Fabry-Perot transmission signal collected over the course of a laser sweep: though the peaks are theoretically spaced by exactly the FSR of the cavity, when we actually record a Fabry-Perot signal, we see unevenly spaced peaks. Really, this is just a problem of inertia—the PZT pushes on the ECDL’s grating, and inertia causes the push to be less effective early in the sweep. In the case of an upscan, the peak spacing decreases as the laser frequency increases.³ Luckily, this effect is easily

³As noted above, all data is imported into the computer so that in increasing frequency order, so a downscan, which starts at higher frequencies, shows the inertial effect as a decreasing peak spacing with *decreasing* frequency.

mitigated using the known transmission function and FSR of the Fabry-Perot cavity. The transmission of a Fabry-Perot cavity follows a so-called Airy function:

$$T_e = \frac{1}{1 + F \sin^2(\delta/2)} \quad (4.2)$$

where F is the coefficient of finesse and δ is the phase accumulated between successive transmitted peaks. We know the recorded Fabry-Perot signal must follow this functional form, so we can extract a linearized horizontal axis by assuming a polynomial form for δ and performing a fit along the normalized point number axis. With the correct function in the argument of the sine, the horizontal axis will be linear and the Airy function will properly describe the transmission signal. We typically fit to either a third or fourth order polynomial, $f(x_j) = a_0 + a_1x_j + a_2x_j^2 + a_3x_j^3 + a_4x_j^4$. It is also necessary to allow for a variation in laser power, which we typically do by allowing the amplitude to vary linearly as $b_0 + b_1x_j$. (We have found that only linear amplitude variations are significant to the fitting procedure.) That is, we fit the collected data to a function of the form:

$$T_e = \frac{b_0 + b_1x_j}{1 + F \sin^2(a_0 + a_1x_j + a_2x_j^2 + a_3x_j^3 + a_4x_j^4)} \quad (4.3)$$

The function f relates the normalized point number to the frequency of the laser (relative to some zero). It maps a non-linearized axis onto a linearized one. The numerator simply allows for a linear power variation over the scan; a nonlinear fit like this requires *very* good initial guesses or else the fit will inevitably fail. See Figure 4.7 for an example of fitting Equation 4.3 to the raw Fabry-Perot data. Plotting the Fabry-Perot signal versus $f(x_j)$ will yield truly evenly spaced peaks, indicating that $f(x_j)$ is the properly linearized frequency axis, scaled into MHz units.

In Figure 4.8 we see an example of the nonlinearity in the Fabry-Perot scan by plotting $f(x_j)$ versus normalized point number. By looking at the second and higher order terms in that polynomial, it is clear that we need to take some steps to linearize the frequency axis—ideally, those higher order terms would all have been identically zero to begin with.

We have also fit the Fabry-Perot signal to a sum of Lorentzians, and fit a polynomial to the locations of the peaks of these Lorentzians. This also yields a polynomial function which can be applied to the horizontal axis to linearize the frequency; see [13, 15]. Over the course of this thesis, we have tested both methods and seen little to no variation between their results.

Regardless of the method, after linearization both upscans and downscans can be plotted versus the linearized frequency axis $f(x_j)$, and the Fabry-Perot peaks are evenly spaced along that axis. At this point there are still two problems with the (now linearized) frequency axis. First, its zero is arbitrarily located, determined by the polynomial fit parameter a_0 . Second, its overall scale comes from the assumed FSR used in the polynomial fitting procedure. We fix both of these issues next, as discussed in Section 4.2.4.

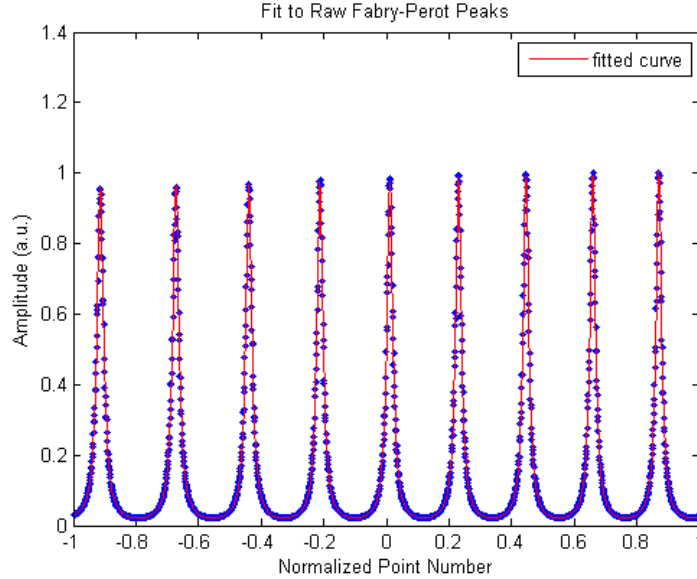


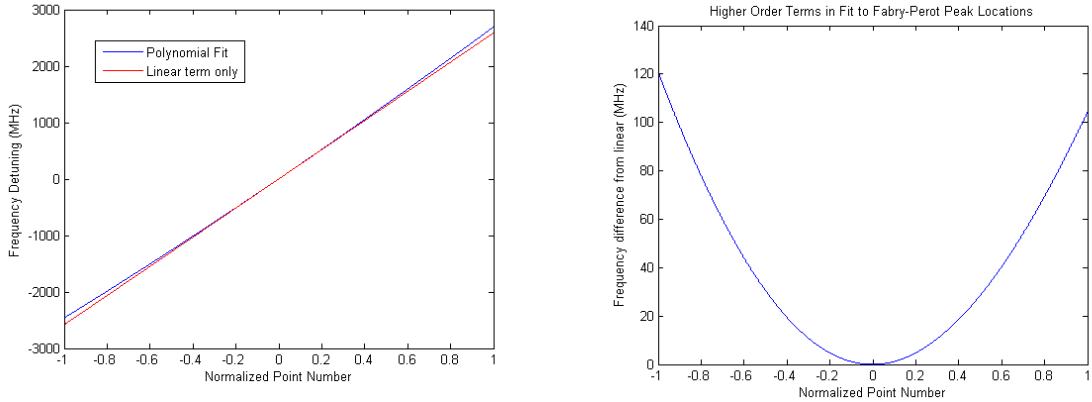
Figure 4.7: Fitting an Airy function to the raw Fabry-Perot data, for the case of an upscan. Note that the peak spacing decreases with increasing point number, as expected for an upscan. This fit yields a polynomial which linearizes the frequency axis to equalize the peak spacing.

4.2.4 Frequency Calibration

We now have a linearized frequency axis, but we cannot yet be sure whether the spacing between points is the *correct* spacing. This is because when we fit the polynomial described above, we assume a Fabry-Perot FSR of 500 MHz, despite knowing that the true FSR differs by a small amount from this nominal value. Fortunately, we can use the vapor cell signal to scale the frequency axis in order to make it the proper size. As described in Section 4.1.1, this vapor cell signal shows the two hyperfine states populated by the IR laser, as well as four sidebands due to the frequency modulation. These sidebands are known to be *precisely* 600 MHz from their respective absorption features, a spacing set by the known frequency output of the synthesizer driving the EOM.

The next step of the analysis, therefore, involves fitting the hyperfine peaks to a sum of six Lorentzians and determining the measured splitting between sidebands and actual absorption peaks. A representative fit was shown in Figure 4.2. First, we choose the largest absorption peak (corresponding to the $6P_{1/2}(F=5)$ state) as our new zero frequency by redefining a_0 in the polynomial $f(x_j)$. This shifts the axis such that all points are measured as a difference (in MHz) from this peak's location.

We also use the fit to six Lorentzians to determine the spacing between the outer sidebands and their corresponding absorption features (i.e., the 2-1 and 6-5 peak splittings in Figure 4.2). We do not consider the 3-2 or 5-4 peak spacings, because the third and fourth peaks overlap and therefore have larger fit uncertainties. From



(a) Full polynomial fit to Fabry-Perot transmission, as compared to the purely linear term in that fit.

(b) Deviation from linearity of the function $f(x_j)$.

Figure 4.8: (a) Polynomial fit to Fabry-Perot peak locations, showing both the actual polynomial used and the fit with only a linear term retained. (b) Deviation from linearity of Fabry-Perot peak locations—the same fit as in (a), but without the linear term.

the two splittings that we *do* consider, we compute the average splitting. If this average splitting is not precisely 600 MHz, then the whole frequency axis must be scaled by the proper calibration factor to *make* it 600 MHz. After doing this, we have a linearized frequency axis with properly defined scale and a convenient zero.

Figure 4.9 shows histograms of splittings between EOM-induced sidebands and their absorption peaks. Note that both the 6-5 splitting and the 2-1 splitting are roughly the same, which proves that the frequency linearization scheme has worked well—before linearization, the splittings can differ by as much as a few percent. Furthermore, the fact that they are not exactly equal to 600 MHz means we need to scale the frequency axis slightly in order to ensure this axis is properly calibrated.

Hyperfine Splitting Measurement

Over the course of this thesis, we realized that this calibration scheme will also allow us to perform a high-precision measurement of the hyperfine splitting between the $6P_{1/2}(F = 4 \text{ and } 5)$ states in indium. The previous measurement of this value, reported in [26] using a Fourier-transform spectrometer, is 1251.5(1.5) MHz. We believe we can improve the 1 part in 10^3 uncertainty of this measurement. Over the course of just a few hours, we can obtain a value of 1256.4(.09), where the uncertainty refers only to statistical uncertainty (see Figure 4.10). This is in fairly good agreement with the previous measurement. We have yet to characterize the systematic uncertainties in this measurement, but presumably it will be easy to do so as we diagnose systematics in the Stark shift measurement itself. Though in good agreement with the previously measured value, it is nice to see that we get an improved

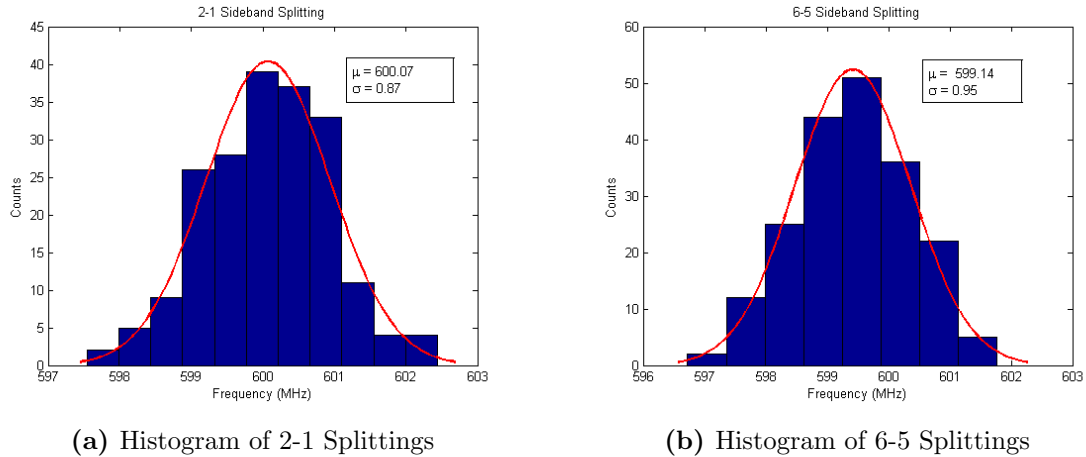


Figure 4.9: Histograms of sideband separation from absorption features for several hundred experimental runs. (a) 2-1 peak separation, (b) 6-5 peak separation. These histograms are also a good check of the linearity of the frequency axis.

precision measurement of the hyperfine splitting “for free” as we conduct the Stark shift measurement.

4.2.5 Stark Shift Determination

We now have a linearized and calibrated frequency axis. If we turn our attention to the atomic beam two-tone FM spectrum of the IR transition to the $6P_{1/2}$ state, it is now possible to determine the Stark shift.

Overlap Method

The so-called “overlap method” of shift measurement was discussed briefly in [15]. Recall that we wish to measure the *shift* between two consecutively collected data sets, and we expect the two signals used to measure the shift to look identical except for being displaced relative to one another. The overlap method can behave poorly if the signal to which it is applied is sufficiently noisy, so it is best to supplement overlap method measurements with a second shift determination. But, the overlap method does have a significant advantage in that it can be applied to any lineshape whatsoever, whether the analytic form is known or not. All that the overlap method requires is that the lineshape stay the *same* when the HV is on and off. That is, if the HV-off pattern is $\mathcal{A}(f)$ and the Stark shift is s , then the HV-on absorption pattern will be $\mathcal{A}(f - s)$. All that we must assume is that \mathcal{A} remains the same in both the HV-on and HV-off configuration; no model of the exact spectral shape is required. This wide applicability is useful. Furthermore, the overlap method is nice in that it makes use of the entirety of the collected data, as opposed to methods which rely on fitting portions of the data to a Lorentzian or Voigt profile, as in [15].

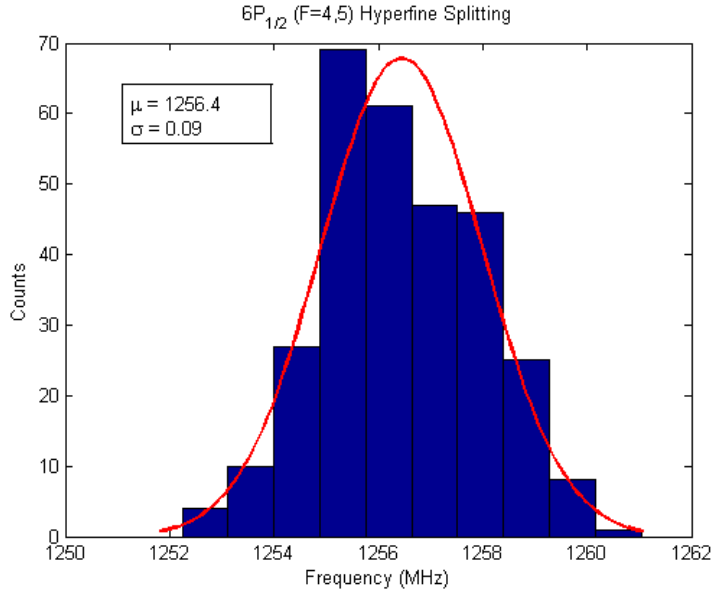


Figure 4.10: Measurement of the hyperfine structure within the indium $6P_{1/2}$ state.

If we imagine systematically sliding the HV-on signal across the frequency axis while holding the HV-off signal fixed, and take point-by-point differences between the two signals along the way, then the summed square of differences between the two signals should be minimized when the two signals overlap one another. Indeed, if the signals were *exactly* identical, the summed squared differences would be identically zero when they overlap, but noisy signals means we search for a minimum difference, rather than zero difference. The point at which the maximum overlap is found is the point at which we have “undone” the Stark shift—the shift required to obtain maximum overlap simply *is* the Stark shift.

Mathematically, for each frequency f we calculate the squared sum of difference between the HV-on signal, $\mathcal{A}(f)$, and the HV-off signal, $\mathcal{A}(f - s + x)$, where x is a shift we impose on the signal. This sum of squared differences is somewhat like a χ^2 value, so we compute that figure of merit. Expanding for x very near the actual Stark shift (i.e., for small $s - x$), we see:

$$\begin{aligned}
 \chi^2 &= \sum_{\text{all } f} \{\mathcal{A}(f) - \mathcal{A}(f - s + x)\}^2 \\
 &\approx \sum_{\text{all } f} \{\mathcal{A}(f) - (\mathcal{A}(f) - \mathcal{A}'(f) \cdot (x - s))\}^2 \\
 &= \sum_{\text{all } f} \{\mathcal{A}'(f) \cdot (x - s)\}^2 \\
 &= (x - s)^2 \sum_{\text{all } f} \{\mathcal{A}'(f)\}^2 \propto (x - s)^2
 \end{aligned} \tag{4.4}$$

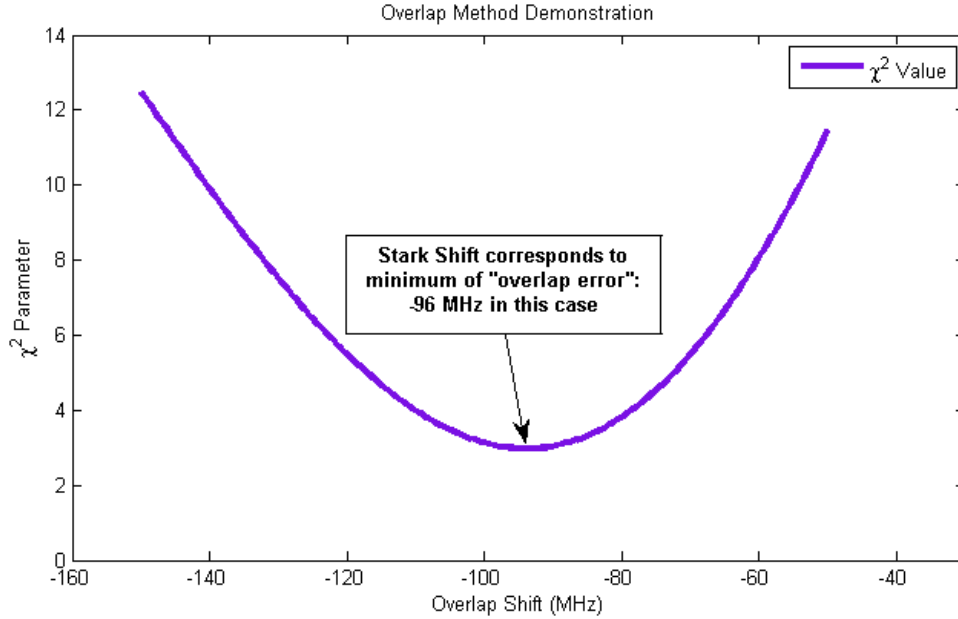


Figure 4.11: The overlap method when the HV is set to 10 kV.

Hence, for small shifts about the actual Stark shift, χ^2 is quadratic and minimized at $x = s$. Plotting the values of χ^2 as a function of manually imposed shift, x , we expect to observe a parabola which we can then minimize to find the Stark shift. Figure 4.11 shows an example of this method applied to a case where the HV is set to 10 kV. In this example the overlap method finds maximum overlap between the two signals when one is shifted by 96 MHz; numerical simulations of this situation predict a nearly 100 MHz Stark shift, in good agreement with this measurement.

Fitting to Lorentzians

Because we also know the analytic form of the two-tone FM lineshape, we can simply fit the detected spectrum to a sum of Lorentzians, and then compare the peak positions for HV-on and HV-off data sets. This is easy to do, since we already fit the hyperfine data to a sum of Lorentzians; from a practical standpoint, much of the code can be used to perform both analyses. See Figure 4.4 for an example of a full fit to six Lorentzians.

There is also physical interest in conducting the analysis this way. For the scalar polarizability we are measuring, all m_F states should experience the same Stark shift. It would be indicative of a systematic error if they did not. Therefore, if we fit the full two-tone FM signal to a sum of Lorentzians, we can measure separately the Stark shifts for the two F levels and look for any signs of broadening or shape distortion due to a tensor (or higher order) polarizability. In the present experiment, we expect to measure no differential shift. It is a useful to know that this expectation is realized.

One might reasonably wonder why we fit to Lorentzians instead of Voigt profiles, which are the true lineshape we should expect to observe. In past theses, the analysis was conducted using both Lorentzian and Voigt profile fits and it was found to affect the results very little or not at all. However, because the Voigt profiles are computationally expensive to perform, they significantly slow down the data analysis process. Therefore, given our desired precision and the other errors we expect to appear in our experiment, it is justified to fit solely to Lorentzian lineshapes.

4.3 Preliminary Results

At present, we have all the necessary pieces assembled to perform a high-precision measurement of the Stark shift in the indium $5P_{1/2} \rightarrow 6S_{1/2} \rightarrow 6P_{1/2}$ transition. It is now a fairly routine task for us to observe two-tone FM signals in the atomic beam, and to induce shifts of up to ~ 100 MHz by applying a large electric field. With the data analysis code developed, we can measure these shifts to about 1% statistical precision with a half day's worth of data. However, as was alluded to in Sections 2.4.2 and 2.4.3, we need to be very careful about interpreting these shifts: it is not immediately clear how to convert from a raw frequency shift to a particular polarizability difference.

Given the configuration of the experimental apparatus during our initial data collection, our preliminary results most closely adhere to the interpretation of Section 2.4.2— data was collected with the blue laser locked always to the field-free resonance. As that discussion implied, we should therefore expect to observe a Stark shift equal to $\delta_3 - \delta_1$, once we have corrected for the Doppler shift via Equation 2.17. After collecting a single day's worth of data, we can combine all data points taken at the same electric field value into a single shift value, and then plot the shifts versus squared electric field. The Stark shift constant, k_S , will be the slope of the resulting line, as suggested by Equation 2.11. An example of such a line is shown in Figure 4.12.

Figure 4.13 shows a histogram in which we combine all individual Stark shift measurements made during data collection— about 160 measurements made over the course of two days. We measure a difference in Stark shifts of $968.3(1.5) \frac{\text{kHz}}{(\text{kV}/\text{cm})^2}$, after correcting for the Doppler shift as described in Section 2.4.2. Converting to conventional (atomic) units for static polarizability, this gives a polarizability difference of $7878(122)a_0^3$. The 1.5% uncertainty is solely statistical error. However, we know that when we conduct the experiment without adjusting the lockpoint of the blue laser, the predominant uncertainty will come from not knowing the Rabi frequencies of the two lasers. Numerical simulations like those in Section 2.4.2 indicate that we should conservatively estimate systematic deviations from the ideal $\delta_3 - \delta_1$ result of about 5%. We thus assume a systematic uncertainty of $400a_0^3$, which should trump all other systematic errors. Adding in the known value $\alpha_0(5P_{1/2}) = 61a_0^3$ we can determine the polarizability of the $6P_{1/2}$ state. We obtain $\alpha_0(6P_{1/2}) = 7938 \pm 60(\text{stat}) \pm 200(\text{sys})$ in atomic units. This is in excellent agreement with the theoretically predicted value of $7925(300)a_0^3$ due to Safronova [6].

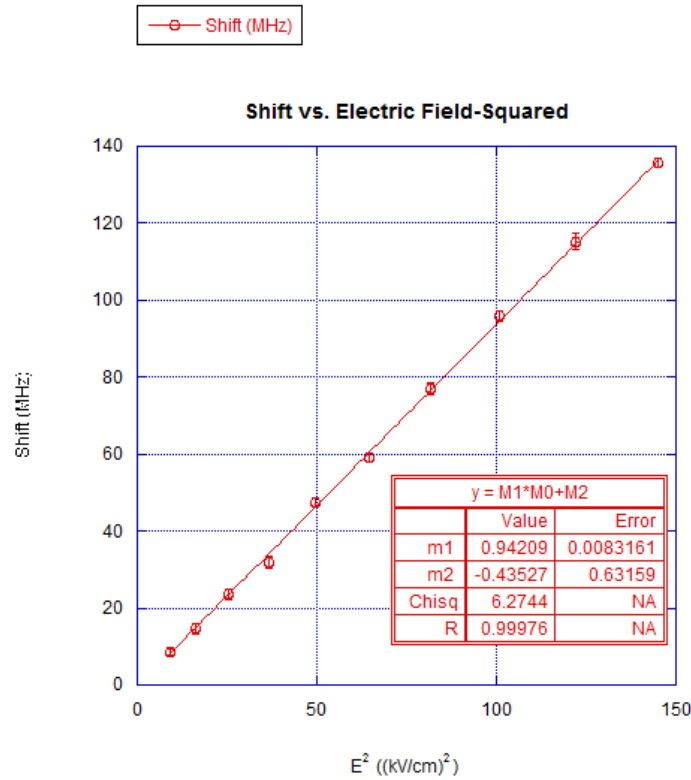


Figure 4.12: Observed shifts (including Doppler correction) plotted versus electric field squared. The slope of the line gives k_S . This represents one afternoon’s worth of data.

See Figure 4.14 for a comparison of the uncertainties in both the theoretical calculations and preliminary results of our measurement. While the error bar on the measurement includes both statistical and systematic uncertainties, the shaded bar across the plot represents only statistical error. Clearly, by updating our experimental apparatus and decreasing our systematic errors accordingly, we are on track to provide a stringent test of the theoretical calculation. We plan to improve our precision by this factor of five or more with the upgrades described in the next section.

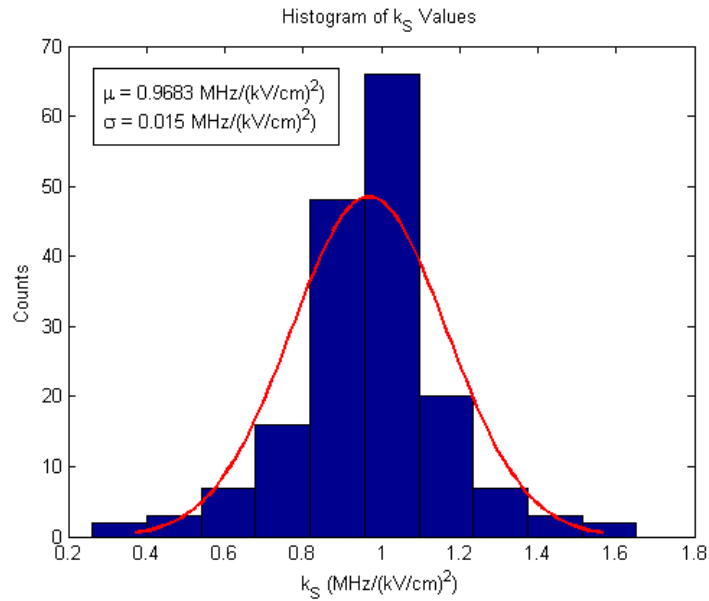


Figure 4.13: Histogram of measured k_S values in the regime where we measure the difference in Stark shifts between $6P_{1/2}$ and $5P_{1/2}$.

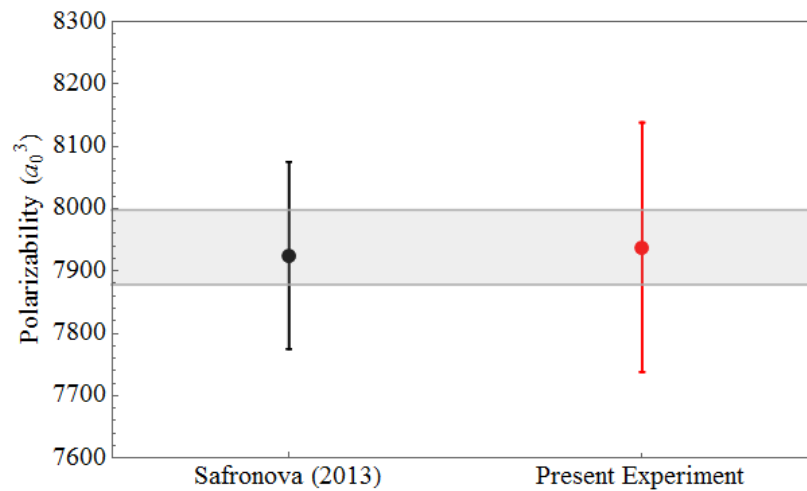


Figure 4.14: Comparison of the theory calculation and our preliminary measurement of the $6P_{1/2}$ polarizability. The shaded region includes our statistical uncertainty, whereas the error bar includes both systematic and statistical error. We expect to reduce the size of our error bar by a factor of five by improving control over the blue laser frequency, as described in the next chapter.

Chapter 5

Ongoing and Future Work

We have achieved quite a lot since the previous thesis work reported in [17]. Most significant is the observation of the two-step transition in the atomic beam unit, as that represents a crucial new finding within the Majumder lab. Additionally, our refined understanding of the three-level dynamics inherent to our system has been invaluable to our interpretation of the collected data. Even as we have made great strides toward the final goal of a 1% measurement of the $6P_{1/2}$ polarizability, some work remains. Some of this has already begun, namely modification of the experimental setup to allow us to keep the blue laser resonant with the $5P_{1/2} \rightarrow 6S_{1/2}$ transition in the atomic beam. We discuss these advances below, alongside the systematic error search necessary to complete the present experiment. Finally, we propose a few future experiments of particular interest.

5.1 Controllable Frequency Detuning in the 410 nm Transition

The data presented above was obtained without making any effort to keep the blue laser resonant with the Stark-shifted 410 nm transition in the ABU. While this yields a result that can be interpreted in terms of polarizabilities, the theory developed in Section 2.4.3 is simpler to interpret and less prone to systematic uncertainties when we keep the blue laser resonant with the atomic beam sample. Because we developed more accurate theory (including lineshapes) when the blue laser remains resonant with the atomic beam, it is desirable to run the experiment in this regime. The goal is this: keep the blue laser locked to the center of the field-free 410 nm transition using a vapor cell while *simultaneously* shifting the frequency of the portion going to the ABU to stay on resonance with the atomic beam whenever the HV is on. We are currently adapting the apparatus to allow us to do so. This requires the addition of optical elements which allow for the shifting of the blue laser's frequency by up to ~ 50 MHz (the largest Stark shifts expected in the lower transition).

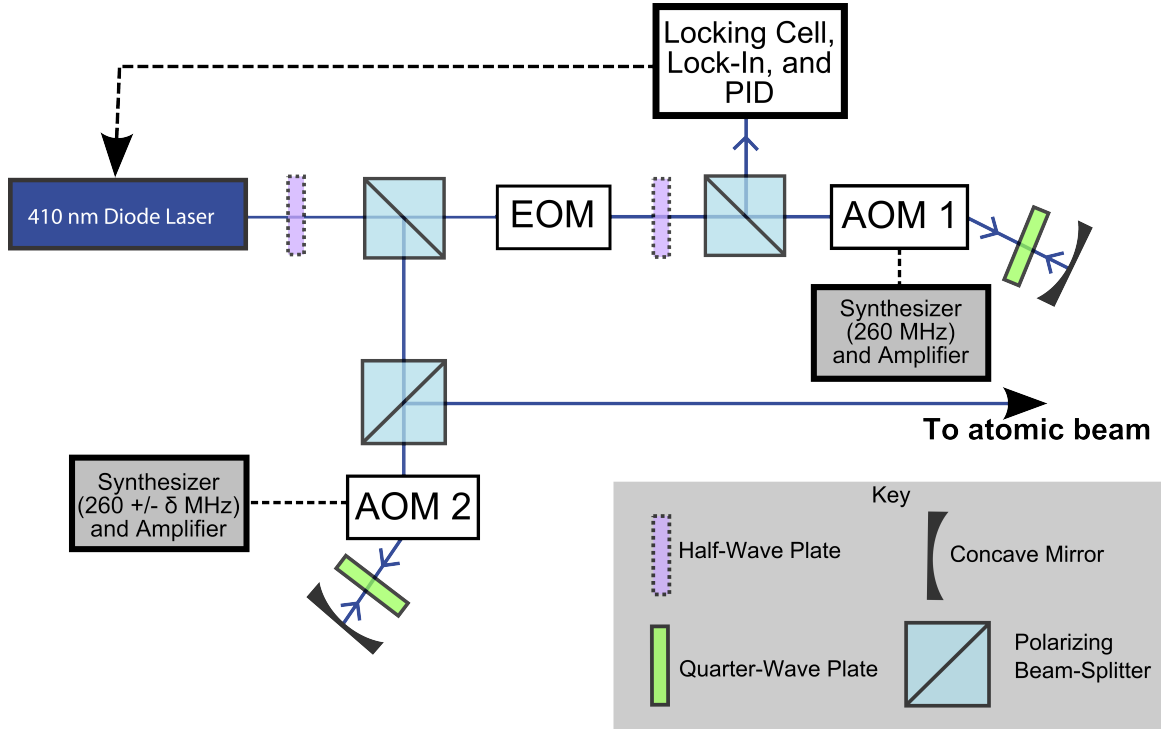


Figure 5.1: The new optical setup, which keeps the blue laser on resonance with the atomic beam whenever the HV is on. We have added two AOMs and the necessary polarization optics to double-pass both. The vapor cell locking system remains locked to the center of a field-free resonance.

A simplified diagram of the new optical setup for the 410 nm laser is shown in Figure 5.1. We have added two acousto-optic modulators (AOMs).¹ Typically, we only wish to work with the first-order diffracted beam, and it is possible to direct about 70% of the input light into a given first-order beam with frequency shifted by ω_d . However, the diffraction angle of the AOM's output depends on the drive frequency, unless the AOM is double-passed (by sending light through in both directions). To make sure our alignment is not affected as we tune the AOM drive frequency, we must double-pass both AOMs. Both AOMs are driven by newly installed RF signal generators from WindFreak Technologies (SynthNV). The RF generators are, in turn, controlled via LabView software incorporated into the overall experimental control program.

AOM 1, added after the EOM in the laser locking setup (see Figure 3.4 for a review) is driven at 260 MHz and double-passed. It thus shifts the frequency by a total of 520 MHz, when we double-pass it and pick out the first-order diffracted

¹An AOM is a device in which RF power drives sound waves in a crystal through which we pass our blue laser. The input light then diffracts off the traveling waves in the crystal, and the output light is the product of interference very much like in Bragg diffraction. Suppose we drive the AOM at frequency ω_d , in the RF regime, and the input light has frequency ω_c . The diffracted beams then have frequencies $\omega_c, \omega_c \pm \omega_d$, and so on for higher orders.

beam each time. This light is then used to lock the laser exactly as described in Section 3.2.2. Because the light used for locking the laser is shifted by 520 MHz, we actually lock 520 MHz *below* resonance. If we did nothing else, the beam going to the ABU would thus be 520 MHz below resonance as seen by the atoms in the vacuum chamber. We correct for this by sending the rest of the blue laser’s output through AOM 2 in a similar double-pass configuration. We also drive this AOM at about 260 MHz, and pick out the same first-order diffracted beam (i.e., always the *plus* first-order beam). When AOM 2 is driven at 260 MHz and double-passed, the light is shifted *back* up by 520 MHz, and the light going to the atomic beam is exactly on resonance with the field-free atoms. With this configuration, we have not shifted the blue light at all; we have simply constructed an elaborate method of delivering light to the ABU which is resonant with the vapor cell atoms.

But suppose we drive AOM 2 at $260 - \delta$ MHz, where $2\delta = k_S(6S - 5P)\mathcal{E}^2$. Now the light going to the atomic beam is at frequency 2δ below field-free resonance. 520 MHz of the shift induced by AOM 2 is used to counteract the 520 MHz shift from AOM 1, and the other -2δ is uncompensated and therefore remains as an overall frequency shift. We can choose to make 2δ exactly the Stark shift whenever the HV is set to some particular value, and therefore easily shift the blue laser’s frequency to be always resonant with the atomic beam. In this way, we exactly achieve the situation described by the Hamiltonian in Equation 2.18.

With these new optics in place, we will be able to retake data while the blue laser remains resonant with the atomic beam. If we choose 20 kV as the maximum HV setting at which to take data, we must compensate for the up to 50 MHz Stark shift induced when the field is on. This will be easy to do, by simply driving AOM 2 down to 235 MHz (i.e., 25 MHz below AOM 1). The diffraction efficiency drops off away from an AOM’s center frequency, but not so quickly as to cause problems for this application. Doing this, we expect to measure the difference in Stark shifts between the $6P_{1/2}$ and $6S_{1/2}$ states. We can then back out a value of the $6P_{1/2}$ polarizability, using the high precision measurement of the lower state polarizability previously completed by our lab [12]. Numerical simulations mentioned briefly in Section 2.4.3 suggest this measurement method is less prone to systematic errors than if we simply left the blue laser locked to a field-free sample. Nonetheless, when there are two ways to measure a given quantity, it is nice to try both and see whether they agree—the results described above are still a useful point of comparison.

5.2 Systematic Error Searches

With the new optical setup completed, we must collect much more data and analyze it while looking for potential systematic errors. The experience our group has gained on past Stark shift measurements is an important guide in identifying where systematic errors might lurk. Once we have identified potential systematic errors, we must search the collected data for any signs of their influence. In some cases, where the systematic effect might be due to a “binary” variable (i.e., dependent on whether a

given experiment setting is on or off), we will want to bin the data into two groups, and see whether they yield the same value for the polarizability. In the case of “continuous” variables, we will want to vary the parameter over some wide range and make sure no effect is seen on the measurement. If an effect is seen in either of these cases, we must then aim to eliminate it or, at worst, include it in an error budget so that we understand the true uncertainty in our measurement. We will now outline some of the most obvious potential systematic errors.

5.2.1 Continuous Variables

The parameters that we can adjust continuously over some range include the IR laser sweep speed and the laser power of both the blue and IR lasers. We are particularly concerned about the laser powers, as the simulations in Section 2.4 suggest that those are potential sources of systematic shifts that could bias our measurements.

Laser Sweep Speed

Over the course of this year, we noticed that some of our data depends on the speed at which we sweep the IR laser over resonance. This is an effect that has been identified by previous students, and we think we understand its origins. Sweeping the laser too slowly (about 0.1 Hz or below) allows time for the PZT generating the sweep to drift. Particularly when we are trying to measure a Stark *shift*, this drift is of concern because any distortions of the frequency axis will appear to be part of the measured shift. Sweeping too quickly is also a concern, because of the nonlinearity in the PZT’s relationship to inertial effects. If we drive the PZT at very high frequencies (much faster than 1 Hz), this nonlinearity might be exacerbated. Sweeping either too quickly or too slowly is usually diagnosed via an asymmetry in values obtained from upscans vs. downscans, as to be discussed shortly.

Basing our zero of frequency on an atomic feature attempts to assuage some of this concern. However, we even noticed the effect when trying to measure hyperfine splittings in the $6P_{1/2}$ state, where it appears as an anomalously large measurement of the splitting. Therefore, data should be taken at a variety of sweep speeds between about 0.5 Hz and 5 Hz, to make sure that no systematic error has been introduced because of the rate of sweep. This necessarily entails a trade-off between sweep speed and signal quality, particularly because the two-tone FM signal has decreasing signal-to-noise with increasing sweep speed.

Laser Power

As was described in Section 2.4, the Stark shift we measure will be affected by the powers of both lasers. If the measurement is performed keeping the blue laser locked to the field-free resonance, as it was for the preliminary data analysis, then we expect to measure the Stark shift as $\delta_3 - \delta_1$ so long as the Rabi frequencies of the two lasers

are similar to one another (within about a factor of two), based on Figure 2.8 and Mathematica simulations which can be seen in Appendix C.

Once we have completed the updated optical setup described in Section 5.1, we mainly need to worry about the ratio of laser powers. As described in Section 2.4.3, so long as $\Omega_1 < 0.7\Omega_2$ is satisfied, we expect the resonance to be a singly peaked function, with the peak at precisely $\Delta_{32} = \delta_3 - \delta_2$. Changing the laser powers broadens and eventually splits this peak, but the line-center is always at the difference between the Stark shifts in the upper two levels. With the new optical setup, we therefore want to perform the measurement at many different blue laser power values and make sure that the measured value does not change as a result. If it did, this would imply the measurement we are making involves some kind of AC Stark shift which we must exclude before determining the polarizability of the $6P_{1/2}$ state. Presumably this would imply extrapolating to zero blue power.

The broadening and/or splitting of the resonance in a two-step transition as the Rabi frequency of the lower transition is increased is the well-known Autler-Townes splitting [27]. We have already begun searching for signs of this effect in our data by varying the blue laser power as much as possible and looking for broader or doubly peaked resonances, but see no such effect. Because the dipole moment connecting the $5P_{1/2}$ and $6S_{1/2}$ states is intrinsically 3 to 4 times smaller than the dipole moment between the $6S_{1/2}$ and $6P_{1/2}$ states. Hence, the fact that we see no signs of Autler-Townes splitting is most likely because we never reach the regime in which we are driving the lower transition as strongly as we drive the upper transition.

k_S vs. \mathcal{E}

It is useful to plot the analyzed data for the Stark shift slope (k_S) versus the applied field (\mathcal{E}) to make sure that we measure the same Stark shift regardless of the applied field. This is especially important for a two-step transition like the one we are investigating. As has been described above, when we collected data without keeping the blue laser resonant with the atomic beam, we move toward progressively more “virtual” first-step transitions as \mathcal{E} increases. One might well worry that the measured polarizability will be more like $\delta_3 - \delta_2$ at lower \mathcal{E} and more like $\delta_3 - \delta_1$ at higher \mathcal{E} . We see some evidence of this effect in the preliminary data analysis, but not enough to be conclusive. Even once we have finished upgrading the optical setup to keep the blue laser resonant with the atomic beam, we still want to ensure that the Stark shift value k_S remains constant with increasing \mathcal{E} .

For instance, in the preliminary results we do not observe a variation in the measured value of k_S as a function of \mathcal{E} . This gives us confidence that some of the three-level dynamics described in Section 2.4.2 are not encountered within the regime of laser power and electric field that we run our experiment. If there *were* some kind of complication, we would observe it as a non-linearity in the observed shift vs. electric field plots, which is to say as a field-dependence in the measured k_S value.

5.2.2 Binary Variables

A number of other adjustable parameters come in discrete groups. A proper systematic error search must therefore involve separating out data collected in each configuration and performing separate analyses, followed by comparison to ensure that no measurable difference is observed. Wherever one *is* seen, care must be taken to find its source and attempt to remove it. See Figure 10 in [12] for an example of these sorts of comparisons.

Upscans vs. Downscans

The most natural binary pair is data collected as an upscan versus a downscan. In the previous Stark shift measurement conducted by our group [12], upscans vs. downscans was one of the only binary variables in which statistically significant differences were measured in the Stark shift. This must indicate some kind of issue with the laser, and that work deduced that it indicated non-single-mode operation at the very beginning or end of a sweep. The hysteresis in the laser scan would therefore treat upscans and downscans differently and introduce errant (multi-mode) laser frequencies into the scan in only one direction. We should be on the lookout for similar effects, and make every effort to improve the single-mode quality of the IR laser during data collection to minimize this uncertainty.

Laser Polarization

Another statistically significant difference that was observed in [12] was related to the laser polarization. For us, it is important to worry not only about the overall polarization but also the relative polarization between the two laser beams. The polarization of the laser beam should have no effect on the measurement of a static polarizability. However, it is important to check that this turns out to be the case.

HV Switching Direction

Comparing HV on-to-off and off-to-on switching direction is important to diagnose any potential problems with the electric field plates. Because we are measuring a relative shift, it should of course not matter which direction the HV switches. However, it is very easy to bin our data so that different switching directions are analyzed separately: the first run in any trial always goes from HV off to HV on, so even-numbered datasets all switch in one direction, and odd-numbered datasets switch in the opposite.

Fitting Method

To ensure that the data fitting protocol does not introduce any unnecessary errors into the measurement, we will fit all datasets using multiple fitting methods. As discussed previously, there are reasons to think that the “overlap method” might not

work well for noisy data; however, it has the advantage of making use of *all* the data, whereas fitting to individual peaks essentially partitions the data into only six regions of interest. In the same vein, different methods of frequency linearization (fitting to an Airy function vs. fitting to a sum of Lorentzians) might produce slightly different frequency axes.

It is not particularly time consuming to conduct any individual fit, so we must make sure that all fitting methods agree. If they do, this encourages us that the results we observe are robust. If they do not, we must check the code for small mistakes, or at least determine which fitting method is more trustworthy than the others. At the very least, we should conduct the final analysis using two different methods of frequency linearization, and two methods of Stark shift extraction.

5.3 Future Work

Even with some work remaining in the present experiment, we can cast an eye forward to exciting future work. Because this thesis demonstrates the possibility of observing two-step transitions in the atomic beam, there are many possible experimental paths to pursue.

5.3.1 Inferred $5D_{3/2}$ State Mixing

Before conducting any new experiment, we can use the expected results from the present experiment to determine the $5D_{3/2}$ reduced electric dipole (E1) matrix element. The $5D_{3/2}$ state is the main contributor to the polarizability. We can then compare two methods of calculation used by Safronova to determine which is more accurate. Based on Equation 3 in [6], one way to write the scalar polarizability is as:

$$\alpha_0(6P_{1/2}) = \frac{1}{3} \sum_n \frac{|\langle n || d || 6P_{1/2} \rangle|^2}{E_n - E(6P_{1/2})} \quad (5.1)$$

where $|d\rangle$ is the reduced E1 operator. We can isolate the term contributed by the $5D_{3/2}$ state to this sum, and call the difference between the measured polarizability and the balance of the infinite sum C . Then,

$$\langle 5D_{3/2} || d || 6P_{1/2} \rangle = \sqrt{3|E(6P_{1/2}) - E(5D_{3/2})|C} \quad (5.2)$$

Suppose we reach our desired results of measuring Δ_{32} to 1% precision. Using the measurement of Δ_{21} completed in [12] (with 0.3% uncertainty) and the theoretical value of the polarizability in the $5P_{1/2}$ state, we can determine a measurement for the polarizability $\alpha_0(6P_{1/2})$ with no loss of precision. The inferred value of C should then be found to about 1-2% uncertainty. Given these presumed values, we should be able to determine $\langle |d| \rangle$ to between 0.5 and 1%. In [6], the matrix element prediction differs by about 2% depending on whether the coupled-cluster (CC) or configuration interaction (CI) calculation method. We should therefore be able to obtain a precise

enough result to determine, in this particular case, which method is more valid. This is truly valuable feedback for the theorists.

5.3.2 Polarizability in the $6P_{3/2}$ State

The most obvious experimental extension is to perform an analogous measurement of the polarizability in the $6P_{3/2}$ state of indium. Due to its higher j value, the $6P_{3/2}$ state is more complicated—one might therefore say more *interesting*—than the $6P_{1/2}$ state. See Appendix E for a discussion of such states. There are *four* hyperfine states to worry about: $6P_{3/2}(F = 3, 4, 5, 6)$. Because $j = 3/2$, this state will exhibit both scalar and tensor polarizabilities. Due to the tensor polarizability, different m_F levels will shift by different amounts, meaning we will resolve the magnetic sublevels when the electric field is on [6]. There are now two quantities of interest, α_0 and α_2 , where the former is a scalar polarizability and the latter is the tensor component. By measuring how two m_F levels shift, we can back out information about both the scalar and tensor polarizability of the state. See Section E.1 for a derivation of this effect. The Safronova group has already predicted the value of this tensor polarizability in [6]. In the indium $6P_{3/2}$ state, she predicts that $\alpha_0 = 10500(400)$ and $\alpha_2 = -1432(45)$, both in units of a_0^3 . We simply need to tune the IR laser from 1343 nm down to 1291 nm in order to reach this state.

5.3.3 Analogous Measurements in Thallium

Recall from Figure 1.1 that thallium is very much like indium, except all levels are one principal quantum number larger. Nonetheless, very similar laser radiation can be used for the analogous transitions in these two elements. We briefly explore some options here. Thallium does have the disadvantage of being highly poisonous. We should therefore have a string of thallium experiments planned before loading thallium into the atomic beam unit again; we would like to maximize the science-to-danger ratio.

Thallium $7P_{1/2}$ Polarizability

Much of our interest in indium is its structural similarity to thallium. We are therefore interested in measuring the thallium $6P_{1/2} \rightarrow 7S_{1/2} \rightarrow 7P_{1/2}$ transition. This is exactly the transition studied in [13]. A UV laser at 378 nm, already in use in the Majumder lab, is needed to excite the first transition, while the same IR laser used in the present experiment can be tuned to 1301 nm to excite the second-step transition. The experiment would then proceed exactly like the current indium experiment, with thallium loaded into the atomic beam unit in the place of indium.

In [7], Safronova has predicted the scalar polarizability in each of these states as: 50.0(3.0) for the $6P_{1/2}$ state, 881(25) for the $7S_{1/2}$ state, and 4918(120) for the $7P_{1/2}$ state, all in units of a_0^3 . These are all of the same order as the analogous polarizabilities in indium. At the same time, thallium has a much larger optical

depth for a given temperature than indium. It is therefore much easier to detect absorption in a thallium beam, and we could likely conduct the experiment without any complicated FM signal processing tricks.

Thallium $7P_{3/2}$ Polarizability

For the same reasons that we are motivated to study the $6P_{3/2}$ polarizability in indium, it would be desirable to measure the $7P_{3/2}$ polarizability in thallium. This has all the added complications and interests related to the $j = 3/2$ final state, but is simplified by the fact that there are only $F = 1, 2$ hyperfine levels. While the UV laser would be left tuned to the 378 nm $6P_{1/2} \rightarrow 7S_{1/2}$ transition, we would need a new IR laser that can be tuned to the 1151 nm $7S_{1/2} \rightarrow 7P_{3/2}$ line. Beyond this, there is no difference between this proposed experiment and the proposed indium $j = 3/2$ measurement. See Section E.2 for a discussion of how the tensor polarizability can be measured in this state.

Thallium $8P_{1/2}$ Polarizability

In the interest of conducting an experiment for which we already own the requisite lasers, we could instead study the thallium $6P_{1/2} \rightarrow 7S_{1/2} \rightarrow 8P_{1/2}$ transition. The Majumder lab began studying this transition in [13], although that work is currently ongoing. We have a home-built laser which can be tuned to the 671 nm second-step transition. Because this is also a $j = 1/2$ state, it is simpler than the $7P_{3/2}$ state mentioned above, and the relevant theory has yet to be conducted. Nonetheless, we are technologically capable of performing this measurement. It would also spur interest in theoretical treatments of the thallium $8P$ state, and thus represent a new test of atomic theory in increasingly excited states.

Appendix A

Spectroscopy Derivations

In this Appendix, we fill in details related to absorption and FM spectroscopy. We derive the fundamental lineshapes due to lifetime and Doppler broadening and then go on to derive the demodulated lineshapes for both single-tone and two-tone FM spectroscopy.

A.1 Lifetime Broadening

Denote the finite lifetime by τ . Now, the Heisenberg Uncertainty Principle tells us that $\Delta E \Delta t \gtrsim \hbar$. For a state with lifetime $\Delta t \sim \tau$, we thus have the requirement that $\Delta E \sim \frac{\hbar}{\tau}$. If the energy of the state is “smeared” out like this, then light detuned from the true resonance frequency by up to $\Delta\omega = \Delta E/\hbar$ can still drive the transition. This is equivalent to saying that the transition has been broadened from a pure delta function in frequency to a function with characteristic width Γ , where

$$\Gamma = \frac{\Delta\omega}{2\pi} = \frac{\Delta E}{2\pi\hbar} = \frac{1}{2\pi\tau} \quad (\text{A.1})$$

This determines the *width* of the lifetime broadening, but what of the lineshape? We follow [28] and assume the excited electron can be modeled as a damped harmonic oscillator. If the lifetime is Γ and the frequency splitting between the two states in the transition is ω_0 , then the electron under this model has some amplitude $x(t)$ which satisfies

$$\ddot{x} + \Gamma\dot{x} + \omega_0^2 x = 0 \quad (\text{A.2})$$

Assuming the emitted or absorbed light is near resonant ($\omega \approx \omega_0$) and the natural linewidth Γ is much less than the transition frequency (which is always the case for the transitions we study), Equation A.2 has the solution

$$x(t) = x_0 e^{-\Gamma/2t} \cos(\omega_0 t) \quad (\text{A.3})$$

Now, due to its decaying amplitude, $x(t)$ is not monochromatic. We can determine its Fourier components easily:

$$A(\omega) = \frac{1}{\sqrt{2\pi}} \int_0^\infty x(t) e^{-i\omega t} dt \quad (\text{A.4})$$

$$= \frac{x_0}{\sqrt{8\pi}} \left(\frac{1}{i(\omega - \omega_0) + \Gamma/2} + \frac{1}{i(\omega + \omega_0) + \Gamma/2} \right) \quad (\text{A.5})$$

where the lower integration limit is taken to be 0 (instead of $-\infty$) because we can assume $x(t) = 0$ for $t < 0$. But the *intensity* is given by the absolute value squared of this frequency spectrum. When we calculate $P(\omega) = A(\omega)A^*(\omega)$ we can neglect terms with $\omega + \omega_0$ in the denominator, as these will be very small, in which case:

$$P(\omega) = \frac{\Gamma^2/4}{(\omega - \omega_0)^2 + \Gamma^2/4} \quad (\text{A.6})$$

where we have chosen the numerator such that the lineshape is equal to 1 on resonance. The lineshape is a *Lorentzian* with full-width-at-half-maximum (FWHM) Γ and center at $\omega_0 = (E_2 - E_1)/\hbar$, where E_1 and E_2 are the energies of the lower and upper states in the transition, respectively.

A.2 Doppler Broadening

The well-known Doppler effect states that the observed frequency of light will depend on the observer's motional state. If a laser beam has frequency ω in the lab frame, then in the frame of an atom moving with velocity v toward (away from) the laser source the frequency will be observed to be at ω' , which is higher (lower) than ω : a so-called blue-shift (red-shift). Assuming $v \ll c$,

$$\omega' = \omega \left(1 + \frac{v}{c} \right) \quad (\text{A.7})$$

This means that even far-off resonant light can still be absorbed by an atom, provided it moves with a large enough velocity relative to the laser. In many cases, most notably in a heated vapor cell, we deal with a sample atoms that can be described by a Maxwell-Boltzmann distribution of velocities. When this is the case, a broad range of laser frequencies will be significantly absorbed, as we can imagine partitioning the atoms into various velocity classes, each of which absorbs light which is Doppler-shifted onto resonance in those atoms' reference frame. As opposed to lifetime broadening, which affects all atoms equally, Doppler broadening is thus a sort of *inhomogeneous broadening* mechanism, affecting atoms differently depending on their motion relative to the laser beam.

We again follow [28] to derive the actual lineshape. For a sample of atoms in equilibrium at temperature T , assume there are $n(v)dv$ atoms per unit volume in an energy level of interest. Then the Maxwell-Boltzmann distribution says that

$$n(v)dv = \frac{N\sqrt{m}}{\sqrt{2\pi kT}} e^{-mv^2/2kT} dv \quad (\text{A.8})$$

where N is the density of all atoms in the energy level, m is each atom's mass, and k is the Boltzmann constant. But Equation A.7 tells us how the velocity and observed frequencies are related, hence:

$$n(\omega)d\omega = \frac{Nc\sqrt{m}}{\omega_0\sqrt{2\pi kT}} e^{-mc^2(\omega-\omega_0)^2/2\omega_0 kT} d\omega \quad (\text{A.9})$$

which is, as predicted, a Gaussian lineshape with full width at half maximum

$$\Delta = \frac{\omega_0}{c} \sqrt{\frac{8kT \ln 2}{m}} \quad (\text{A.10})$$

This Δ is the Doppler width. As stated in Section 2.1, the width is about 1.6 GHz for the 410 nm transition in the vapor cell, but only about 100-200 MHz for the same transition in the ABU. This demonstrates the narrowing achieved by collimating the atomic beam and probing the atoms transversely.

A.3 Single-Tone FM Lineshape Derivation

The single-tone FM lineshape is derived as follows. Before any modulation, the laser's output is assumed to be monochromatic at frequency ω_c (~ 100 THz). At some point in space, the field can be written as

$$\tilde{E}(t) = E_0 e^{i(\omega_c t + \phi)} \quad (\text{A.11})$$

We then pass the beam through an EOM. This has the effect of changing the phase:

$$\phi \rightarrow \beta \sin(\omega_m t) \quad (\text{A.12})$$

where β is called the modulation depth and is a quantity that describes how strongly we are modulating the field.¹ (Typically, $\beta \ll 1$. However, see [29] for an exploration of high modulation depths.) Hence, the EOM adds a time-dependent phase to the laser's electric field, and the time dependence is set by the modulation frequency. We now express the electric field as

$$\tilde{E}(t) = E_0 e^{i(\omega_c t + \beta \sin(\omega_m t))} = E_0 e^{i\omega_c t} e^{i\beta \sin(\omega_m t)} \quad (\text{A.13})$$

The proper mixture of squinting and becoming familiar with the literature on FM theory reminds us of a similarity between Equation A.13 and the generating function for (of all things) Bessel functions [30], i.e.

¹We note in passing that, technically, what we have described is *phase* (rather than frequency) modulation— but these two sorts of modulation are equivalent up to an arbitrary choice of phase [15, 18].

$$e^{x(1/2)(h-h^{-1})} = \sum_{n=-\infty}^{\infty} h^n J_n(x) \quad (\text{A.14})$$

Making the identifications: $h \rightarrow e^{i\omega_m t}$ and $x \rightarrow \beta$, Equation A.14 becomes

$$\exp(\beta/2(e^{i\omega_m t} - e^{-i\omega_m t})) = e^{i\beta \sin(\omega_m t)} = \sum_{n=-\infty}^{\infty} e^{in\omega_m t} J_n(\beta) \quad (\text{A.15})$$

The second equality in Equation A.15 is typically known as the Jacobi-Anger expansion. This identity allows us to re-express Equation A.13 in a useful way: we can write the electric field as a piece oscillating at the laser frequency ω_c with an infinite set of frequency sidebands, each separated from that central frequency by an integer multiple of ω_m and weighted by the n^{th} Bessel function evaluated at β . That is,

$$\tilde{E}(t) = E_0 e^{i\omega_c t} \sum_{n=-\infty}^{\infty} J_n(\beta) e^{in\omega_m t} \quad (\text{A.16})$$

$$= \sum_{n=-\infty}^{\infty} E_0 J_n(\beta) e^{i(\omega_c + n\omega_m)t} \quad (\text{A.17})$$

We can visualize the frequency spectrum post-modulation by plotting the amplitude of each frequency component as a function of frequency. If we send the laser beam through a Fabry-Perot cavity, we observe the typical Airy function pattern, but now with sideband peaks separated from the central peaks by ω_m [15]. See Figure A.1. Now the interpretation of β as the modulation depth becomes clear: as β increases, more power is redistributed from the central carrier frequency to the sidebands.

Once the laser field has been modulated, we allow it to interact with a sample of atoms. The sample will absorb near-resonant light. Depending on the physical situation of the atomic sample, the absorption lineshape will correspond to a Gaussian, Lorentzian, or some combination; these are described in Section 2.1. The transmitted light will therefore be the incident light multiplied by a (frequency-dependent) transmission factor, $T(\omega)$: $\tilde{E}_T = T(\omega)\tilde{E}$. Hence,

$$\tilde{E}_T(t) = \sum_{n=-\infty}^{\infty} E_0 J_n(\beta) T(\omega_c + n\omega_m) e^{i(\omega_c + n\omega_m)t} \quad (\text{A.18})$$

In this experiment, all modulation is limited to $\beta \lesssim 0.2$, so the fact that only the zeroth and first Bessel functions are non-negligible for small arguments means we can approximate Equation A.17 as being a sum over only $n = -1$ to 1 .² With this approximation, and noting that $J_{-n}(\beta) = (-1)^n J_n(\beta)$, we have

²Once again, see [29] for a more general treatment.

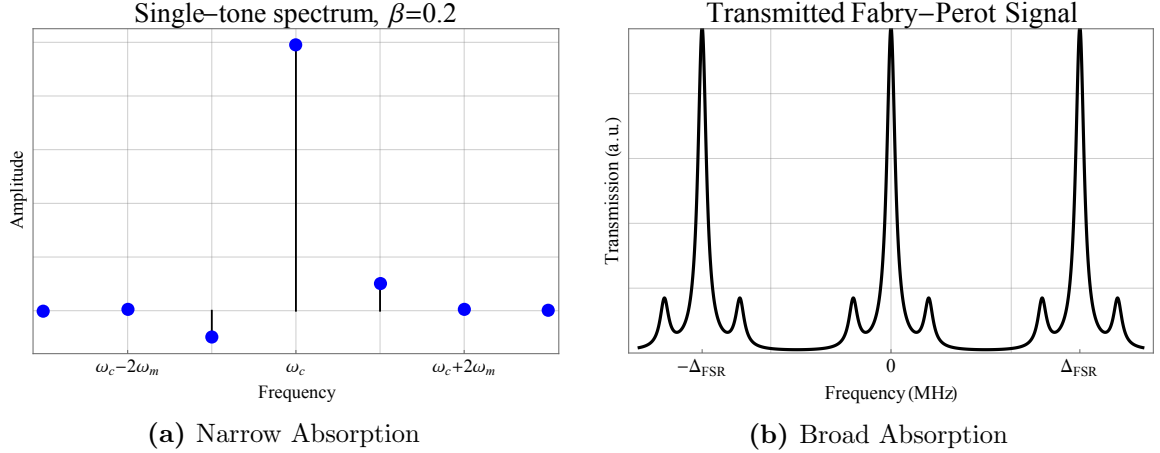


Figure A.1: (a) Single-tone FM spectrum. Signs indicate relative phase of each frequency component. (b) Fabry-Perot transmission signal. In this case, $\beta = 0.2$, which is typical of the modulation depths used in this experiment. Note that only the carrier and first set of sidebands are prominent at these low modulation depths.

$$\tilde{E}_T(t) \approx E_0 e^{i\omega_c t} \{ J_0(\beta)T(\omega_c) + J_1(\beta)T(\omega_c + \omega_m) - J_1(\omega_c - \omega_m) \} \quad (\text{A.19})$$

Now, detecting this light with a photodiode, we detect a time-averaged intensity: $I(t) \propto \langle \tilde{E}_T^* \tilde{E}_T \rangle$. However, we must be slightly careful in what we average over: choosing a detector with a sufficiently high bandwidth, we can observe oscillations at the modulation frequency (and perhaps higher harmonics of the modulation frequency), but not all the way at optical frequencies. Squaring Equation A.19 is simple but tedious, so we simply quote the result from [17]:

$$\begin{aligned} I(t) &\propto T^2(\omega_c)J_0^2(\beta) + T^2(\omega_c + \omega_m)J_1^2(\beta) + T^2(\omega_c - \omega_m)J_1^2(\beta) \\ &+ \cos(\omega_m t)J_0(\beta)J_1(\beta) \{ T^2(\omega_c)T^2(\omega_c + \omega_m) - T^2(\omega_c)T^2(\omega_c - \omega_m) \} \\ &- \cos(2\omega_m t)J_1^2(\beta) \{ T^2(\omega_c - \omega_m)T^2(\omega_c + \omega_m) \} \end{aligned} \quad (\text{A.20})$$

Finally, suppose we wish to detect the signal oscillating at ω_m . This amounts to using a lock-in amplifier for demodulation. The demodulated intensity is simply the coefficient of the cosine term in Equation A.20:

$$I_{\text{demod}}(t) = J_0(\beta)J_1(\beta) (T^2(\omega_c)T^2(\omega_c + \omega_m) - T^2(\omega_c)T^2(\omega_c - \omega_m)) \quad (\text{A.21})$$

$$\propto T^2(\omega_c + \omega_m) - T^2(\omega_c - \omega_m) \quad (\text{A.22})$$

Imagine scanning the laser frequency, ω_c , across an atomic transition from below. When ω_c is far below the resonance frequency, the light is entirely transmitted; when ω_c is below resonance by precisely ω_m , the upper sideband is predominantly absorbed;

when ω_c is precisely on resonance, the two sidebands (being equally spaced on either side of ω_c) are equally absorbed; when ω_c is above resonance by ω_m , the lower sideband is predominantly absorbed; finally, when ω_c is far above resonance, essentially all light is transmitted. In the end, it turns out that the demodulated signal (Equation 2.2) is merely proportional the difference in absorption of the two first-order sidebands. We therefore expect to see two peaks: one when each sideband happens to be resonant with the transition being probed. This can be seen in Figure 2.2.

A.3.1 Alternative Single-Tone Lineshape Derivation

In the presence of a Doppler-broadened transition, the absorption of the two sidebands blend together and produce a smooth, nearly linear central portion. (See Figure 2.2b.) The demodulated signal looks like a dispersion curve. Over the course of this thesis, we realized that such a curve is an ideal signal for stabilizing our laser system.

Instead of picturing frequency modulation as a method of adding sidebands to the laser spectrum as done above, consider the idea that it induces a “dithering” of the laser frequency about some central value (which we can scan, for instance across an atomic transition). In this sense, demodulation with a lock-in amplifier will be shown to be akin to “taking a derivative.” Mathematically, this dither means that

$$\omega_c \rightarrow \omega_c + \beta \sin \omega_m t \quad (\text{A.23})$$

$$\implies T(\omega_c) \rightarrow T(\omega_c + \beta \sin \omega_m t) \quad (\text{A.24})$$

We assume throughout this thesis that $\beta \ll 1$. So long as $T(\omega)$ is a slowly varying function (in other words, $\beta \ll \omega_c$, and the Doppler width is much larger than ω_m), we can make the approximation:

$$T(\omega_c + \beta \sin \omega_m t) \approx T(\omega_c) + \beta \sin \omega_m t T'(\omega_c) \quad (\text{A.25})$$

Here, a prime indicates differentiation with respect to the argument (frequency, not time). Suppose we pick out the signal oscillating at ω_m . From Equation A.25, this is clearly $\propto T'(\omega_c)$, the derivative of the transmission factor. Our lock-in amplifier thus functions as a “derivative-taker.” This demodulated signal looks like a typical dispersive lineshape. In the limit of large Doppler broadening (a reasonable assumption given the experimental parameters described in Chapter 3), this derivative looks exactly like the FM demodulated lineshape shown in Figure 2.2.

It is nice to be able to derive the dispersion-like lineshape from this separate perspective, especially because of the usefulness of the signal for laser locking purposes. A practical explanation of how such a lock is achieved is provided in Section 3.2.2, but the foregoing discussion provides the theoretical basis for the method.

A.4 Two-Tone FM Lineshape Derivation

Deriving the two-tone FM demodulated lineshape is quite similar to spirit to the approach taken in Section A.3. Starting again at Equation A.11, we pass a monochromatic laser beam through an EOM. This time, however, we drive the EOM at two frequencies which are very close to one another: choose the frequencies $\omega_m \pm \Omega$ satisfying the condition that $\Omega \ll \omega_m$. We also assume that $\Omega \ll \Gamma_{\text{Dopp}}$, whereas $\omega_m \gg \Gamma_{\text{Dopp}}$ (where Γ_{Dopp} is the relevant Doppler width). Using the same argument invoked in Equation A.12, we write the time-dependent electric field which contains the carrier oscillation at ω_c , and now *two* extra arguments, one for each modulation frequency. That is:

$$\begin{aligned} \tilde{E}(t) &= \tilde{E}_0 e^{i(\omega_c t + \beta_- \sin(\omega_m - \Omega/2)t + \beta_+ \sin(\omega_m + \Omega/2)t)} \quad (\text{A.26}) \\ &= \tilde{E}_0 e^{i\omega_c t} \left\{ \sum_{n=-\infty}^{\infty} J_n(\beta_-) e^{in(\omega_m - \Omega/2)t} \right\} \left\{ \sum_{n=-\infty}^{\infty} J_n(\beta_+) e^{in(\omega_m + \Omega/2)t} \right\} \quad (\text{A.27}) \end{aligned}$$

In going from the first equality to the second, we invoked the Jacobi-Anger expansion on each modulation frequency term separately. Now let us state several assumptions which limit the scope of this derivation, but at the benefit of making the mathematics easier and still modeling the experimental situation quite accurately. First, assume $\beta_- = \beta_+ \equiv \beta$. In the lab, the way we obtain two modulation frequencies is by mixing two synthesizer signals and obtaining equal powers in two frequencies driving an EOM, so this is a valid assumptions for the present work. Furthermore, we never drive the EOM particularly strongly (indeed, doing so would damage it), so we can assume we are in a $\beta \ll 1$ regime and drop from Equation A.27 all terms with $|n| > 1$.³

Multiplying the remaining terms in the sums of Equation A.27, we obtain:

$$\begin{aligned} \tilde{E}(t) &= \tilde{E}_0 [J_0^2(\beta) e^{i\omega_c t} - J_1^2(\beta) e^{i(\omega_c + \Omega)t} - J_1^2(\beta) e^{i(\omega_c - \Omega)t} \\ &\quad - J_0(\beta) J_1(\beta) e^{i(\omega_c - \omega_m - \Omega/2)t} - J_0(\beta) J_1(\beta) e^{i(\omega_c - \omega_m + \Omega/2)t} \\ &\quad + J_0(\beta) J_1(\beta) e^{i(\omega_c + \omega_m - \Omega/2)t} + J_0(\beta) J_1(\beta) e^{i(\omega_c + \omega_m + \Omega/2)t}] \quad (\text{A.28}) \end{aligned}$$

Examining the frequency components that appear in this expression, we see that we get a similar spectrum to the single-tone case, but now with spectral components split by Ω about the single-tone frequency components (e.g., a pair of components at $\omega_c + \omega_m \pm \Omega/2$). A sample spectrum, in the small β regime, is shown in Figure A.2. In this figure, the relative size of ω_m and Ω is not to scale. In fact, Ω is chosen to be much smaller than the typical absorption features we study. (See Chapter 3 for much more detail, but as a bit of foreshadowing we choose $\omega_m = 600$ MHz, $\Omega = 50$

³In Appendix C, some Mathematica code is shown which allows for easy computational extensions of this.

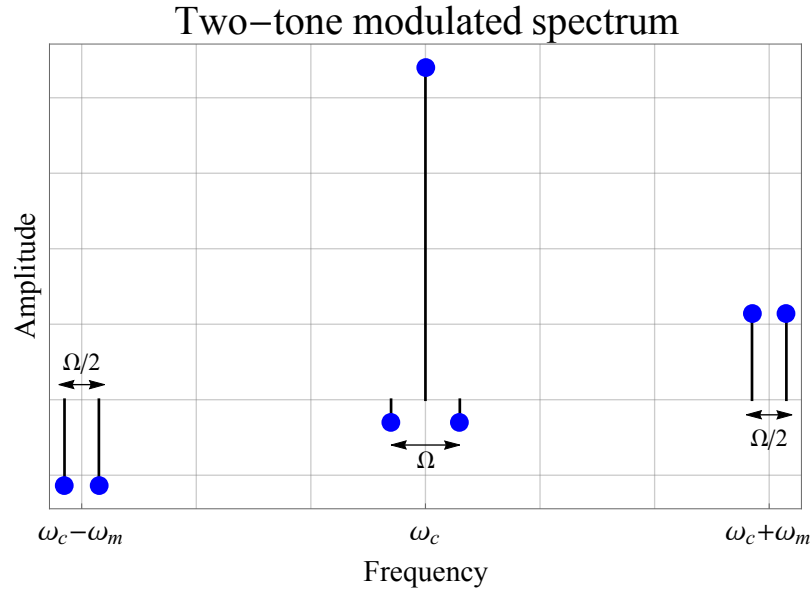


Figure A.2: For a particular choice of β , assumed to be small, the laser spectrum consists of pairs of peaks located near the frequencies $\omega_c \pm n\omega_m$. Small sidebands around the carrier frequency are produced by interference between the modulating frequencies. This spectrum is not to scale in the sense that $\Omega \ll \omega_m$, so the pairs of sidebands would really appear to be at nearly the exact same location on a properly scaled axis. Signs indicate relative phases between components.

kHz, and investigate transitions with widths of order 50 MHz.) So long as Ω is very small compared to these widths, both components of the closely spaced pairs will see approximately the same absorption. More precisely:

$$T(\omega_c + \omega_m - \Omega/2) \approx T(\omega_c + \omega_m + \Omega/2) \quad (\text{A.29})$$

$$T(\omega_c - \omega_m - \Omega/2) \approx T(\omega_c - \omega_m + \Omega/2) \quad (\text{A.30})$$

Hence, we may treat each of the closely spaced pairs of frequency sidebands as essentially identical. There are now only three frequency components between which we must distinguish: those at ω_c , $\omega_c + \omega_m$, and $\omega_c - \omega_m$. Just like in Equation A.18, we must append a frequency-dependent transmission coefficient to each term in order to simulate the interaction between the laser field and the atomic sample, keeping in mind the simplification implied by Equations A.29 and A.30.

To model the detection process, we must find the absolute value squared of $\tilde{E}(t)$, which is proportional the detected intensity we obtain a tremendously ugly mess of terms oscillating at a variety of frequencies. To deal with this, Mathematica arises as our savior. See Appendix C for code which allows for the easy derivation of the transmitted intensity. However, we only really care about one term in the intensity expression— consider what happens if we select only the terms oscillating at Ω , the

difference between the two modulation frequencies. Demodulating at that frequency, we get the intensity profile:

$$I_{\text{demod}} \propto 2T^2(\omega_c) - T^2(\omega_c - \omega_m) - T^2(\omega_c + \omega_m) \quad (\text{A.31})$$

This is the fundamental result of two-tone FM spectroscopy: the demodulated lineshape consists of an upward-going central peak at ω_c , with downward-going sidebands spaced at ω_m on either side. This is quite reminiscent of the single-tone case, although slightly more complicated than a simple comparison of relative absorption. A nice feature of the signal is that the sidebands are located at precisely ω_m away from the central peak, so long as the broadened atomic width is much less than the modulation frequency, so the signal is “self-calibrating.”

Appendix B

Three-Level System Derivations

In this Appendix, we fill in the details surrounding the three-level dynamics studied for this thesis. While this theoretical treatment is fundamentally new to the Majumder lab, the derivation of Equation 2.12 is a standard problem in quantum optics. We first present the details of the derivation of this Hamiltonian, and then derive the Doppler shift correction that was quoted in Equation 2.17.

B.1 Derivation of the Three-Level Hamiltonian

We set out to derive the three-level Hamiltonian quoted in Equation 2.12. Consider the three states shown in Figure 2.5, $|1\rangle$, $|2\rangle$, and $|3\rangle$ with energies E_1 , E_2 , and E_3 , respectively. With no interaction, these states are eigenstates of the “bare” atomic Hamiltonian, which can be written as

$$H_{\text{bare}} = \begin{pmatrix} E_1 & 0 & 0 \\ 0 & E_2 & 0 \\ 0 & 0 & E_3 \end{pmatrix} \quad (\text{B.1})$$

Two lasers are used to couple these states in a “ladder” (or “cascade”) configuration, meaning we choose the frequencies to be well-separated from one another, at $\omega_1 \approx (E_2 - E_1)/\hbar$ and $\omega_2 \approx (E_3 - E_2)/\hbar$. This (two) laser electric field is thus $\vec{\varepsilon}(t) = \vec{\varepsilon}_1 e^{i\omega_1 t} + \vec{\varepsilon}_2 e^{i\omega_2 t} + \text{c.c.}$ ¹ This leads to an interaction represented by a Hamiltonian whose matrix elements are $\langle j | (\hat{d} \cdot \vec{\varepsilon}) | k \rangle$, where \hat{d} is the electric dipole operator which connects two states.² Now, there ought not be any dipole coupling between an energy eigenstate and itself, so $\langle 1 | \hat{d} | 1 \rangle = \langle 2 | \hat{d} | 2 \rangle = \langle 3 | \hat{d} | 3 \rangle \equiv 0$. Meanwhile, any Hamiltonian must be Hermitian, so let us define $\langle 1 | \hat{d} | 2 \rangle \equiv d_{21}$ and $\langle 2 | \hat{d} | 3 \rangle \equiv d_{32}$, hence $\langle 2 | \hat{d} | 1 \rangle \equiv d_{21}^*$ and $\langle 3 | \hat{d} | 2 \rangle \equiv d_{32}^*$. States $|1\rangle$ and $|3\rangle$ are not coupled by an electric dipole operator (due to parity), else we would choose to drive that transition

¹The choice of a cosine-like field is arbitrary— besides, we want to think about steady-state behavior in which case the difference in phase between a sine and cosine can hardly matter.

²From now on, we assume the light is linearly polarized to simplify the dot product that appears in the matrix elements.

directly. So, we may treat the matrix elements between those two states as zero. This interaction is thus

$$H_{\text{int}} = \{\varepsilon_1 e^{i\omega_1 t} + \varepsilon_2 e^{i\omega_2 t} + \text{c.c.}\} \begin{pmatrix} 0 & d_{21} & 0 \\ d_{21}^* & 0 & d_{32} \\ 0 & d_{32}^* & 0 \end{pmatrix} \quad (\text{B.2})$$

And hence the full Hamiltonian, $H_{\text{full}} = H_{\text{bare}} + H_{\text{int}}$, is:

$$H_{\text{full}} = \begin{pmatrix} E_1 & 0 & 0 \\ 0 & E_2 & 0 \\ 0 & 0 & E_3 \end{pmatrix} + \{\varepsilon_1 e^{i\omega_1 t} + \varepsilon_2 e^{i\omega_2 t} + \text{c.c.}\} \begin{pmatrix} 0 & d_{21} & 0 \\ d_{21}^* & 0 & d_{32} \\ 0 & d_{32}^* & 0 \end{pmatrix} \quad (\text{B.3})$$

We now pull a standard trick in which we enter a “rotating frame” to endow all states with a time-dependent phase. This is achieved by finding a unitary transformation and new state which satisfy $|\psi\rangle = \hat{U}_0 |\phi\rangle$, where \hat{U}_0 is carefully chosen for later convenience. The new problem is to solve for the evolution of $|\phi\rangle$. We choose the following unitary operator:

$$\hat{U}_0 = \begin{pmatrix} 1 & 0 & 0 \\ 0 & e^{-i\omega_1 t} & 0 \\ 0 & 0 & e^{-i(\omega_1 + \omega_2)t} \end{pmatrix} \quad (\text{B.4})$$

The utility of this choice of unitary operator will be apparent soon. Intuitively, its action is to boost each eigenstate of H_{bare} by an amount corresponding to that state’s unperturbed energy separation from the ground state (in the sense of appending an time-dependent phase to each state). Now, write the time-dependent Schrodinger Equation for $|\phi\rangle$ as

$$i\hbar \left(\frac{d\hat{U}_0}{dt} |\phi\rangle + \hat{U}_0 \frac{d|\phi\rangle}{dt} \right) = H_{\text{full}} \hat{U}_0 |\phi\rangle \quad (\text{B.5})$$

Note the use of the chain rule on the state, since both \hat{U}_0 and $|\phi\rangle$ depend on t . Multiplying through by \hat{U}_0^\dagger , rearranging terms, and noting that \hat{U}_0 and H_{bare} commute, we get:

$$i\hbar \frac{d|\phi\rangle}{dt} = \left[H_{\text{bare}} + \hat{U}_0^\dagger H_{\text{int}} \hat{U}_0 - i\hbar \hat{U}_0^\dagger \frac{d\hat{U}_0}{dt} \right] |\phi\rangle \quad (\text{B.6})$$

Clearly, identifying the term in square brackets itself as a Hamiltonian, which we define as H_{RF} , yields a Schrodinger-like equation in the rotating frame. It is straightforward (though tedious) to calculate the matrix forms of the three terms that comprise H_{RF} , and the operator turns out to be:

$$\begin{aligned}
H_{\text{RF}} = & \begin{pmatrix} E_1 & 0 & 0 \\ 0 & E_2 - \hbar\omega_1 & 0 \\ 0 & 0 & E_3 - \hbar(\omega_1 + \omega_2) \end{pmatrix} \\
& + \{ \varepsilon_1 e^{i\omega_1 t} + \varepsilon_2 e^{i\omega_2 t} + \text{c.c.} \} \begin{pmatrix} 0 & d_{21} e^{-i\omega_1 t} & 0 \\ d_{21}^* e^{i\omega_1 t} & 0 & d_{32} e^{-i\omega_2 t} \\ 0 & d_{32}^* e^{i\omega_2 t} & 0 \end{pmatrix}
\end{aligned} \tag{B.7}$$

Now all the time-dependence is in the off-diagonal terms, but something interesting happens if we explicitly write that dependence out. There are terms at $2\omega_1$, $2\omega_2$, $\omega_1 + \omega_2$, and $\omega_1 - \omega_2$, as well as DC terms. In our case, the laser frequencies are far detuned from one another, so all the non-DC terms are large enough that they quickly time-average to zero. Dropping these quickly oscillating terms is called the “rotating wave approximation.” In that approximation, the Hamiltonian has a fairly simple form:

$$H_{\text{RWA}} = \begin{pmatrix} E_1 & \varepsilon_1 d_{21} & 0 \\ \varepsilon_1 d_{21} & E_2 - \hbar\omega_1 & \varepsilon_2 d_{32} \\ 0 & \varepsilon_2 d_{32} & E_3 - \hbar(\omega_1 + \omega_2) \end{pmatrix} \tag{B.8}$$

We can clean things up a bit. Define $\Omega_1 = \varepsilon_1 d_{21}/\hbar$ and $\Omega_2 = \varepsilon_2 d_{32}/\hbar$ as the Rabi frequencies of the first and second transitions, respectively. Also introduce δ 's to represent Stark shifts in the individual levels: let $E_j = E_j^{(0)} - \hbar\delta_j$, for $j = 1, 2, 3$. Note especially that each $\delta \propto \mathcal{E}^2$, so when the field is off these δ 's are all zero, whereas when the field is on they are all quadratic in the field. Then:

$$H_{\text{RWA}} = \begin{pmatrix} E_1^{(0)} - \delta_1 & \Omega_1 & 0 \\ \Omega_1 & E_2^{(0)} - \delta_2 - \hbar\omega_1 & \Omega_2 \\ 0 & \Omega_2 & E_3^{(0)} - \delta_3 - \hbar(\omega_1 + \omega_2) \end{pmatrix} \tag{B.9}$$

Now, since the zero of energy is arbitrary, we can subtract $E_1^{(0)} - \delta_1$ along the diagonal to get:

$$H_{\text{RWA}} = \begin{pmatrix} 0 & \Omega_1 & 0 \\ \Omega_1 & E_2^{(0)} - E_1^{(0)} - (\delta_2 - \delta_1) - \hbar\omega_1 & \Omega_2 \\ 0 & \Omega_2 & E_3^{(0)} - E_1^{(0)} - (\delta_3 - \delta_1) - \hbar(\omega_1 + \omega_2) \end{pmatrix} \tag{B.10}$$

Define the detunings *from field-free* resonance as $\Delta_1 = E_2^{(0)} - E_1^{(0)} - \hbar\omega_1$ and $\Delta_2 = E_3^{(0)} - E_2^{(0)} - \hbar\omega_2$. Then:

$$H_{\text{RWA}} = \begin{pmatrix} 0 & \Omega_1 & 0 \\ \Omega_1 & \Delta_1 - (\delta_2 - \delta_1) & \Omega_2 \\ 0 & \Omega_2 & \Delta_2 + \Delta_1 - (\delta_3 - \delta_1) \end{pmatrix} \tag{B.11}$$

This is the general form of the Hamiltonian we must study, and special cases are discussed in Sections 2.4.2 and 2.4.3.

B.2 Stark Shift Correction Due to Doppler Shift

This derivation is only relevant if we conduct the experiment like in Section 2.4.2, where the blue laser is not shifted to stay resonant with the atomic beam. In that case, we stabilize the blue laser to a sample of atoms in a field-free region and do nothing to shift the part of the beam going to the ABU. This means that when we apply the electric field to the atomic beam, the first-step transition is slightly off resonance (because in the atomic beam, *all* energy levels shift). In the atomic beam, we thus excite atoms whose motion along the laser beam causes a Doppler shift bringing them *back* into resonance with the blue beam. Because only these atoms are available for excitation to the $6P_{1/2}$ state, that transition will again take place at a Doppler-shifted frequency. We must account for this in order to measure the proper Stark shift value in our experiment.

Following [7], and looking at Figure 2.4 as necessary, define $|\Delta_{21}|$ and $|\Delta_{32}|$ to be the *magnitudes* of the Stark shifts in the lower ($5P_{1/2} \rightarrow 6S_{1/2}$) and upper ($6S_{1/2} \rightarrow 6P_{1/2}$) transitions, respectively. (Note that $\Delta_{32} \gg \Delta_{21}$.) Similarly, define the field-free resonance frequencies as f_{21}^0 and f_{32}^0 , and the field-on frequencies as f'_{21} and f'_{32} . Atoms in a region of high electric field will have their energy levels shifted down in frequency (by $|\Delta_{21}|$), but the first-step laser is locked at the field-free value. Hence, we excite atoms whose Doppler shift brings them back onto resonance—the velocity class excited is determined by the condition

$$f'_{21} = f_{21}^0 = \left(1 + \frac{v}{c}\right) (f_{21}^0 - |\Delta_{21}|) \quad (\text{B.12})$$

Similarly, the second-step transition will be observed at

$$f'_{32} = \left(1 + \frac{v}{c}\right) (f_{32}^0 - |\Delta_{32}|) \quad (\text{B.13})$$

where we accounted for the Stark shift by subtracting off $|\Delta_{32}|$. Solving Equation B.12 for $(1 + v/c)$ and substituting it into Equation B.13, we obtain the condition

$$f'_{32} = \frac{f_{21}^0}{f_{21}^0 - |\Delta_{21}|} (f_{32}^0 - |\Delta_{32}|) \approx \left(1 + \frac{|\Delta_{21}|}{f_{21}^0}\right) (f_{32}^0 - |\Delta_{32}|) \quad (\text{B.14})$$

where the approximation is justified since $\Delta_{21} \ll f_{21}^0$. Expanding out the product in Equation B.14 and keeping only through first order in Δ/f yields the final relationship

$$f'_{32} = f_{32}^0 - |\Delta_{32}| + |\Delta_{21}| \frac{f_{32}^0}{f_{21}^0} \quad (\text{B.15})$$

This determines the actual Stark shift, Δ_{32} , in terms of the observed shift of a resonance, $f'_{32} - f_{32}^0$. Because f_{32}^0 and f_{21}^0 are known very precisely, and Δ_{21} was determined to high-precision in [15], a precise determination of Δ_{32} is possible.

Appendix C

Mathematica Simulations

In this appendix, we present Mathematica code referenced within the thesis. First, a short Mathematica program that generates two-tone FM lineshapes is shown; second, a program that helps study the theory of three-level systems in an external electric field is presented.

C.1 Two-Tone FM Lineshape

From a practical standpoint, the most important result of Section 2.2.2 is the two-tone FM lineshape used to detect the spectra collected from the atomic beam. This includes various approximations that will be outlined below. However, over the course of this past year we turned our attention to how changing parameters of the FM technique would affect a collected spectrum. The mathematics quickly becomes intractable (or at the very least aggravating) to work out by hand. We therefore developed a simple Mathematica program that allows for the calculation of two-tone FM lineshapes in essentially full generality.

Clearly, a lot of algebraic gymnastics are necessary when working with the expressions that enter into the two-tone FM lineshape derivation, especially if one wishes to relax the various assumptions we made therein. Mathematica is an ideal tool to accelerate the simple, though tedious, mathematical manipulations. Here we present a program to allow the quick derivation of more general FM lineshapes.

We begin the derivation *after* having applied the Jacobi-Anger identity which expresses the electric field as an infinite sum over frequency sidebands— that is, we start with Equation A.27. Figure C.1 shows the code used to simulate the electric field of the modulated laser. In order to more accurately represent the reality of our experiment, we also take into account the fact that the mixing circuit used to produce the $\omega_m \pm \frac{\Omega}{2}$ driving our EOM also produces a small amount of power at $\omega_m \pm \frac{3\Omega}{2}$, and all other odd-half-integer multiples of Ω away from the center modulation frequency. These “extra” sidebands are exponentially suppressed, and so we only include the first of them. However, in this demonstration of the code that capability is commented out.

```

Clear[ $\omega$ m,  $\Omega$ ];
 $\beta$ 1 = .5;
 $\beta$ 2 = 0;
For[Degp = 1, (Abs[BesselJ[Degp,  $\beta$ 1]] > .25 || Abs[BesselJ[Degp + 1,  $\beta$ 1]]), Degp++];
For[Degm = 1, (Abs[BesselJ[Degm,  $\beta$ 2]] > .05 || Abs[BesselJ[Degm + 1,  $\beta$ 2]]), Degm++];
E1[t_] := Chop[Expand[
  TrigToExp[
    TrigExpand[
      ExpToTrig[
        Expand[
          (Sum[BesselJ[n,  $\beta$ 1] Exp[n I ( $\omega$ m +  $\Omega$ /2) t], {n, -Degp, Degp}])
          (Sum[BesselJ[m,  $\beta$ 1] Exp[m I ( $\omega$ m -  $\Omega$ /2) t], {m, -Degp, Degp}])
          (* (Sum[BesselJ[n1,  $\beta$ 2] Exp[n1 I ( $\omega$ m + 3 $\Omega$ /2) t], {n1, -Degm, Degm}])
          (Sum[BesselJ[m1,  $\beta$ 2] Exp[m1 I ( $\omega$ m - 3 $\Omega$ /2) t], {m1, -Degm, Degm}]) *)
        ]]]]]]]

```

Figure C.1: This portion of code generates the electric field of the modulated laser beam. Commented out is a portion of the code that allows us to include higher order sidebands.

The user must input values of β_1 and β_2 which define the modulation depth of first and second order sidebands. Then, the program calculates the number of terms to include in each sum, using the criteria that terms with coefficients above a certain minimum size will be retained. Finally, the program calculates the product of sums which constitutes the electric field, including all appreciably sized terms. A hideous combination of commands to simplify the expression is required, but at its heart this portion of code is really just multiplying many terms together.

Next, the program calculates the spectrum of the generated laser field. This is shown in Figure C.2. It does so by selecting from the simulated laser electric field terms at various frequency values. Choosing suitable parameter values, it plots the spectrum and we see what looks like the expected set of frequency components along with their respective phases, as shown in Figure C.3.

After obtaining the spectrum, we must simulate the frequency-dependent absorption caused by the atom-laser interaction (see Figure C.4). This is done by appending the appropriate transmission factor to each frequency component in the laser spectrum. We turn the spectrum back into the laser field by summing all terms in the spectrum, weighted by their transmission factor. Finally, the absolute value squared of the electric field is calculated in order to simulate the intensity—recall that we can only detect intensities. Note that, for reasons that are poorly understood by the author, Mathematica is happiest if we take the complex conjugate “by hand.” Hence, we manually replace i by $-i$ (and $-i$ by i) in that part of the code.

Here is where the true power of Mathematica shines: even retaining only a few terms in the expression for the laser intensity would fill nearly a printed page. If we wish to relax low-modulation depth assumptions, tens of pages would be filled to print out the expression for laser intensity!

```

spectrum = {};
Do[Do[
  a = Select[E1[t], MemberQ[#, Exp[i I t ωm + j I t Ω / 2]] &];
  b = N[a /. t → 0];
  If[b ≠ 0, AppendTo[spectrum, {i ωm + j Ω / 2, a}], 0],
  {i, -4 Degp, 4 Degp}], {j, -4 Degm, 4 Degm}];
AppendTo[spectrum, {0, Select[E1[t], (FreeQ[#, ωm] && FreeQ[#, Ω]) &]}];
Sort[spectrum] /. {ωm → 600, Ω → 10, t → 0} // Chop
ListPlot[spectrum /. {ωm → 600, Ω → 75, t → 0}, PlotRange → All,
  PlotStyle → {PointSize[.012], Black}, ImageSize → 600,
  Filling → Axis, FillingStyle → Directive[Thickness[.004], Black]]

```

Figure C.2: This portion of the code collects terms according to the argument of the complex exponential factor—that is, it collects terms according to their frequency value. This allows us to generate the laser spectrum from the simulation.

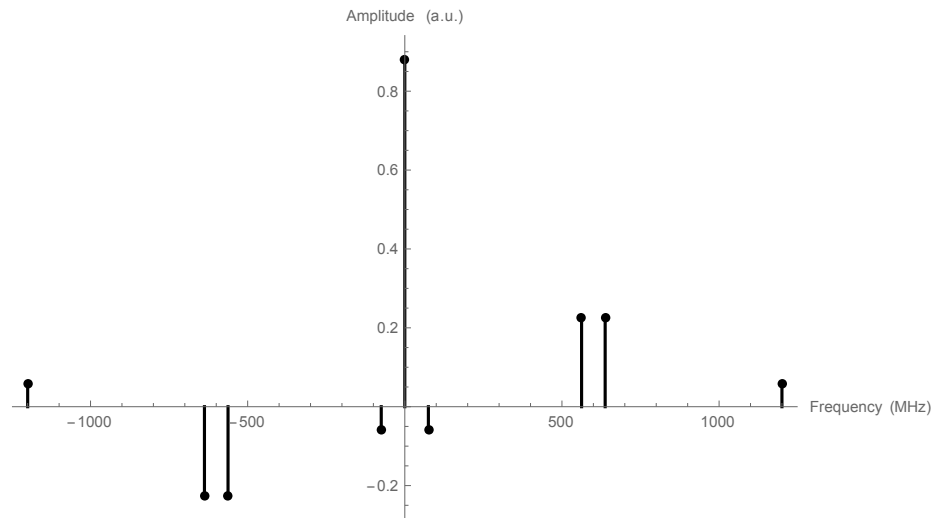


Figure C.3: A sample plot of the simulated laser spectrum. It checks with the expected form.

With the intensity, we have nearly completed the Mathematica simulation. All that remains is to mimic the action of a lock-in amplifier. In other words, we want to pick out only those terms that oscillate at Ω (the difference between the two frequencies with which we drove the EOM in the first place). See Figure C.5. A clever Mathematica trick is used to achieve this: we sort the intensity according to the arguments of the complex exponentials multiplying each term, find the coefficient of the factor $e^{i\Omega t}$ (and of $e^{-i\Omega t}$ since Mathematica thinks of i and $-i$ as distinct entities), and then simply set t equal to zero to remove time dependence. We are left with an expression for the demodulated intensity which is surprisingly simple, and equal to the expected lineshape.

```

Clear[T];
E2 := 0;
Do[Do[
  E2 += T[laser + i ωm + j Ω/2] (Select[E1[t], (MemberQ[#, Exp[i I t ωm + j I t Ω/2]]) &]),
  {i, -2 Degp, 2 Degp}],
 {j, -2 Degm, 2 Degm}];
E2 += T[laser] (Select[E1[t], (FreeQ[#, ωm] && FreeQ[#, Ω]) &]);
Int = Chop[TrigToExp[TrigExpand[ExpToTrig[ExpandAll[
  (E2 /. {I → -I, -I → I})] ExpandAll[E2]]]]];

```

Figure C.4: This portion of code calculates the transmitted electric field and the corresponding intensity.

```

Demod[laser_] := Collect[
  Coefficient[Collect[Int, E^_], Exp[I Ω t]]
  + Coefficient[Collect[Int, E^_], Exp[-I Ω t]], E^_ /. {E^_ → 0}

```

Figure C.5: This portion of the code simulates the effect of a lock-in amplifier on the intensity calculated above. We pick out terms that oscillated at frequency Ω . We are left with the proper cross terms of transmission coefficients at various frequencies. Though the coefficients of these terms are numeric, they do indeed match the appropriate values of Bessel functions that appear in the analytic lineshape derivation.

C.2 Analysis of Three-Level Hamiltonian

Numerical Diagonalization and Fractional Difference Calculations

In Section 2.4, it was necessary to solve for the eigenvalues and eigenvectors of a 3×3 Hamiltonian. We present here the Mathematica code which does so. The code, in Figure C.6, calculates the eigenvalues and eigenvectors of the RWA Hamiltonian, iterating over choices of detuning Δ . Then it computes the probability to be excited to the third state, $\langle P_3 \rangle$, using Equation 2.15. It computes the location of the peak of that quantity, and then computes a fractional difference between the peak location and the location of either $\delta_3 - \delta_2$ or $\delta_3 - \delta_1$, depending on whether or not we have chosen to construct the Hamiltonian with the blue laser always resonant with the lower transition.

Analytic Lineshape Calculation

The code in Figure C.7 is due to Professor Fred Strauch. It walks through the derivation of Equation 2.19.

```

scaleTable = {};
Do[
  Ez = Ez1; (* External electric field in kV/cm *)
  Ω1 = 9; (* Assumed Rabi frequency for blue laser *)
  Ω2 = 9; (* Assumed Rabi frequency for IR laser *)
  δ21 = .122 Ez^2; (* Using value of ks from Nathan Schine *)
  δ31 = .97 Ez^2; (* Assuming ks=.97 for upper state; Does not contain Doppler-shift correction *)
  Δ1 = δ21; (* Detuning in first transition-- set to 0 if no laser adjustment, set to δ21 to keep on resonance *)
  Hrwa[Δ_] :=
    {{0, Ω1, 0},
     {Ω1, Δ1 - δ21, Ω2}, (*Adding in .122Ez^2 to the diagonal assumes the lock point is following the Stark shift*)
     {0, Ω2, -δ31 + Δ + Δ1}}; (* Rotating wave Hamiltonian, Δ=variable detuning *)

  (* Now step through Δ values, numerically calculate eigenvalues and eigenvectors,
  calculate the probability to end up in the third state. Make an interpolating
  function of the probability to end up in the 3rd state. *)
  probCompile = {};
  Do[
    {vals, vecs} = Eigensystem[Hrwa[Δ]];
    normvecs = Table[vecs[[i]] / Sqrt[Conjugate[vecs[[i]]].vecs[[i]]], {i, 1, Length[vecs]}] // Chop;
    prob3 = Sum[Abs[{0, 0, 1}.normvecs[[i]] normvecs[[i]].{1, 0, 0}]^2, {i, 1, 3}];
    AppendTo[probCompile, {Δ, prob3}],
    {Δ, -25, 300, .5}];
  probFull = Interpolation[probCompile];
  simMax = x /. NMaximize[{probFull[x], (δ31) - 25 ≤ x ≤ (δ31) + 25}, x][[2]];
  testMax = δ31 - δ21; (* Testing to compare to Shift if what we measure really is δ3-δ2 *)
  scale = (simMax - testMax) / testMax;
  AppendTo[scaleTable, {Ez, scale}],
  {Ez1, 1, 15}];
ListPlot[scaleTable, PlotStyle → Red, AxesLabel → {"Ez", "Fractional Diff"}, ImageSize → 500, LabelStyle → {Black, Medium}]

```

Figure C.6: This code allows us to generate numerical comparisons between the three-level Hamiltonian lineshape $\langle P_3 \rangle$ to the “ideal” peak location if the Stark shift were truly the difference between two states.

We first write the eigenvectors of the Hamiltonian in the form

$$v_\lambda = \frac{1}{(\Omega_1 \Omega_2)^2 + \lambda^2 \Omega_2^2 + (\lambda^2 - \Omega_1^2)^2}^{1/2} \{ \Omega_1 \Omega_2, \Omega_2 \lambda, (\lambda^2 - \Omega_1^2) \},$$

where λ are the eigenvalues of the RWA Hamiltonian.

This yields a the time-averaged transition probability of

$$p_{1 \rightarrow 3} = \sum_{j=1}^3 | \langle 1 | v_{\lambda_j} \rangle \langle v_{\lambda_j} | 3 \rangle |^2$$

$$p_{1 \rightarrow 3} = \sum_{j=1}^3 \frac{(\Omega_1 \Omega_2)^2 (\lambda_j^2 - \Omega_1^2)^2}{(\Omega_1 \Omega_2)^2 + \lambda_j^2 \Omega_2^2 + (\lambda_j^2 - \Omega_1^2)^2}.$$

We then form a common denominator for this probability, and Taylor expand the numerator and denominator as a function of the detuning.

This is guaranteed to terminate at some order because the eigenvalues occur symmetrically, in which case one repeatedly use the relations

$$\lambda_1 + \lambda_2 + \lambda_3 = x$$

$$\lambda_1 \lambda_2 + \lambda_1 \lambda_3 + \lambda_2 \lambda_3 = -(\Omega_1^2 + \Omega_2^2)$$

$$\lambda_1 \lambda_2 \lambda_3 = -\Omega_1^2 x$$

to reduce the expression in terms of x , Ω_1 , and Ω_2 . The final result is

$$p_{1 \rightarrow 3} = \frac{2 (\Omega_1 \Omega_2)^2 (x^2 + 3 (\Omega_1^2 + \Omega_2^2))}{4 x^4 \Omega_1^2 + 4 (\Omega_1^2 + \Omega_2^2)^3 + x^2 (-8 \Omega_1^4 + 20 \Omega_1^2 \Omega_2^2 + \Omega_2^4)}.$$

The minus sign in the denominator leads to the split peak if $\Omega_1 > 0.7 \Omega_2$ (or so).

First form the Hamiltonian and check the eigenvectors.

$H = \{ \{0, \Omega_1, 0\}, \{ \Omega_1, 0, \Omega_2 \}, \{0, \Omega_2, x\} \};$

$H \cdot \{a, b, c\} - \lambda \{a, b, c\}$

$\{-a \lambda + b \Omega_1, -b \lambda + a \Omega_1 + c \Omega_2, c x - c \lambda + b \Omega_2\}$

Solve $\{-a \lambda + b \Omega_1 = 0, -b \lambda + a \Omega_1 + c \Omega_2 = 0\}, \{b, c\}$

$\{ \{ b \rightarrow \frac{a \lambda}{\Omega_1}, c \rightarrow \frac{a (\lambda^2 - \Omega_1^2)}{\Omega_1 \Omega_2} \} \}$

(* Let's let a = $\Omega_1 \Omega_2$ *)

$v[\lambda_] = \frac{1}{\text{Sqrt}[(\Omega_1 \Omega_2)^2 + \lambda^2 \Omega_2^2 + (\lambda^2 - \Omega_1^2)^2]} \{ \Omega_1 \Omega_2, \lambda \Omega_2, (\lambda^2 - \Omega_1^2) \};$

FullSimplify $[H \cdot v[\lambda] - \lambda v[\lambda]]$

$\{0, 0, \frac{(x-\lambda)(\lambda-\Omega_1)(\lambda+\Omega_1)+\lambda\Omega_2^2}{\sqrt{(\lambda^2-\Omega_1^2)^2+(\lambda^2+\Omega_1^2)\Omega_2^2}}\}$

$\{0, 0, \frac{(x-\lambda)(\lambda-\Omega_1)(\lambda+\Omega_1)+\lambda\Omega_2^2}{\sqrt{(\lambda^2-\Omega_1^2)^2+(\lambda^2+\Omega_1^2)\Omega_2^2}}\}$

Note that the last term vanishes by the eigenvalue equation for λ :

Expand $[(x-\lambda)(\lambda-\Omega_1)(\lambda+\Omega_1)+\lambda\Omega_2^2]$

$x \lambda^2 - \lambda^3 - x \Omega_1^2 + \lambda \Omega_1^2 + \lambda \Omega_2^2$

Det $[H - \lambda \text{IdentityMatrix}[3]]$

$x \lambda^2 - \lambda^3 - x \Omega_1^2 + \lambda \Omega_1^2 + \lambda \Omega_2^2$

Now form the numerator and denominator of $p_{1 \rightarrow 3}$:

$\text{num} = \Omega_1^2 \Omega_2^2 (\lambda^2 - \Omega_1^2)^2 ((\Omega_1^2 \Omega_2^2 + \lambda^2 \Omega_2^2 + (\lambda^2 - \Omega_1^2)^2)$

$\times (\Omega_1^2 \Omega_2^2 + \lambda^2 \Omega_2^2 + (\lambda^2 - \Omega_1^2)^2))^2 + \Omega_1^2 \Omega_2^2 (\lambda^2 - \Omega_1^2)^2$

$\times ((\Omega_1^2 \Omega_2^2 + \lambda^2 \Omega_2^2 + (\lambda^2 - \Omega_1^2)^2) (\Omega_1^2 \Omega_2^2 + \lambda^2 \Omega_2^2 + (\lambda^2 - \Omega_1^2)^2))^2$

$+ \Omega_1^2 \Omega_2^2 (\lambda^2 - \Omega_1^2)^2 ((\Omega_1^2 \Omega_2^2 + \lambda^2 \Omega_2^2 + (\lambda^2 - \Omega_1^2)^2) (\Omega_1^2 \Omega_2^2 + \lambda^2 \Omega_2^2 + (\lambda^2 - \Omega_1^2)^2))^2$;

$\text{denom} = ((\Omega_1^2 \Omega_2^2 + \lambda^2 \Omega_2^2 + (\lambda^2 - \Omega_1^2)^2) (\Omega_1^2 \Omega_2^2 + \lambda^2 \Omega_2^2 + (\lambda^2 - \Omega_1^2)^2) (\Omega_1^2 \Omega_2^2 + \lambda^2 \Omega_2^2 + (\lambda^2 - \Omega_1^2)^2))^2$;

(* Ω_1 and Ω_2 are the Rabi frequencies, x is equal to the combined Stark shift minus the laser frequency shift *)

Calculate the eigenvalues and expand them as a function of x :

$\{vals, vecs\} = \text{Eigensystem}[H, \text{Cubics} \rightarrow \text{True}];$

$\lambda 1x = \text{Normal}[\text{FullSimplify}[\text{Series}[vals[[1]], \{x, 0, 10\}], \text{Assumptions} \rightarrow \{\Omega_1 > 0, \Omega_2 > 0\}]]];$

$\lambda 2x = \text{Normal}[\text{FullSimplify}[\text{Series}[vals[[2]], \{x, 0, 10\}], \text{Assumptions} \rightarrow \{\Omega_1 > 0, \Omega_2 > 0\}]]];$

$\lambda 3x = \text{Normal}[\text{FullSimplify}[\text{Series}[vals[[3]], \{x, 0, 10\}], \text{Assumptions} \rightarrow \{\Omega_1 > 0, \Omega_2 > 0\}]]];$

$\lambda 1x;$

Do the same thing for the numerator and denominator. Note that their expansion only has even powers of x

and only goes up to x^6 and x^8 for the numerator and denominator, respectively.

$\text{num} = \text{num} /. \{\lambda 1 \rightarrow \lambda 1x, \lambda 2 \rightarrow \lambda 2x, \lambda 3 \rightarrow \lambda 3x\};$

num

$\text{num} = \text{Normal}[\text{Simplify}[\text{Series}[\text{num}, \{x, 0, 10\}], \text{Assumptions} \rightarrow \{\Omega_1 > 0, \Omega_2 > 0\}]]]$

$8 x^6 \Omega_1^8 \Omega_2^{10} + 24 \Omega_1^6 \Omega_2^{10} (\Omega_1^2 + \Omega_2^2)^4 + 2 x^4 \Omega_1^6 \Omega_2^{10} (4 \Omega_1^4 + 32 \Omega_1^2 \Omega_2^2 + \Omega_2^4) + 2 x^2 \Omega_1^6 \Omega_2^{10} (-20 \Omega_1^6 + 48 \Omega_1^4 \Omega_2^2 + 75 \Omega_1^2 \Omega_2^4 + 7 \Omega_2^6)$

$\text{denom} = \text{Normal}[\text{Simplify}[\text{Series}[\text{denom} /. \{\lambda 1 \rightarrow \lambda 1x, \lambda 2 \rightarrow \lambda 2x, \lambda 3 \rightarrow \lambda 3x\}, \{x, 0, 10\}], \text{Assumptions} \rightarrow \{\Omega_1 > 0, \Omega_2 > 0\}]]];$

$\text{denom}x$

$16 x^8 \Omega_1^8 \Omega_2^8 + 16 \Omega_1^4 \Omega_2^8 (\Omega_1^2 + \Omega_2^2)^6 - 8 x^2 \Omega_1^4 \Omega_2^8 (\Omega_1^2 + \Omega_2^2)^3 (8 \Omega_1^4 - 20 \Omega_1^2 \Omega_2^2 - \Omega_2^4)$

$+ 8 x^6 \Omega_1^6 \Omega_2^8 (-8 \Omega_1^4 + 20 \Omega_1^2 \Omega_2^2 + \Omega_2^4) + x^4 \Omega_1^4 \Omega_2^8 (96 \Omega_1^8 - 224 \Omega_1^6 \Omega_2^2 + 480 \Omega_1^4 \Omega_2^4 + 72 \Omega_1^2 \Omega_2^6 + \Omega_2^8)$

Finally, we can form the transition probability and simplify!

$\text{prob13} = \text{num}x / \text{denom}x$

$(8 x^6 \Omega_1^8 \Omega_2^{10} + 24 \Omega_1^6 \Omega_2^{10} (\Omega_1^2 + \Omega_2^2)^4 + 2 x^4 \Omega_1^6 \Omega_2^{10} (4 \Omega_1^4 + 32 \Omega_1^2 \Omega_2^2 + \Omega_2^4) + 2 x^2 \Omega_1^6 \Omega_2^{10} (-20 \Omega_1^6 + 48 \Omega_1^4 \Omega_2^2 + 75 \Omega_1^2 \Omega_2^4 + 7 \Omega_2^6))$

$/ (16 x^8 \Omega_1^8 \Omega_2^8 + 16 \Omega_1^4 \Omega_2^8 (\Omega_1^2 + \Omega_2^2)^6 - 8 x^2 \Omega_1^4 \Omega_2^8 (\Omega_1^2 + \Omega_2^2)^3 (8 \Omega_1^4 - 20 \Omega_1^2 \Omega_2^2 - \Omega_2^4) +$

$8 x^6 \Omega_1^6 \Omega_2^8 (-8 \Omega_1^4 + 20 \Omega_1^2 \Omega_2^2 + \Omega_2^4) + x^4 \Omega_1^4 \Omega_2^8 (96 \Omega_1^8 - 224 \Omega_1^6 \Omega_2^2 + 480 \Omega_1^4 \Omega_2^4 + 72 \Omega_1^2 \Omega_2^6 + \Omega_2^8))$

Simplify $[\text{prob13}]$

$\frac{2 \Omega_1^2 \Omega_2^2 (x^2 + 3 (\Omega_1^2 + \Omega_2^2))}{4 x^4 \Omega_1^2 + 4 (\Omega_1^2 + \Omega_2^2)^3 + x^2 (-8 \Omega_1^4 + 20 \Omega_1^2 \Omega_2^2 + \Omega_2^4)}$

Figure C.7: This code walks through the analytic calculation of the lineshape $\langle P_3 \rangle$.

Appendix D

Data Analysis MATLAB Code

Here, we fill in details of the data analysis procedure (presented formally in Chapter 4) by explaining the guts of the code used to conduct the analysis. This analysis is conducted almost exclusively in MATLAB, although Kaleidagraph can be used to perform simple fits to data that has already been processed within MATLAB. Accordingly, this appendix is organized so as to follow the logical flow of the suite of MATLAB analysis code we have developed over the course of this year. (Much of this code was based on analysis programs written by former thesis students and post-docs—special thanks are owed to Gabby Vukasin '14, Nathan Schine '13, David Kealhofer '13, and Dr. Gambhir Ranjit.) Readers who wish to see previous iterations of analysis code used in the Majumder lab are encouraged to consult to Appendix A in [13] as an example. All of the files references here can be found on the Majumder lab fileserver in the directory `Z:\Ben\MATLAB\`.

The LabView program controlling data acquisition saves the data sets as follows. It generates a folder `Z:\In_Data\DayOfWeek,MonthDay,Year\`. (DayOfWeek is a three letter code corresponding to the day of data collection; MonthDay is the three letter code corresponding to the month and two digits corresponding to the numerical day; Year is a four digit version of the year.) All the files from a given trial are saved within this folder in subfolders corresponding to each HV setting recorded, and subsubfolders separating out upscans and downscans. Finally, each individual folder is a text file labeled by the scheme `n1trialn2.txt`. `n1` is the scan number, and `n2` is either 0 or 1—0 if the HV was off and 1 if the HV was on. Even `n1` values correspond to HV off-on sets, and odd `n1` values correspond to HV on-off sets. Hence, there are two files for each `n1`, since data is collected in HV-on and HV-off pairs.

D.1 IndiumFitOverlap.m

This is the master program, the one which calls all subprograms used in the analysis. It controls looping through the various data sets to be analyzed, which requires the user input two values: `PName1` and `PName2`. These two inputs define the folder (through the HV value) and the subfolder (upscan or downscan) to be analyzed.

It then defines a variable `counter` which will tell the user which file is being analyzed as the code runs, and an array `dataArray` which will be filled up as the analysis proceeds.

The rest of the program consists of a loops which run through the data contained within the folder specified by the `PName` values. The loops run over two counters: `n1`, which picks out the prefix number of each file to be analyzed (it must be set to run from 0 to $N - 1$, where N is the maximum prefix number), and `n2`, which runs of 0 and 1 and picks out either an HV-off (`n2=0`) or HV-on (`n2=1`) data set. Looping over these two counters, many subprograms are called to carry out the analysis.

D.1.1 `getdataIndium.m`

The first subprogram called is responsible for data import. It defines the file to be imported, by concatenating `PName` and `FName`, which were defined in the outer loop. This file location is the location of a specific `.txt` file. It opens the file, imports it, and generates an array called `data` which consists of five columns (the data point number, PZT ramp voltage, Fabry-Perot transmission signal, vapor cell hyperfine reference signal, and atomic beam two-tone FM signal). Finally, with the data imported, it closes the file in its stored location.

D.1.2 `downsampleAndNormalizeIndium2.m`

This program separates the array “data,” which was imported above, into separate arrays. It defines one single-column array for each column in `data`. `x_Raw` is the PZT ramp voltage, `fp_Raw` is the raw Fabry-Perot signal, and so on. Next, it excludes some data in case the computer recorded points outside of purely up- or down-scan. It defines `x_max` and `x_min` as the points corresponding to the minimum and maximum of the voltage ramp, respectively, and then reverses the order of the data points in every vector if `x_min > x_max` (i.e., in the case of a downscan). This ensures that all downscans are recorded in reverse point order, so that the data increases in frequency when plotted in order. We want all data sets to be increasing in frequency so that, for instance, the order of hyperfine peaks is always $F = 4$ before $F = 5$.

With the points in the proper order, we define a normalized point number axis according to Equation 4.1. We downsample the data by some factor to ensures that all points are statistically independent (in case we over-sampled during data collection). We are left with three vectors containing data points, and a corresponding x -axis for each: `x_fp_DS` as the Fabry-Perot’s downsampled x -axis, `fp_DS` as the downsampled Fabry-Perot data, and similarly for the vapor cell hyperfine reference as well as the atomic beam two-tone FM data. Finally, the program plots all three of these signals in an image like Figure 4.6.

D.1.3 FabryPerotFittingIndium.m

The next program actually has a few different versions, all of which start with the name `FabryPerotFittingIndium`. They all serve the purpose of fitting the Fabry-Perot signal, but each does so in a slightly different way, as specified by an underscored suffix in the file name.

FabryPerotFittingIndium.m

This fits the Fabry-Perot data to a sum of Lorentzians, the number of Lorentzians depending on the number of peaks found by the subprogram `sympeaksIndium`. Once `sympeaksIndium` has looked for peaks, given minimum peak heights and the option to perform a “running average” to smooth out jagged features, it defines a range over which to fit Lorentzians—it won’t do so too close to the edges of the scan, for instance. Depending on the number of peaks found, it then constructs a vector called `FPoints`, which contains the peak locations in order. This vector will be used to linearize the frequency axis later. If the fit is very poor, the program is called again to try once more.

FabryPerotFittingIndium_Airy.m

Rather than fitting the Fabry-Perot scan to a sum of Lorentzians, this code fits it to an actual Airy function, as described in Equation 4.3. The beginning of the program is the same as the one in the previous section, until the fit function is input as an Airy function. The fit parameters here are not peak locations, but the coefficients of a polynomial needed to make the argument of the Airy function (assumed to be a fourth order polynomial) fit the recorded data.

Good initial guesses for the coefficients of the fourth order polynomial are needed. We use the following: the location of the middle peak as a_0 , the average peak spacing for a_1 , and the difference between the first two and last two peak spacings for a_2 . All other polynomial coefficients are assumed to be 0 as initial guesses (they will be found by the fitting procedure). Once the fit is performed, the polynomial in the Airy function’s argument *is* the function which, when applied to the frequency axis, linearizes the data.

FabryPerotFittingIndium_Airy_Bootstrap.m

This is exactly the same as the above program, but it uses a “bootstrapping” fitting procedure, so that the initial guesses from each fit come from the results of the previous fit. Only the very first time the program is run must the computer construct initial guesses based on the peaks found by `sympeaksIndium`.

D.1.4 **FrequencyLinearizationIndium.m**

This program also has two variations: if the Airy function fit was used for the Fabry-Perot fitting, it is necessary to append `Airy` to the file name.

FrequencyLinearizationIndium.m

If the fit to the Fabry-Perot was performed as a sum of Lorentzians, then this code is necessary to turn the peak location information into a polynomial used to linearize the frequency axis. This program takes the measured peak locations stored in `FPoints`, and plots them versus an assumed Fabry-Perot FSR of 500 MHz. If the axis were already linear, this would form a line; deviations from linearity make it a higher order polynomial.

A polynomial fit is performed to these points, and the polynomial coefficients are saved in a vector `p`. Using the MATLAB command `polyval` applied to any x -axis vector (e.g., `x_fp_DS`) will linearize that axis.

FrequencyLinearizationIndium_Airy.m

If the Airy fitting method were used, then the frequency linearization step does not require a new polynomial fit—the polynomial is already known! Therefore, this subprogram is very simple: it applies `polyval` to the `p` computed within the Airy fitting to linearize the Fabry-Perot axis and produce a linearized plot.

D.1.5 **LorentzianFitIndium.m**

With the linearizing function found in the vector `p`, we now turn our attention to frequency *calibration* using the vapor cell hyperfine signal. The very first step involves linearization of the HFS signal, by application of `polyval` to `x_hfs_DS`. It then uses `sympeaksIndium` to search for 5 peaks (even though there are 6 peaks in the HFS signal, the central 2 overlap enough that we cannot expect this step of the program to distinguish them).

The output of `sympeaksIndium` is used to provide initial guesses to a full sum-of-Lorentzians fit. That fit is performed, most importantly leaving us with the location of all six peaks. We compute the splitting between the sixth and fifth peaks (the 6-5 splitting) and between the second and first peaks (the 2-1 splitting). Given the linearized axis, these should both be exactly equal to one another. Often, they are not quite perfectly equal but are within less than 1%. That tells us the linearization has essentially completed its job. The peak locations and heights, along with a goodness-of-fit parameter, are collected into a vector called `Z`.

We use the known modulation frequency from the IR EOM—600 MHz—to define the average splitting to be 600 MHz. We know that the EOM is driven at 600 MHz to extremely high precision, so this is the best way to impose a known frequency scale. We do so by defining a correction factor, \mathcal{C} , which we can later apply to all frequency

measurements to scale them to the correct values. (The FSR of the Fabry-Perot is close to, but not quite, 500 MHz, so \mathcal{C} is usually very close to 1.)

D.1.6 Atomic Beam Frequency Axis Finalization

To set a consistent “zero” of frequency, we now define the the constant in the linearizing polynomial such that the largest hyperfine peak (the $6P_{1/2}(F = 5)$ state) is at 0. This is done by subtracting the location of this peak from the original value of a_0 . With this newly defined vector of polynomial coefficients, \mathbf{p} , we now linearize the frequency axis of the two-tone FM signal by applying `polyval` to that dataset’s horizontal axis. The linearized axis is saved as `ttfm_freqSIG`.

Note that, because the whole program is looping over `n2` (picking up `n2 = 0` and `1`), the zero of frequency is always at the location of the hyperfine peak recorded simultaneously with the two-tone FM signal being analyzed. Therefore, any pernicious laser drift will not affect our data because we know that the atomic transition frequency can *never* change— any apparent shift in that location must come from the laser’s PZT drifting. Therefore, this is a way to measure the shift from a consistent zero point.

D.1.7 Separation of HV-on and HV-off Data

Now we separate out HV-on and HV-off datasets, depending on whether the loop was on the iteration with `n2 = 0` or `1`. In each case, we define an interpolating function which runs along the linearized frequency axis defined above. We save two interpolations: for the HV-off case, we have an axis `freqSIG0` and for the HV-on case, we have an axis `freqSIG1` over which to interpolate. For both HV-on and HV-off cases we also define the necessary parameters of the hyperfine splitting, the sideband peak separations, and the correction factor, \mathcal{C} (along with uncertainties). All of this will be included in the final collected data array.

D.1.8 OverlapEvaluation.m

This portion of the code carries out the “overlap method” described in Section 4.2.5. First, we define two variables, `Delta_min` and `Delta_max` which define how far the overlap method will shift one dataset over the other. We choose to make these `field2 - 40` and `field2 + 40`, respectively, to scan about a region 80 MHz on either side of the expected Stark shift.

The actual code of `OverlapEvaluation.m` first defines a vector of zeros which will be filled with overlap differences— the number χ^2 in Equation 4.4. Then, for each shift value between `Delta_min` and `Delta_max` the code computes the value of χ^2 for that particular amount of shift. It then collects data into an array, consisting of the `Delta` (the shift we imposed on the data) and `chisq` (the summed-squared-difference).

Because we expect the shape of χ^2 to be quadratic about the actual Stark shift, we fit this data to a parabola and use the known formula for the vertex of the parabola

to find the shift corresponding to the minimum χ^2 . That value is the Stark shift. We save this value as `min_diff` to be compiled with other computed values in the outer code.

D.1.9 Outputting Data

After all this analysis, we construct an array of data aptly named `dataArray`. It contains the hyperfine splittings, the sideband splittings used for frequency calibration, the correction factor \mathcal{C} , and `min_diff`, as well as uncertainties in all of these parameters. It then saves the data to a desired location, within the folder from which all the analyzed data originated.

D.2 Final Analysis

The final analysis usually consists of compiling histograms, or else plotting the observed Stark shifts versus \mathcal{E}^2 to determine k_S from the slope. Constructing histograms is easily done within MATLAB, whereas we usually prefer Kaleidagraph to fit lines. The future user can decide how they prefer to do any of these steps of the analysis however, as they are typically conducted outside the confines of a single MATLAB program.

Appendix E

Measuring the Stark Effect in a $j = 3/2$ State

In this Appendix, we work out the theory behind how a tensor polarizability may be measured. This is relevant to studying the indium $6P_{3/2}$ state and the thallium $7P_{3/2}$ state.

E.1 Measuring the Indium $6P_{3/2}$ Tensor Polarizability

Here, we derive the method by which we may measure the tensor polarizability of the indium $6P_{3/2}$ state. This involves measuring how the Stark shift affects different m_F levels within that state. Following [2], the perturbing Hamiltonian in this case is the sum of a hyperfine interaction and a Stark interaction operator:

$$H' = H_{\text{hf}} + H_S \quad (\text{E.1})$$

where we note that the hyperfine interaction is diagonal in the $|F, m_F\rangle$ basis. As usual, the Stark Hamiltonian is zero to first order in the applied electric field (assuming degeneracy can be neglected), so we must turn to second-order perturbation theory. We can write the matrix elements of the perturbing Hamiltonian as:

$$\langle F, m_F | H_{\text{hf}} | F, m_F \rangle = \frac{1}{2}AK + \frac{1}{4}B \frac{\frac{3}{2}K(K+1) - \frac{99}{2}J(J-1)}{36J(2J-1)} \quad (\text{E.2})$$

$$\langle F, m_F | H_S | F'', m_F \rangle = -\frac{1}{2}\alpha_0\mathcal{E}^2\delta_{F,F''} - \frac{1}{2}\alpha_2\mathcal{E}^2 \langle F, m_F | Q | F'', m_F \rangle \quad (\text{E.3})$$

In the first equation, $K = F(F+1) - J(J+1) - \frac{99}{4}$ (this equation assumes $I = 9/2$ as for indium), A is the magnetic dipole coupling constant, and B is the electric quadrupole coupling constant. These constants were measured by the Majumder lab in [31]. In the second equation, \mathcal{E} is the applied electric field (assumed to be

linearized polarized so $\Delta m_F = 0$), α_0 is the scalar polarizability, α_2 is the tensor polarizability, $\delta_{F,F''}$ is the Kronecker delta, and Q is an operator describing how the Stark interaction mixes the hyperfine states. The matrix elements of the hyperfine terms can be determined experimentally, while the matrix elements of the Stark terms can be calculated from Wigner 3- j and 6- j symbols—the formula for these matrix elements is given by Equation 41 in [32].

Still following [2], we will make a clever choice of states to investigate: since the Stark interaction will not mix states of different m_F values, the $|6, 6\rangle$ state cannot mix with any other state, so this part of the perturbation is a 1×1 matrix:

$$\langle 6, 6 | H' | F'', 6 \rangle = -\frac{1}{2}\alpha_0\mathcal{E}^2 - \frac{1}{2}\alpha_2\mathcal{E}^2 + \langle 6, 6 | H_{\text{hf}} | 6, 6 \rangle \quad (\text{E.4})$$

Similarly, the $|6, 5\rangle$ state can only mix with the $|5, 5\rangle$ state. This part of the perturbation is therefore a 2×2 matrix (elements determined from [32]):

$$\langle 6, 5 | H' | F'', 5 \rangle = -\frac{1}{2}\alpha_0\mathcal{E}^2 + \begin{pmatrix} -\frac{1}{4}\alpha_2\mathcal{E}^2 - \langle 6, 5 | H_{\text{hf}} | 6, 5 \rangle & -\frac{\sqrt{3}}{2}\alpha_2\mathcal{E}^2 \\ -\frac{\sqrt{3}}{2}\alpha_2\mathcal{E}^2 & \frac{1}{4}\alpha_2\mathcal{E}^2 - \langle 5, 5 | H_{\text{hf}} | 5, 5 \rangle \end{pmatrix} \quad (\text{E.5})$$

If we diagonalize Equation E.5 and subtract the $|6, 5\rangle$ eigenvalue from the $|6, 6\rangle$ eigenvalue found via Equation E.4, we determine α_2 in terms of the splitting induced between the two magnetic sublevels and the electric field value, \mathcal{E}^2 . That is, the measurement we wish to perform is a measurement of how the $|6, 5\rangle$ and $|5, 5\rangle$ magnetic sublevels shift by different amounts due to a nonzero tensor polarizability. We can also determine α_0 using the measured value of α_2 and Equation E.4.

Note that we had to make special choices of which hyperfine level to populate (i.e., $F = 6$ above) so as to avoid looking at levels which can mix with many others. We can pull the same trick to study the $F = 3$ level at the bottom of the “ladder” in the $6P_{3/2}$ state. That will provide a complimentary test of α_2 . Because of selection rules, this requires paying special attention to the *intermediate* state we populate within the $6S_{1/2}$ manifold: the selection rule $\Delta F = 0, \pm 1$ requires we populate the $6S_{1/2}(F = 5)$ state to reach $6P_{3/2}(F = 6)$, but that we populate the $6S_{1/2}(F = 4)$ state to reach the $6P_{3/2}(F = 3)$ state. In his thesis, Paul Hess did exactly this [31], so we will follow his lead in the Stark shift experiment.

E.2 Measuring the Thallium $7P_{3/2}$ Tensor Polarizability

A very similar calculation can be carried out for the thallium $7P_{3/2}$ state. In fact, the calculation is even simpler than above because the nuclear spin of thallium is $I = 1/2$, so there are only two F states: $F = 1$ and $F = 2$. As above, the Stark interaction cannot mix states of different m_F values, so the $|2, 2\rangle$ state cannot mix with any other state. This means that this part of the perturbation is a 1×1 matrix:

$$\langle 2, 2 | H' | F'', 2 \rangle = -\frac{1}{2}\alpha_0\mathcal{E}^2 - \frac{1}{2}\alpha_2\mathcal{E}^2 + \langle 2, 2 | H_{\text{hf}} | 2, 2 \rangle \quad (\text{E.6})$$

Similarly, the $|2, 1\rangle$ state can only mix with the $|1, 1\rangle$ state. This part of the perturbation is therefore a 2×2 matrix,

$$\langle 2, 1 | H' | F'', 1 \rangle = -\frac{1}{2}\alpha_0\mathcal{E}^2 + \begin{pmatrix} -\frac{1}{4}\alpha_2\mathcal{E}^2 - \langle 2, 1 | H_{\text{hf}} | 2, 1 \rangle & -\frac{\sqrt{3}}{2}\alpha_2\mathcal{E}^2 \\ -\frac{\sqrt{3}}{2}\alpha_2\mathcal{E}^2 & \frac{1}{4}\alpha_2\mathcal{E}^2 - \langle 1, 1 | H_{\text{hf}} | 1, 1 \rangle \end{pmatrix} \quad (\text{E.7})$$

If we diagonalize Equation E.7 and subtract the $|2, 1\rangle$ eigenvalue from the $|2, 2\rangle$ eigenvalue found via Equation E.6, we determine α_2 in terms of the splitting induced between the two magnetic sublevels and the electric field value, \mathcal{E}^2 . That is, the measurement we wish to perform is a measurement of how the $|2, 1\rangle$ and $|1, 1\rangle$ magnetic sublevels shift by different amounts due to a nonzero tensor polarizability. We can also determine α_0 using the measured value of α_2 and Equation E.6. In this case, the special choices about which states to populate are less complicated, because of the small nuclear spin.

Bibliography

- [1] P. A. Vetter, D. M. Meekhof, P. K. Majumder, S. K. Lamoreaux, and E. N. Fortson, *Physical Review Letters* **74**, 2658 (1995), ISSN 1079-7114.
- [2] A. Kortyna, C. Tinsman, J. Grab, M. S. Safronova, and U. I. Safronova, *Phys. Rev. A* **83** (2011), ISSN 1094-1622.
- [3] J. Mitroy, M. S. Safronova, and C. W. Clark, *J. Phys. B* **43** (2010).
- [4] T. D. Wolfenden, P. E. G. Baird, and P. G. H. Sandars, *Europhysics Letters* **15**, 731 (1991), ISSN 1286-4854.
- [5] B. K. Sahoo, R. Pandey, and B. P. Das, *Phys. Rev. A* **84** (2011), ISSN 1094-1622.
- [6] M. S. Safronova, U. I. Safronova, and S. G. Porsev, *Phys. Rev. A* **87** (2013), ISSN 1094-1622.
- [7] M. S. Safronova and P. K. Majumder, *Phys. Rev. A* **87** (2013).
- [8] P. K. Majumder and L. L. Tsai, *Phys. Rev. A* **60** (1999).
- [9] D. S. Richardson, R. N. Lyman, and P. K. Majumder, *Phys. Rev. A* **62** (2000).
- [10] S. C. Doret, P. D. Friedberg, A. J. Speck, D. S. Richardson, and P. K. Majumder, *Phys. Rev. A* **66** (2002).
- [11] M. Gunawardena, H. Cao, P. W. Hess, and P. K. Majumder, *Phys. Rev. A* **80** (2009), ISSN 1094-1622.
- [12] G. Ranjit, N. A. Schine, A. T. Lorenzo, A. E. Schneider, and P. K. Majumder, *Phys. Rev. A* **87** (2013), ISSN 1094-1622.
- [13] G. Vukasin, Bachelor's thesis, Williams College (2014).
- [14] B. K. Sahoo and B. P. Das, *Phys. Rev. A* **84** (2011).
- [15] N. Schine, Bachelor's thesis, Williams College (2013).
- [16] A. Lorenzo, Bachelor's thesis, Williams College (2011).
- [17] N. Bricault, Bachelor's thesis, Williams College (2014).

- [18] C. D. Holmes, Bachelor's thesis, Williams College (2003).
- [19] G. Janik, C. B. Carlisle, and T. F. Gallagher, *J. Opt. Soc. Am. B* **3**, 1070 (1986).
- [20] F. W. Strauch, Personal communication (2015).
- [21] B. W. Shore, *The Theory of Coherent Atomic Excitation*, vol. 2 (Wiley-VCH, 1990).
- [22] C. Cohen-Tannoudji and S. Reynaud, *J. Phys. B* **10** (1977).
- [23] B. W. Shore, *Manipulating quantum structures using laser pulses* (Cambridge University Press, 2011).
- [24] P. K. Majumder, PhD thesis, Harvard University (1989).
- [25] M. Gunawardena, P. W. Hess, J. Strait, and P. K. Majumder, *Review of Scientific Instruments* **79**, 103110 (2008), ISSN 0034-6748.
- [26] S. George, G. Guppy, and J. Verges, *J. Opt. Soc. Am. B* **7**, 249 (1990).
- [27] S. H. Autler and C. H. Townes, *Phys. Rev.* **100** (1955).
- [28] W. Demtroder, *Laser Spectroscopy: Basic Concepts and Instrumentation*, vol. 2 (Springer, 1998).
- [29] N. A. Schine, G. Ranjit, and P. K. Majumder, *Optical Society of America* (2013).
- [30] M. L. Boas, *Mathematical Methods in the Physical Sciences* (John Wiley & Sons, Inc., 2006).
- [31] P. W. Hess, Bachelor's thesis, Williams College (2008).
- [32] R. W. Schmieder, *Am. J. Phys.* **40**, 297 (1972).